DOE/CE/40936--T5-Vol.4

Black Liquor Combustion Validated Recovery Boiler Modeling Final Year Report

Volume 4
(Appendix IV)

by

T.M. Grace, W.J. Frederick, M. Salcudean, and R.A. Wessel

August 1998

A Summary Report
of the Project

Work Performed Under Contract DE-FG07-90CE40936

Prepared for

The U.S. Department of Energy
Office of Industrial Technologies
Washington, D.C.

Prepared by

The Institute of Paper Science and Technology
Atlanta, GA

Oregon State University
Corvallis, OR

University of British Columbia
Vancouver, BC, Canada

Babcock & Wilcox Company
Alliance, OH

DISCLAIMER

DISCLAIMER

Portions of this document may be illegible in electronic image products. Images are produced from the best available original document.

Table of Contents
Volume 4

RADIATIVE HEAT TRANSFER PROPERTIES FOR BLACK LIQUOR COMBUSTION

Final Project Report

April 1, 1995 - August 30, 1996

By:

BABCOCK & WILCOX COMPANY

Richard A. Wessel
Ralph T. Bailey

Date: August 27, 1996

Subcontract No. 1
Between
THE INSTITUTE OF PAPER SCIENCE AND TECHNOLOGY
AND
BABCOCK AND WILCOX

DOE DE-FG02-90CE40936
IPST Project No. 3605-2
B&W CRD No. 1328
B&W RDD No. 43383

NOTICE

This report was prepared by Babcock & Wilcox as an account of work sponsored by the United States Government. Neither the United States Government, nor the US Department of Energy, nor the Institute of Paper Science and Technology, nor Babcock & Wilcox, nor their subcontractors, nor any of their employees, makes any warranty, express or implied, or assumes any legal liability or responsibility for the accuracy, completeness, or usefulness of any information, apparatus, product, or process disclosed, or represents that its use would not infringe privately-owned rights.

TABLE OF CONTENTS

LIST OF FIGURES

LIST OF TABLES

EXECUTIVE SUMMARY

The spectral emittance of kraft black liquor and condensed phase products of combustion was measured using two experimental techniques:

- Spectral reflectances of black liquor, dried solids, char, and salt cake were measured at room temperature (25°C). Samples were illuminated by monochromatic light, and the reflected energy from the samples was measured. Spectral reflectance was determined by comparing the reflected energy from the sample to that reflected from a standard surface of known reflectance. Spectral absorbance (and emittance) was determined from a reciprocal relationship.

- Spectral emittances of char, smelt and salt cake were measured at high temperatures (450-850°C) and under controlled conditions to suppress chemical decomposition. Spectral emittance was determined by comparing the emitted energy from the sample to that emitted by a blackbody at the same temperature.

High temperature emittance measurements for char were unsuccessful due to difficulties heating the porous material, however low temperature measurements for char were successful.

Total emittance was calculated as a function of blackbody temperature for each sample. Black liquor, dried solids, and char have relatively high emittances (0.8 to 1.0) that decrease with temperature. Molten smelt also has a relatively high emittance (0.8 to 0.95), that is independent of the amount of sulfide oxidation, and appears to be transparent to radiation at short wavelengths. In contrast, salt cake dust and sintered fume deposits have a very low emittance (0.2 to 0.7), that decreases significantly with temperature. The highly porous nature of this material probably contributes to it's low emittance at low wavelengths due to internal scattering of transmitted radiation. Consequently, radiation properties have a large effect on furnace heat flux distribution because they are largely dependent on the physical characteristics, melting point and temperature of recovery boiler deposits.

Engineering correlations were successfully developed for radiation properties of black liquor, dried solids, char, molten smelt and salt cake for temperatures 100 to 1800°C. Correlations for total emissivity and absorptivity should be used to calculate surface radiation heat transfer. Equations for particle emission, absorption and scattering coefficients should be used to calculate heat transfer for black liquor drop combustion. Particle properties are valid for the large particle limit ($\pi d/\lambda >> 1$) typical of black liquor spray combustion in recovery boilers ($d > 100\ \mu m$, $\lambda < 10\ \mu m$).

Emissivity correlations were implemented into a model for heat transfer and combustion of single black liquor drops. Sensitivity of the model was evaluated and radiation properties were found to have a large effect on predicted burning times for conditions used in captive drop experiments and for combustion of 2 mm drops at simulated recovery boiler conditions. Therefore accurate radiation properties are needed to understand and interpret experimental results for black liquor combustion, and to predict heat transfer and combustion of black liquor spray in numerical models of a recovery furnace. Modeling results should be used as a benchmark for others who wish to implement the radiative properties.

Radiative properties characterized in this work provide some of the basic tools needed to calculate heat transfer in recovery boilers. However, additional work is needed to characterize radiative properties of gas entrained aerosol particles and to continue characterization of thermal and radiative properties of inorganic deposits. Radiative properties of inorganic aerosol are needed to understand the effect of gas-entrained, submicron fume particles on furnace heat transfer. More detailed measurements are needed to characterize radiation properties of partially transparent materials (smelt and fume deposits) over a range of conditions (temperature, chemical composition, physical characteristics, layer thickness and substrate materials). Understanding of thermal properties of deposits will improve strategies for cleaning convective surfaces and may increase runtime or throughput between boiler outages.

ACKNOWLEDGEMENTS

Appreciation is acknowledged for the guidance and support provided by Dr. Thomas M. Grace, Principal Investigator and Project Manager, Institute of Paper Science and Technology. The authors would like to acknowledge those who provided technical support to this project: Robert A. McIlroy, Christopher L. Verrill, and Larry A. Hiner of Babcock & Wilcox Company.

1.0 INTRODUCTION

1.1 BACKGROUND

Radiation properties of black liquor, char, smelt and salt cake are needed to calculate heat transfer in a kraft recovery boiler. Heat transfer in the lower furnace is dependent upon the emissivity and absorptivity of burning black liquor drops, char bed and deposits on the furnace walls. These properties can be determined from measurements of spectral emittance (or reflectance) over the infrared spectrum, at wavelengths from 0.7 to 12 μm. Radiation properties for combustion gases (H_2O, CO_2, CO and SO_2) and soot particles are also needed, but are readily available in the literature (Siegel and Howell, 1981; Edwards and Balakrishnan, 1973).

Properties of gas-entrained carryover and aerosol (fume) particles are needed for absorption and scattering of radiation in the upper furnace. Radiation properties of small particles, less than about 100 μm, are determined from measurements of the complex index of refraction and calculations based on Mie theory (Bohren and Huffman, 1983). Properties of particles, greater than 100 μm, can be determined from measurements of spectral emittance. Prior to this work, these properties were not available in the open literature.

Models have generally relied on estimates of black liquor radiation properties based on engineering assumptions or properties of coal, char and ash (Wessel et al, 1993). Radiation properties are also used to analyze and interpret black liquor combustion data to develop chemical kinetic relationships for combustion submodels (Frederick, 1990; Frederick and Hupa, 1993). Predicted drop heating rates and temperature, during drying and devolatilization stages of combustion, have a large effect on drop swelling and burning characteristics (Wessel and Verrill, 1995). Submodels for black liquor combustion and radiative heat transfer are used in global models for recovery boilers to predict boiler performance (Wessel et al, 1995; Nowak et al, 1995). Radiative properties are critical for predicting furnace heat absorption and the temperature of combustion gases exiting the furnace cavity. Local heat flux and temperature of furnace walls is sensitive to the emissivity of wall deposits.

The reader is referred to a monograph on the properties and thermal effects of ash deposits in coal-fired furnaces (Wall, et al., 1993) for more background on furnace radiation properties.

1.2 OBJECTIVE

The objective of this project is to characterize radiation properties for black liquor combustion based on spectral emittance measurements of black liquor and intermediate condensed phase products of combustion. This goal was accomplished by:

- Measuring spectral emittance (or reflectance) of black liquor, dry solids, char, molten smelt and salt cake. The results of these measurements are described in Section 2.0.

- Developing engineering correlations of total emissivity and absorptivity for surface radiation; and emission, absorption and scattering efficiencies for black liquor drop combustion. These correlations and the governing equations for radiative heat transfer are described in Section 3.0.

- Implementing radiative properties into models for black liquor combustion and evaluating the effect of the properties on model predictions. Modeling results for black liquor drop combustion are described in Section 4.0.

1.3 NOMENCLATURE

Radiative properties and associated nomenclature are well defined in the literature (Siegel and Howell, 1981; Wall, et al., 1993). However, the terms *emissivity* and *emittance*, *absorptivity* and *absorbance*, and *reflectivity* and *reflectance* are commonly interchanged. In this work, the following nomenclature will be used:

- *emittance, absorbance* and *reflectance* are used with the experimental determination of surface properties. The *-ance* ending is usually reserved for extensive properties, and in

this case denotes that properties are dependent upon non-ideal conditions such as surface roughness and contamination, or dependent upon layer thickness when the material is partially transparent.

- *emissivity, absorptivity* and *reflectivity* are used with the analytical or empirical determination of surface properties. The *-ivity* ending is usually reserved for intensive properties, which is more consistent with the use of these terms, and denotes that the effects of non-ideal surface conditions have been neglected.

2.0 RADIATION PROPERTY MEASUREMENTS

2.1 SAMPLE PREPARATION

Samples of black liquor, dry solids, char, industrial smelt, two synthetic smelts and industrial salt cake were prepared for emittance measurements. A large sample of as-fired black liquor was obtained from a kraft mill producing bleached softwood pulp. The black liquor sample was analyzed for gross heating value, solids content and elemental composition (Table 1). A sample of dry solids was prepared from the liquor sample by spreading the liquor in a shallow pan and drying for 16 hours (two 8 hour days) at 105°C under an air atmosphere. A sample of char was prepared by heating the liquor to 500°C in a muffle furnace. The furnace temperature was raised to the final temperature in several steps over a period of 3 hours.

Individual samples of solidified smelt were collected from each of the five smelt spouts in ingot molds. The solidified ingots were broken and material from the unoxidized center was analyzed for total sodium, potassium, sulfur, and chlorine content, and sulfidity (Table 2). Additional center material from the sample 53580 ingot was used as the industrial smelt sample. The synthetic mixtures were prepared from reagent grade compounds to represent a fully-reduced and fully-oxidized smelt. The ratios of sulfur to total alkali and potassium to sodium in the synthetic smelts were based on the average values from the industrial smelt analysis. The readily available reagent grade of Na_2S contained 9 waters of hydration. The material was dehydrated by heating to 105°C in an oven flushed with nitrogen. The dry product was then ground to a powder in a glove box flushed with nitrogen. The dry powders were then weighed and mixed together (Table 3). There was no attempt to premelt the mixtures since the would be melted during the emittance measurement.

Salt cake samples were collected in the first bank of a long flow economizer at another mill producing bleached kraft pulp. Bulk dust samples were collected from the baffle plate. Fume deposits were collected by inserting a steel plate in the gas stream for several hours, then carefully removing. Samples were not analyzed for chemical content.

Table 1. Analysis of As-Fired Black Liquor

B&W sample No.		F-5871	
Basis (Oven dry)		As Received	Dry
Moisture	(% wt)	32.65	0.00
Solids	(% wt)	67.35	100.00
Gross Heating Value	(kJ/kg)	8,862	13,157
Elemental Analysis, % by weight			
Moisture		32.65	0.00
Carbon		21.40	31.77
Hydrogen		2.42	3.59
Nitrogen		0.05	0.07
Sulfur		4.25	6.31
Sodium		14.83	22.02
Potassium		1.01	1.50
Chlorine		0.55	0.82
Inerts		0.00	0.00
Oxygen (by diff.)		22.84	33.92
Total		100.00	100.00

Table 2. Analysis of Smelt Samples

Composition as reported, % by weight							
Sample No.		53580	53581	53582	53583	53584	Average
Total S	(as SO_3)	29.9	29.7	30.4	30.9	30.1	30.2
Total Na	(as Na_2O)	58.0	56.1	61.0	59.4	58.1	58.5
Total K	(as K_2O)	3.2	3.1	3.2	3.2	3.0	3.1
Total Cl	(as Cl)	1.4	1.4	1.3	1.5	1.4	1.4
Calculated composition, % by weight							
Na_2CO_3		68.3	68.6	68.4	67.7	67.9	68.2
NaOH		0.0	0.0	0.2	0.8	0.0	0.2
NaCl		2.2	2.2	2.2	2.5	2.3	2.3
Na_2S		25.9	26.2	27.7	27.8	25.0	26.5
$Na_2S_2O_3$		1.7	1.8	1.5	1.4	1.7	1.6
Na_2SO_3		0.0	0.1	0.0	0.0	0.0	0.0
Na_2SO_4		2.4	3.3	2.1	2.2	5.3	3.1
NaHS		0.5	0.0	0.0	0.0	0.4	0.2
Total		101.0	102.2	102.1	102.4	102.6	102.1
Molar Ratios, %							
$S/(Na_2O+K_2O)$		38.550	39.595	37.343	38.871	38.779	38.610
K_2O/Na_2O		3.633	3.639	3.400	3.588	3.412	3.533

Table 3. Composition of Synthetic Smelt

Composition, % by weight	Oxidized	Reduced
Na_2CO_3	50.79	63.83
Na_2S	0.00	31.28
Na_2SO_4	45.31	0.00
K_2CO_3	3.89	4.89
Total	100.00	100.00
Molar Ratios, %		
$S/(Na_2O+K_2O)$	38.610	38.610
K_2O/Na_2O	3.533	3.533

2.2 EXPERIMENTAL APPARATUS

The spectral emittance of the different forms of kraft black liquor and condensed phase products of combustion was measured using two experimental techniques.

- The spectral reflectance of black liquor, dried solids, char and salt cake samples was measured at room temperature, 25°C, at which the amount of emitted energy is too small to be measured. Samples were illuminated by monochromatic light, and the reflected energy from the samples was measured. Spectral reflectance was determined by comparing the reflected energy from the sample to that reflected from a standard surface of known reflectance. Spectral absorbance (and emittance) was determined from a reciprical relationship.

- Spectral emittances of char, smelt and salt cake were measured at high temperatures, 450-850°C, at which the amount of emitted spectral energy could be measured directly. Spectral emittance was determined by comparing the emitted energy from the sample to that emitted by a blackbody at the same temperature.

High temperature emittance measurements for char were unsuccessful due to difficulties heating the porous material, however low temperature measurements were successful.

Spectral Reflectance Measurement Facility

The Spectral Reflectance Facility is shown schematically in Figure 1 and consists of a blackbody radiation source, grating monochrometer, infrared integrating sphere and associated photo-detectors. The integrating sphere is 8 inches in diameter with the interior surface coated with gold to provide high reflectance over the measurement range of about 0.7 to 14 μm. Three penetrations are located around the equator of the sphere. Light enters one port and is focused onto the sample port, located on the opposite side of the sphere. Located at 90 degrees to these ports, is the third port in which a photo-detector is mounted. Light reflected from the sample at all angles is contained and reflected inside the sphere. The magnitude of the light energy,

measured by the photo-detector, is a measure of the energy reflected by the sample.

Reflectance is determined by measuring the photo-detector signal from a gold-coated sample (reflectance, $\rho = 0.96$), from an open hole ($\rho = 0$), and from the sample of unknown reflectance. The spectral reflectances of the samples are between those of the gold-coated sample and the open hole, and the sample reflectance is determined by linear interpolation.

For measuring reflectance as a function of wavelength the integrating sphere was placed at the output of the monochrometer which together with the blackbody radiation source provided a stable and repeatable source of wavelength separated light. This measurement provides the total hemispherical reflectance. For an opaque material, the absorptance (emittance) is simply the difference between unity and reflectance.

An uncertainty analysis performed for the facility shows the uncertainty in spectral emittance at two standard deviations to be around 6 to 7 percent for wavelengths from 1 to 5 μm. For wavelengths greater than 6 μm, the uncertainty is about double. The increase above 6 μm is due to the increased electronic noise of the detector that is used in this wavelength range, and a greater sensitivity to detector temperature. This uncertainty analysis is based on measurements made with the facility in the emittance mode. However, the levels of uncertainty should be about the same, for room temperature reflectance measurements. The exception is increased uncertainty for data at wavelengths beyond 10 or 11 μm where the reflected energy is typically low.

Spectral Emittance Measurement Facility

Spectral and total emittance measurements were performed at the Spectral Emittance Measurement Facility shown schematically in Figure 2. The facility consists of a high-temperature furnace, optics, a grating monochromator, a series of photo detectors, and a personal computer-based data acquisition system. A detailed description of the facility and measurement techniques is provided in Appendix A.

To determine the emittances, it is necessary to measure both the surface temperature and the spectral radiation from the heated samples. The furnace is designed to radiantly heat 2-inch square samples to temperatures in excess of 1100°C. For this test, a platinum crucible was mounted in a hole in a square plate, and the crucible was radiantly heated from the bottom. The smelt material was then placed in the crucible and heated to melting.

A gold-plated mirror and a zinc selenide lens collect and focus the emitted radiant energy into the monochromator. The monochromator and gratings then disperse the radiant energy by wavelength and transmit it to the photo detectors. The photo-detector voltage signal is proportional to the incident energy, and is measured using a computer controlled A/D (analog-to-digital) converter. Measurements are also made using the blackbody calibration source so the emissive power of the sample at a given wavelength can be normalized to that of a theoretical blackbody at the same temperature. The resulting data are then analyzed according to the procedure outlined in Appendix A.

The level of uncertainty in the spectral emittance measurements is discussed here to qualify the data. A past uncertainty analysis that was performed for the facility identified the uncertainty in spectral emittance at two standard deviations to be around 6 to 7 percent for wavelengths from 1 to 5 μm. For wavelengths greater than 6 μm, the uncertainty was about double. The increase above 6 μm was due to the increased electronic noise of the detector that is used in this wavelength range, and a greater sensitivity to detector temperature. This uncertainty analysis was performed based on using thermocouples for determining the surface temperatures.

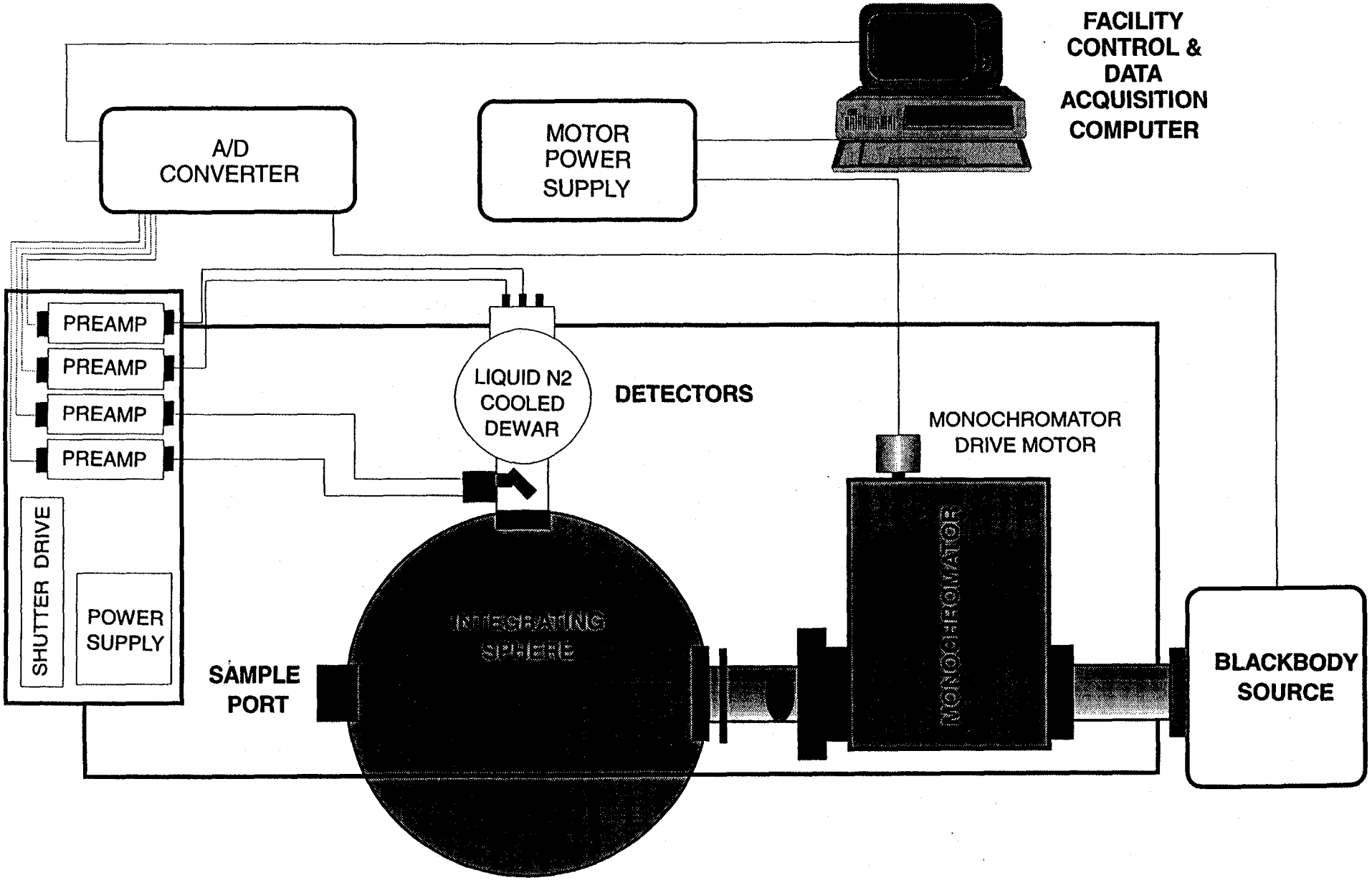

Figure 1. Spectral Reflectance Measurement Facility

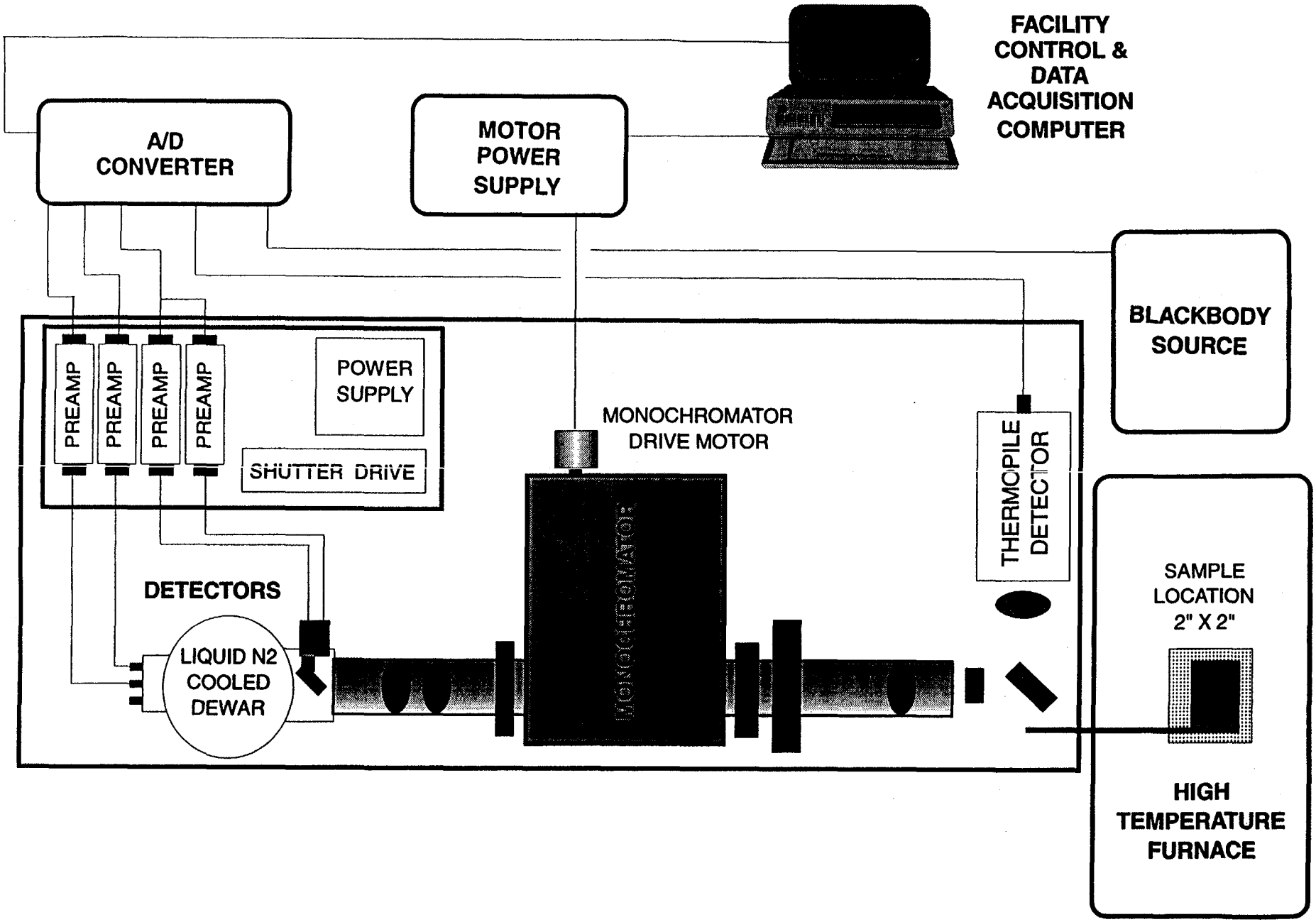

Figure 2. Spectral Emittance Measurement Facility

2.3 MEASUREMENT PROCEDURES

Spectral Reflectance Measurements

The hemispherical spectral reflectance (ρ_λ) of the black liquor, dried solids, char and salt cake was measured at room temperature, and spectral absorbance was determined from the relationship $\alpha_\lambda = 1 - \rho_\lambda$, assuming the material is opaque. Samples, at room conditions (~25°C in air), were illuminated with wavelength separated light and the magnitude of the reflected light energy was measured. This signal was then compared to that measured using a gold coated target ($\rho \sim 0.96$) and an open hole ($\rho \sim 0.0$). The sample port diameter was about 1 inch in diameter, and samples were prepared that completely covered the sample port of the integrating sphere. Measurements of reflected light energy for the open hole, gold target and the test samples were conducted sequentially. The temperature controlled blackbody source provided a very stable source of radiant energy over the duration of the test.

Black liquor, dried solids and char samples were maintained in sealed containers in an inert atmosphere until testing. The samples were prepared so that they could be easily inserted and removed from the sample holder on the integrating sphere. The liquid black liquor was "painted" onto a 1/16 inch (1.6 mm) deep recess cut into a stainless steel plate, approximately 1-1/8 inches (28.6 mm) in diameter. The high viscosity of the black liquor prevented the sample from sagging or dripping over the duration of the test. The char and dried solids samples were pressed into pellets about 1-3/8 inches (34.9 mm) in diameter and 1/16 inch (1.6 mm) thick and the unmounted pellets were inserted into the sample holder. Samples of salt cake (fume deposits), which had not fallen off the 2 by 2 inch (50.8 by 50.8 mm) collection plates, were used as the sample target.

Spectral Emittance Measurements

Spectral emittance measurements were made for synthetic smelt and industrial smelt at temperatures of about 850°C (see Table 4). The high-temperature tests were conducted under a nitrogen purge containing 10% CO to suppress Na_2CO_3 decomposition. A platinum crucible was

installed in the furnace and radiantly heated to a temperature of about 750°C. The CO/N_2 purge was started and about 5 grams of solid smelt was added to the crucible. The temperature of the crucible was then increased to melt the smelt sample and a Type S platinum/platinum-rhodium thermocouple was positioned just below the surface of the molten smelt. The 5 gram sample provided a molten smelt thickness of 3 to 5 mm in the crucible. The radiated energy spectra from the sample was measured to determine spectral emittance.

High temperature emittance measurements of the char sample were also attempted. For this material, ground char was pressed into a wafer of about 30 mm diameter and 3 mm thickness. A Pt/Pt-Rh thermocouple was placed in a small groove in the surface of the wafer and lightly covered with powdered char. The wafer was placed on a thin stainless steel plate that was radiantly heated from the backside. As with the smelt samples, the char was contained in a CO/N_2 environment to prevent oxidation. Using this procedure, the char sample was heated to about 650°C. However, at this elevated temperature, the char wafer cupped, and the thermocouple junction detached from the surface of the char so that the surface temperature was under estimated and reliable data could not be obtained.

Table 4. Radiation Property Measurement Conditions

Sample Description	Number of Tests	Measurement Technique	Sample Temperature	Sample Environment
Black Liquor (67% Solids)	2	Reflectance	25 °C	Air
Dried Black Liquor Solids	2	Reflectance	25 °C	Air
Black Liquor Char	1	Reflectance	25 °C	Air
Industrial Smelt	3	Emittance	813 - 848 °C	10% CO in N_2
Synthetic Smelt (Oxidized)	2	Emittance	870 - 931 °C	10% CO in N_2
Synthetic Smelt (Reduced)	1	Emittance	872 °C	10% CO in N_2
Packed Economizer Dust	2	Emittance	466-468 °C	Air
Fume Deposit	1	Reflectance	25 °C	Air

2.4 SPECTRAL PROPERTY RESULTS

Spectral absorbance and emittance data for black liquor combustion products are given in Appendix B; smoothed curves of these data are shown in Figures 3, 4 and 5. The radiative properties are reported here as emittance, even though the measurements may have been obtained by reflectance or emittance technique. The spectral properties of emittance ε_λ, absorbance α_λ and reflectance ρ_λ are related by $\varepsilon_\lambda = \alpha_\lambda = 1 - \rho_\lambda$, assuming the material is opaque.

High emittance was measured at nearly all wavelengths for black liquor, dried black liquor solids, and char (Figure 3). The scatter in the individual data points about the smoothed curve is about 10%. This scatter is due to the weak signal associated with these measurements along with the detector noise. The data for the black liquor and dried solids are nearly the same for wavelengths greater than 1.5 μm. The decrease in emittance indicated at wavelengths greater than 7 μm may also be due to the weak signal and relatively large measurement uncertainty at these wavelengths. The change in emittance between dried solids samples 1 and 2 may be attributed to oxidation of sample 2 after being exposed to air for an extended period.

The spectral emittance of the industrial smelt is shown in Figure 4 for three separate measurements of the same material, denoted as A, C and E. The emittance of the industrial smelt is near unity over the entire wavelength range measured in these tests. The three sets of data show similar inflections in the spectral emittance, in particular at a wavelength of about 4.5 μm.

At the shortest wavelengths, the measured emittance consistently exceeded a value of 1. This was likely caused by an underestimate of the surface temperature of the smelt, as radiant energy in the visible and near-infrared is very sensitive to temperature. For example, at a wavelength of 0.8 μm and a temperature of 850°C, a 5°C change in temperature causes a 10% change in radiant energy. For these samples, then, the spectral emittance at wavelengths below 1 to 2 μm is near 1. Visually, these molten samples appeared opaque, and the molten smelt surface contained several "black lines" that were likely carbon particles that congregated at the boundaries of convection bubbles in the molten smelt.

Figure 4 also shows the spectral emittance for a synthetic oxidized smelt, denoted as samples A and B. The two sets of data in these figures are quite repeatable, including the small inflections in spectral emittance at wavelengths above 4 μm. Although spectral data is provided down to a wavelength of about 1 μm, the data at the lowest wavelengths is suspect. This is because the molten sample was noticeably transparent at visible wavelengths. This implies that the source of the radiant energy measured at these short wavelength was the bottom of the platinum crucible rather than the molten surface of the smelt. Although the emittance of the platinum is probably quite low, the temperature of the platinum crucible can be significantly greater (i.e. 20 to 30°C) than the smelt surface. With the procedure used in this test, it is not possible to isolate radiation from the platinum from that of the smelt. For wavelengths of 3 μm and greater, the data for synthetic oxidized smelt is similar to industrial smelt.

Figure 4 shows the spectral emittance of the synthetic reduced smelt. As with the other smelt samples, the spectral emittance of this sample at wavelengths above 3 μm is near unity and shows similar spectral inflections with wavelength. Below 3 μm, the spectral emittance averages about 0.7. As with the synthetic oxidized smelt, this sample was partially transparent at visible wavelengths, but somewhat less transparent than the oxidized sample. The emittance data at short wavelengths is probably subject to similar types of errors as the oxidized smelt.

The spectral emittance of salt cake (economizer dust samples and fume deposits) are shown in Figure 5. Emittance is quite low compared to that of smelt. Economizer dust samples may be partly transparent at short wavelengths, and the indicated increase in emittance below 3 μm may be caused by radiation from the bottom of the heated sample holder. Also, these samples were tested at low temperature (~470°C) to prevent the sample from melting. At these temperatures, radiant energy at short wavelengths is extremely sensitive to temperature. Deposits are not typically heated from below and would not normally exhibit this behavior. Reflectance measurements indicate that most radiation is reflected at short wavelengths, which is consistent with the "snow" white color of the samples in the visible spectrum. Reflectance measurements are expected to be more reliable because the cold substrate is more representative of the conditions on the walls of a recovery boiler and the physical characteristics of the sample are the same at low temperatures.

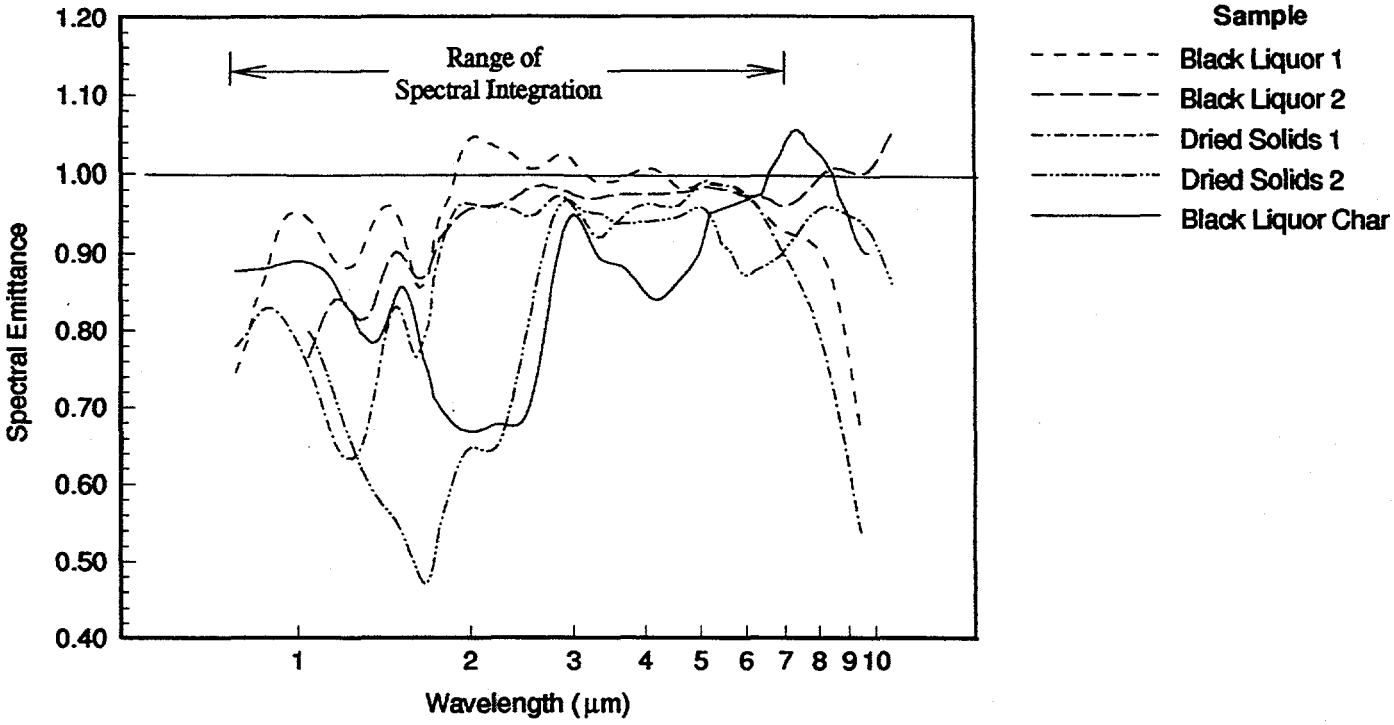

Figure 3. Spectral Emittance of Black Liquor, Dried Solids, and Char

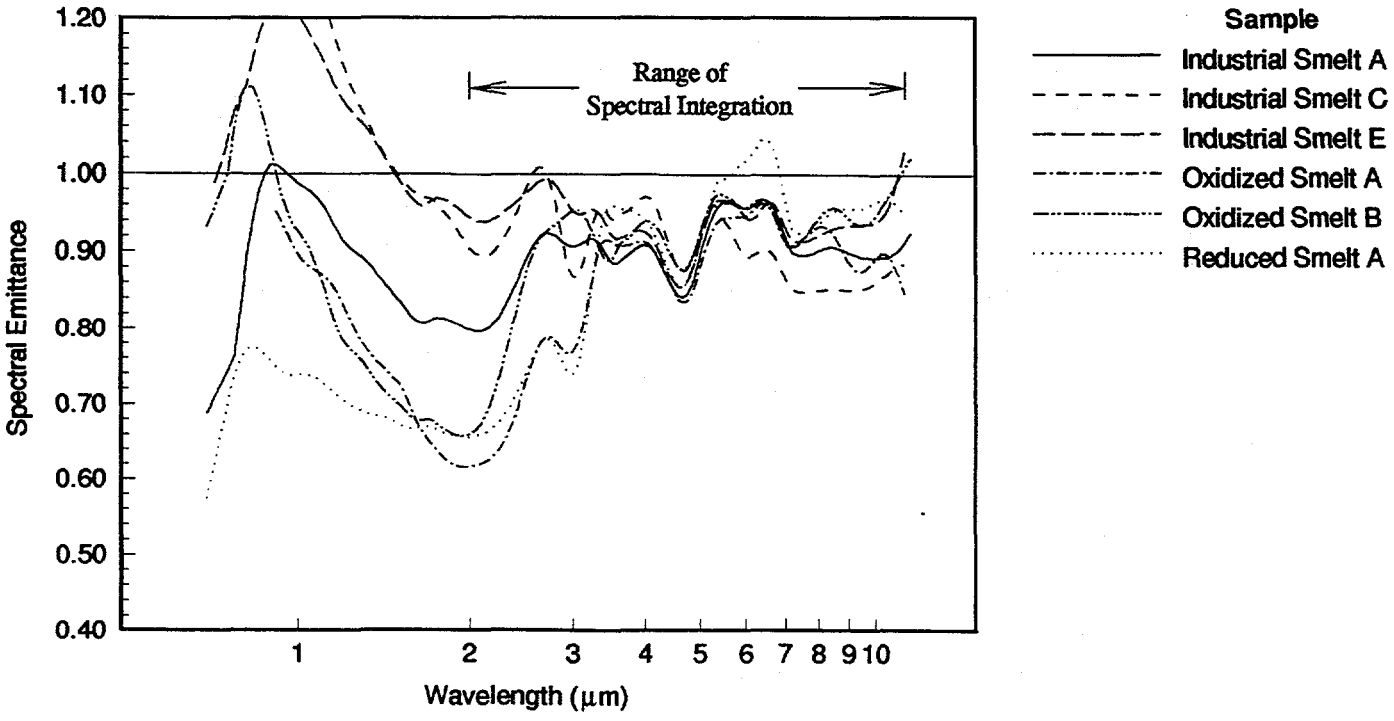

Figure 4. Spectral Emittance of Molten Smelt

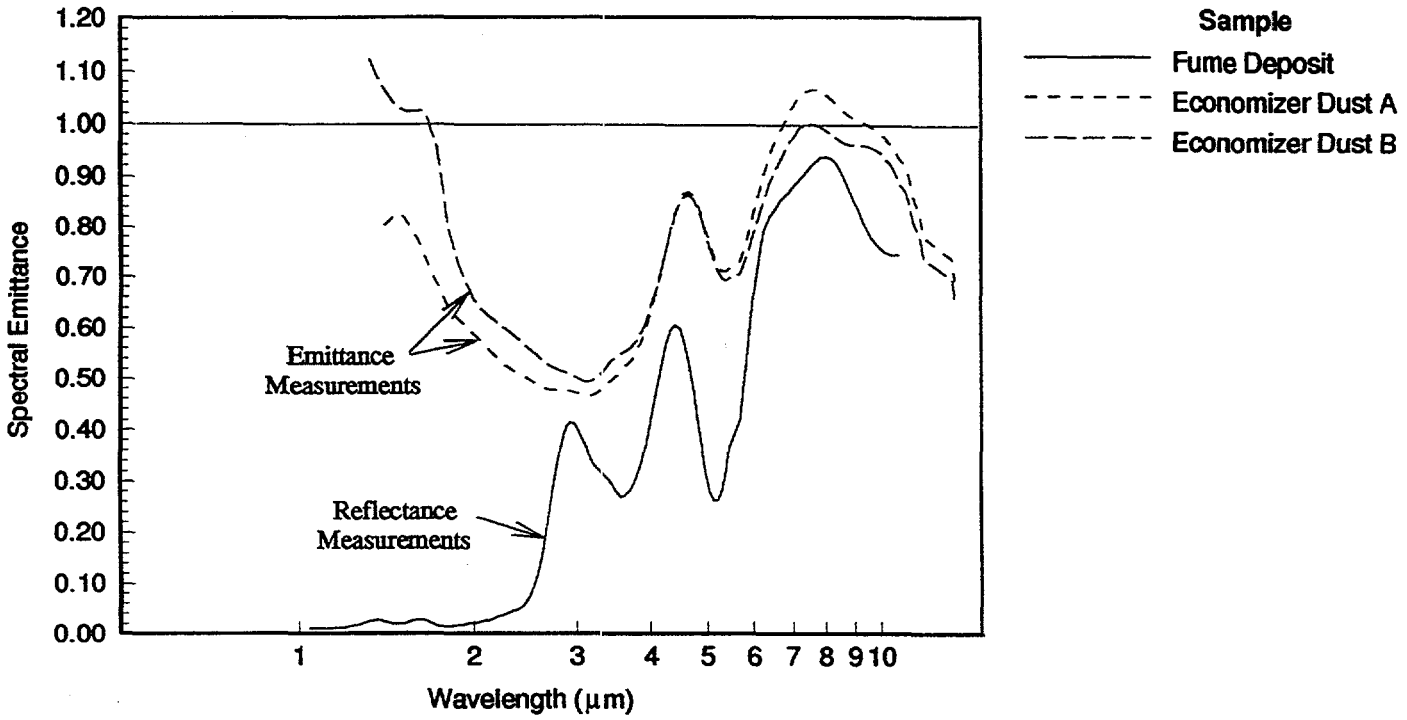

Figure 5. Spectral Emittance of Salt Cake

2.5 TOTAL PROPERTY RESULTS

Radiation properties are designated as total if they refer to the entire wavelength spectrum. Spectral emittance data were numerically integrated over the blackbody spectrum to determine the total emittance as a function of temperature:

$$\varepsilon(T_s) = \frac{\int_0^\infty \varepsilon_\lambda(T_s)\, E_{b\lambda}(T_s)\, d\lambda}{\int_0^\infty E_{b\lambda}(T_s)\, d\lambda} \cong \frac{\int_{\lambda_1}^{\lambda_2} \varepsilon_\lambda(T_s)\, E_{b\lambda}(T_s)\, d\lambda}{\int_{\lambda_1}^{\lambda_2} E_{b\lambda}(T_s)\, d\lambda} \qquad (1)$$

In these equations, λ is wavelength (μm), $\varepsilon_\lambda(T_s)$ is spectral emittance, T_s is the surface temperature (°K), and $E_{b\lambda}(T_s)$ is the blackbody emissive power (W/m^2-μm). The blackbody spectrum is shown in Figure 6 as a function of wavelength for different temperatures. Spectral measurements from 0.7 to 12 μm span most of the infrared spectrum for temperatures 200 to 1800°C (473 to 2073°K). The integration is performed over a finite interval of wavelength, by the approximation on the right side of Equation (1). For reflectance measurements, the range of integration was approximately 0.7 to 8.0 μm; data at wavelengths greater than 8.0 μm were excluded due to uncertainties in measurement accuracy (see Figure 3). For emittance measurements, the range of integration was approximately 2.0 to 10 μm; data at wavelengths less than 2.0 μm were excluded due to uncertainties in measurement accuracy (see Figure 4). Spectral emittance data were smoothed and were physically bounded ($0 \le \varepsilon_\lambda \le 1$) prior to the integration.

Total absorbance can also be calculated as a function of temperature:

$$\alpha(T_s, T_i) = \frac{\int_0^\infty \varepsilon_\lambda(T_s)\, E_{b\lambda}(T_i)\, d\lambda}{\int_0^\infty E_{b\lambda}(T_i)\, d\lambda} \cong \frac{\int_{\lambda_1}^{\lambda_2} \varepsilon_\lambda(T_s)\, E_{b\lambda}(T_i)\, d\lambda}{\int_{\lambda_1}^{\lambda_2} E_{b\lambda}(T_i)\, d\lambda} \qquad (2)$$

where T_i is the temperature of incident radiation (°K). Total absorbance depends on surface temperature due to the effects of temperature on the structure of the deposit (e.g. melting,

sintering) and possibly on variations in optical properties. If these surface temperature effects are neglected (assuming ε_λ is independent of T_s), then total emittance and absorbance are an equivalent function of temperature, $\varepsilon(T) = \alpha(T)$. Therefore, although the results and predictions which follow are presented as plots of $\varepsilon(T_s)$, they may also be interpreted as plots of $\alpha(T_i)$ assuming the physical state of the deposit is unchanged. Although $\varepsilon_\lambda = \alpha_\lambda$ is always true, generally $\varepsilon(T_s) \neq \alpha(T_i)$ unless $T_s = T_i$.

Total emittance results for samples of black liquor, dried solids, char, smelt and salt cake are shown in Figures 7, 8 and 9. Multiple curves for samples of the same material are an indication of measurement repeatability. Variations in total emittance are attributed to changes in surface composition, surface roughness, porosity and measurement uncertainties. Black liquor, dried solids, and char have relatively high emittances (0.8 to 1.0) that decrease with temperature (Figure 7). Molten smelt also has a relatively high emittance (0.8 to 0.95) at all temperatures (Figure 8). The synthetic oxidized and reduced smelts have lower emittances than industrial smelts because they do not contain any residual carbon or other contaminates that may increase emissivity. It also appears that total emittance is somewhat independent of the amount of sulfide oxidation, based on a comparison of oxidized and reduced synthetic smelts.

In contrast to smelt, salt cake dust and sintered fume deposits have a very low emittance (0.2 to 0.7), that decreases significantly with temperature (Figure 9). The high porosity, in combination with a high intrinsic transmissivity of the material, probably contributes to it's low emittance at low wavelengths due to internal scattering of transmitted radiation. This is a property of most dielectric materials including fly-ash deposits (Wall, et al., 1993). Consequently, furnace heat transfer and wall heat flux distribution are largely dependent on the physical characteristics, melting point and temperature of recovery boiler deposits.

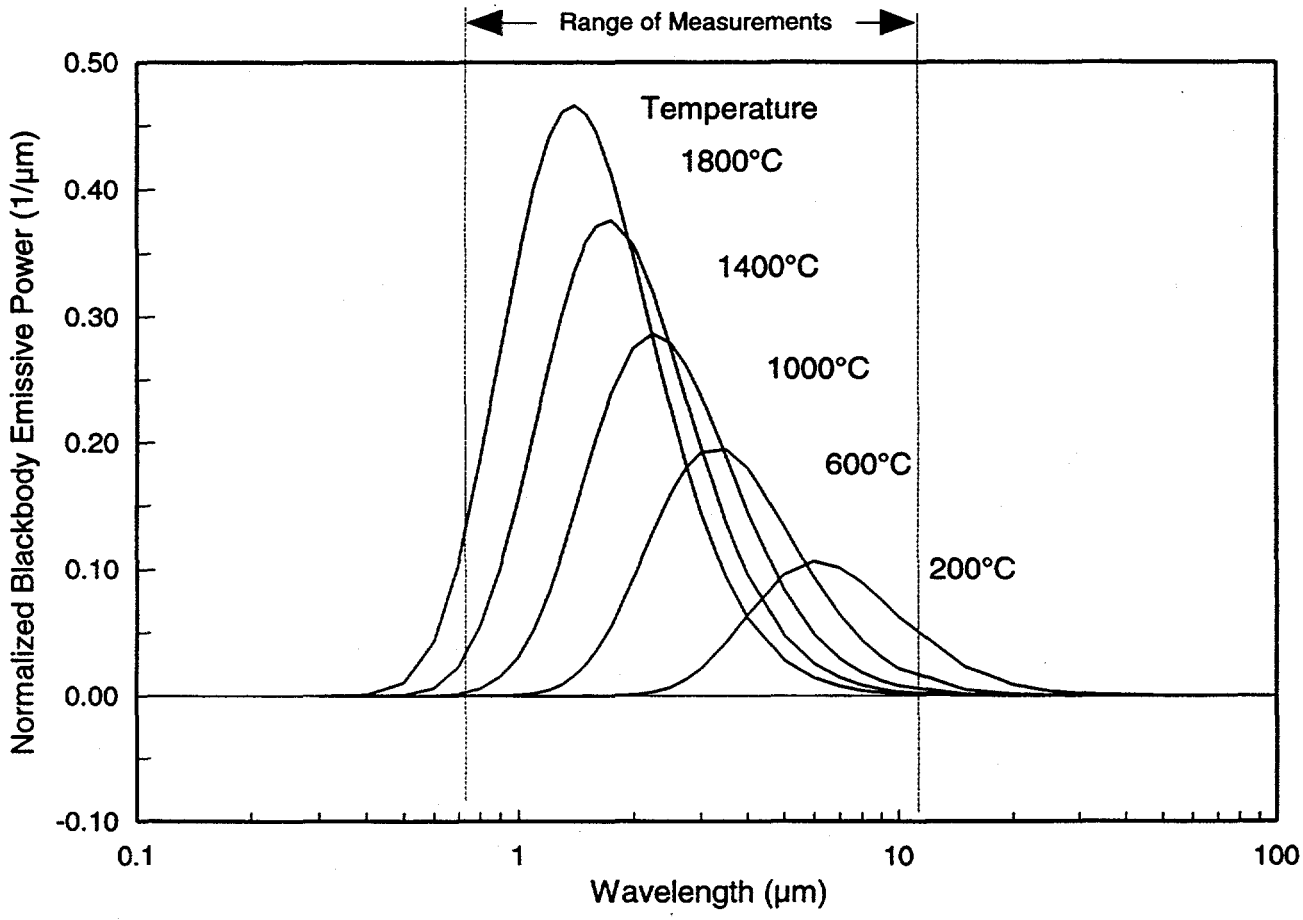

Figure 6. Blackbody Emissive Power for Different Temperatures

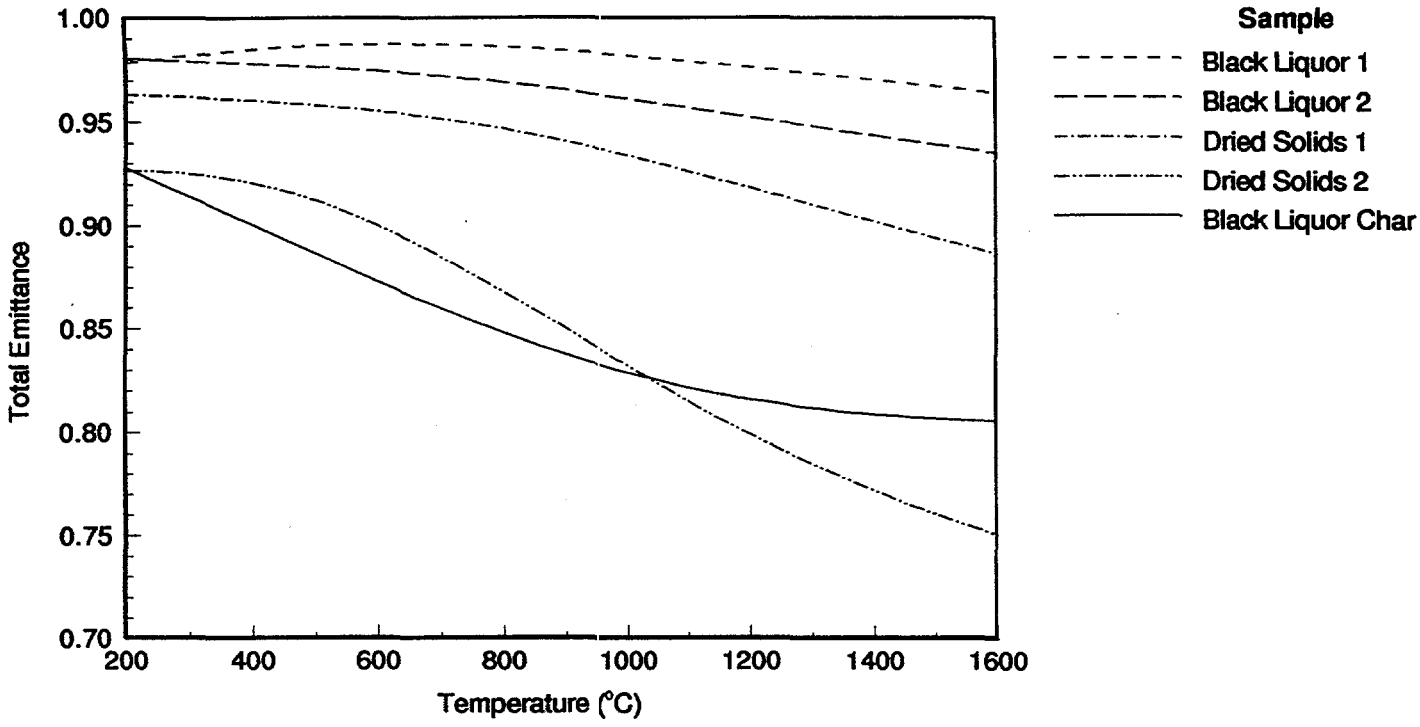

Figure 7. Total Emittance of Black Liquor, Dried Solids and Char

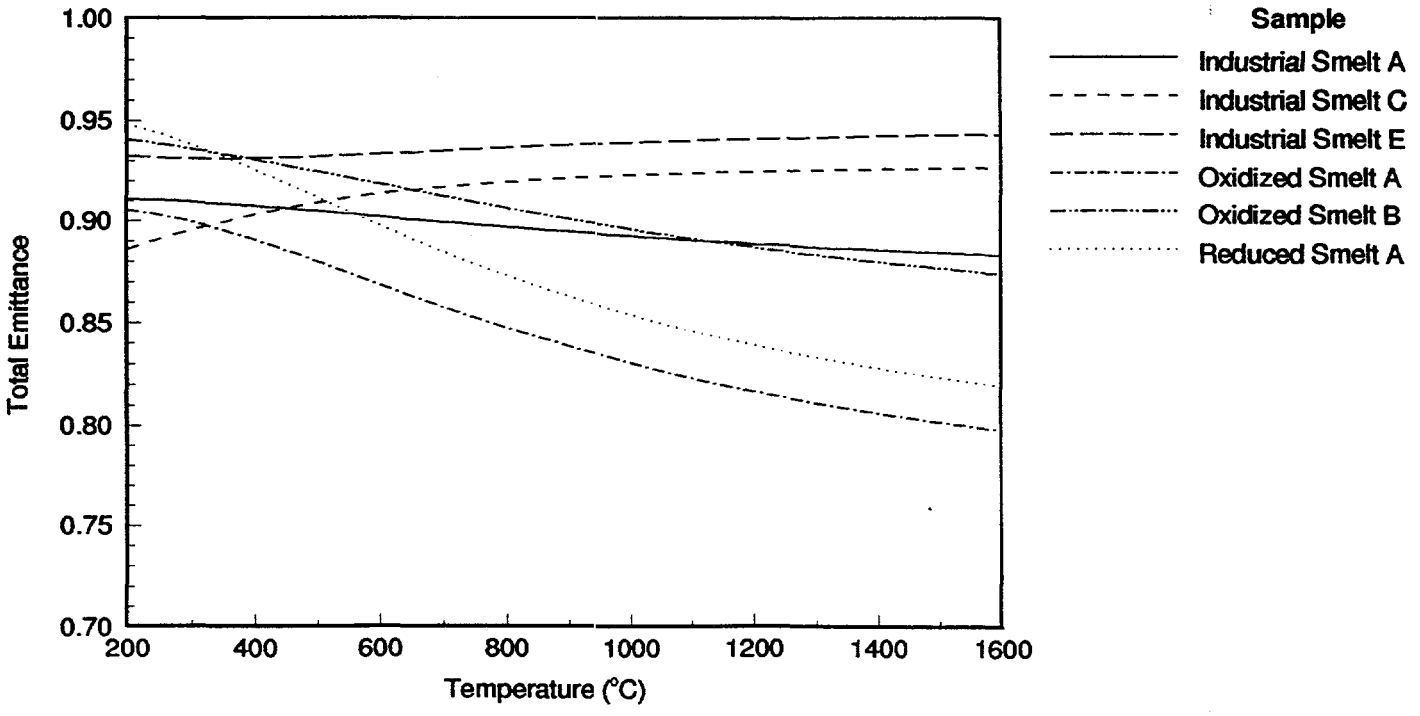

Figure 8. Total Emittance of Molten Smelt

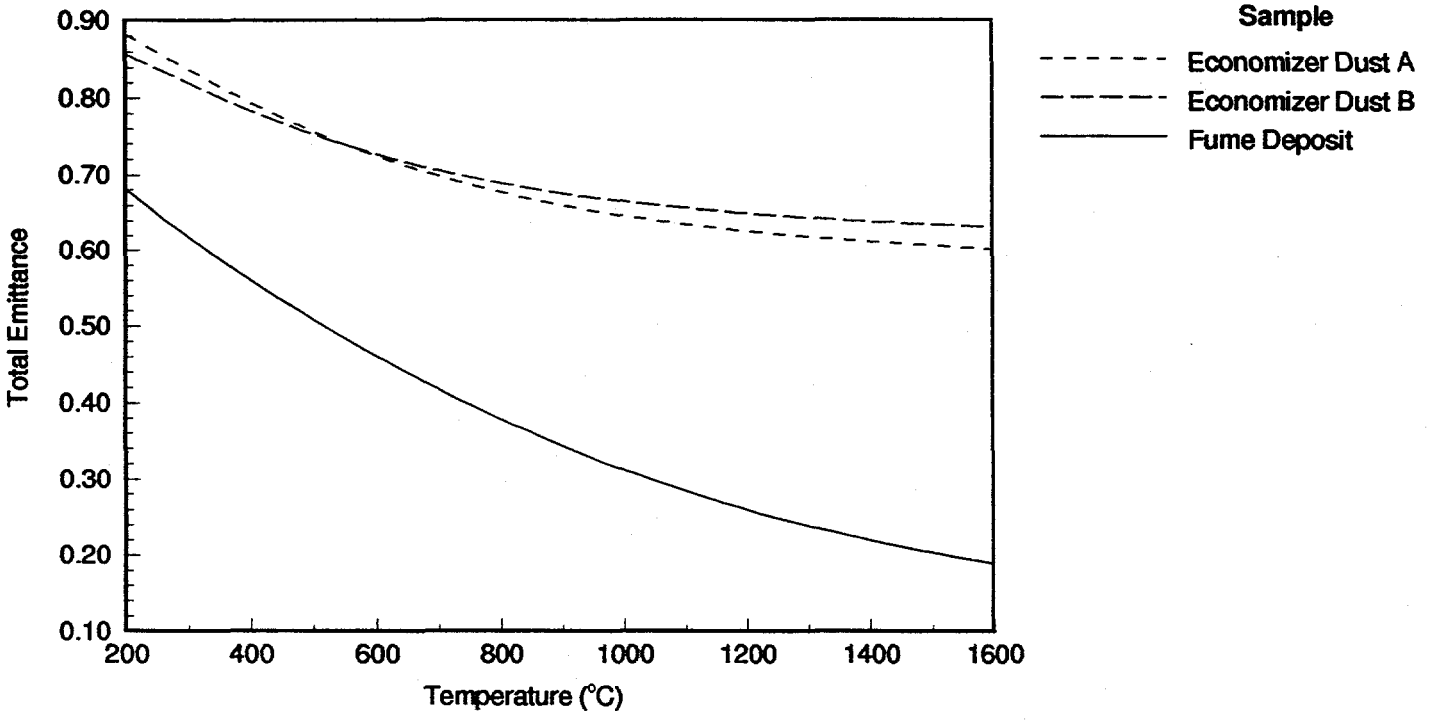

Figure 9. Total Emittance of Salt Cake

3.0 RADIATION PROPERTY CORRELATIONS

Engineering correlations for total emissivity as a function of temperature were developed by fitting polynomials to total emittance curves described in Section 2.5. Representative curves were selected when more than one sample was tested. The correlation constants are given in Table 5. The correlations fit total emittance curves with an R-squared better than 99.9% and standard error less than 0.1% for temperatures 200 to 1600°C, but can be reasonably extrapolated to temperatures as low as 100°C and as high as 1800°C. The results of the emissivity correlations are shown in Figure 10.

Table 5. Correlations for Total Emissivity and Absorptivity (373 < T < 2073°K)

Sample Description	C_0	C_1	C_2	C_3
Black Liquor (67 % Solids)	0.97009	4.3916×10^{-5}	-5.3758×10^{-8}	1.0892×10^{-11}
Dried Black Liquor Solids	0.94052	8.6109×10^{-5}	-9.3482×10^{-8}	1.7052×10^{-11}
Black Liquor Char	1.00570	-1.6336×10^{-4}	-4.1053×10^{-9}	1.8628×10^{-11}
Industrial Smelt	0.91898	-8.4206×10^{-6}	-1.8412×10^{-8}	6.8426×10^{-12}
Sintered Fume Deposit	1.05299	-9.3223×10^{-4}	3.2570×10^{-7}	-3.9692×10^{-11}

Emissivity: $\varepsilon(T_s) = C_0 + C_1T_s + C_2T_s^2 + C_3T_s^3$ T_s = Surface Temperature (°K)

Absorptivity: $\alpha(T_i) = C_0 + C_1T_i + C_2T_i^2 + C_3T_i^3$ T_i = Incident Radiation Temperature (°K)

The radiative properties for absorption and scattering by particles are needed for heat transfer calculations during black liquor drop combustion. The conditions for a black liquor drop in a recovery boiler are such that $d > 100\ \mu m$, $\lambda < 10\ \mu m$; therefore the large particle limit for diffraction of radiation ($\pi d/\lambda >> 1$; Bohren and Huffman, 1983) is usually satisfied. Under these conditions the emission, absorption and scattering efficiencies for spherical particles are given by:

$$
\begin{aligned}
Q_e &= \varepsilon(T_s) \\
Q_a &= \alpha(T_i) \\
Q_s &= 1 - \alpha(T_i)
\end{aligned}
\tag{3}
$$

Emission, absorption and scattering coefficients are given by:

$$
\begin{aligned}
\kappa_e &= \varepsilon(T_s)\, N \pi d^2/4 \\
\kappa_a &= \alpha(T_i)\, N \pi d^2/4 \\
\sigma &= \left[1 - \alpha(T_i)\right] N \pi d^2/4
\end{aligned}
\tag{4}
$$

These properties, with the properties of inorganic aerosol particles and radiating gases, are used to solve the radiative transport equation within the furnace (Fiveland and Jessee, 1994). In the above equations, d is the particle diameter and N is the number of particles per unit volume. The absorbance is evaluated at the source temperature of the incident radiation. If the total incident radiant energy (G in W/m^2) or incident radiant heat flux (q^+ in W/m^2) is known from the solution of the radiative transport equation, then the incident radiation temperature (T_i in °K) for the absorption coefficient can be approximated by assuming local radiative equilibrium:

$$
T_i = \sqrt[4]{\frac{G}{4\tilde{\sigma}}} \quad \text{or} \quad T_i = \sqrt[4]{\frac{q^+}{\tilde{\sigma}}} \tag{5}
$$

where $\tilde{\sigma}$ is the Stefan-Boltzmann constant (5.6696×10^{-8} $W/m^2\text{-}K^4$). The incident radiant energy, G, and incident radiant heat flux, q^+, are calculated from the radiant intensity vector $\vec{I}$:

$$
G = \int_{4\pi} \vec{I} \cdot d\vec{\Omega} \quad \text{and} \quad q^+ = \vec{I} \cdot \vec{n} \tag{6}
$$

where $d\vec{\Omega}$ is the differential solid angle in the direction $\vec{\Omega}$ and $\vec{n}$ is the unit normal vector for the surface.

Radiative heat transfer to the surface of a particle is calculated from the equation:

$$q_{rad} = \pi d^2(\alpha G/4 - \varepsilon\tilde{\sigma}T_s^4) \tag{7}$$

where T_s is the surface temperature and πd^2 is the particle surface area. Radiative heat transfer to a surface is:

$$q_{rad} = A_s(\alpha q^+ - \varepsilon\tilde{\sigma}T_s^4) \tag{8}$$

where A_s is the surface area.

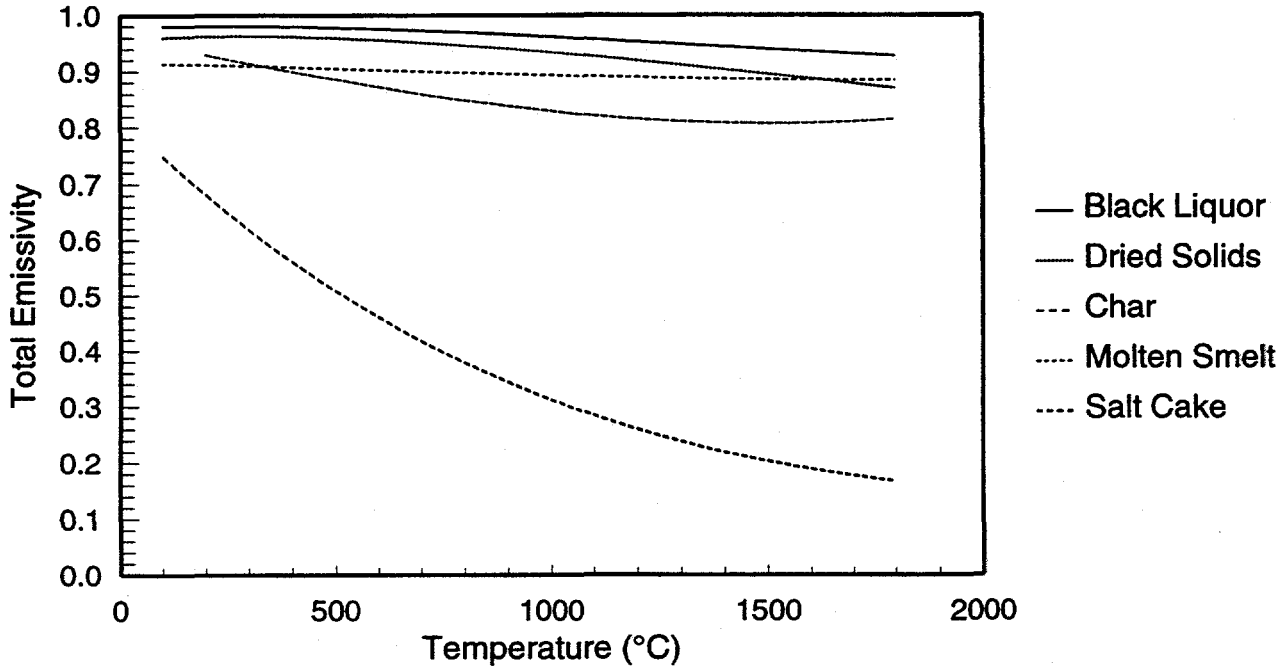

Figure 10. Emissivity Correlations for Black Liquor, Dried Solids, Char, Molten Smelt and Salt Cake

4.0 DROP HEAT TRANSFER AND COMBUSTION

Emissivity correlations were implemented into a model for heat transfer and combustion of single black liquor drops. The model was used to evaluate particle heat transfer for:

- drying and devolatilization of captive 2 mm drop in laboratory furnace at the Institute of Paper Science and Technology (IPST),

- drying and devolatilization of free-falling 0.1 mm particle in the Laminar Entrained Flow Reactor (LEFR) at Oregon State University (OSU),

- combustion of free-falling 2 mm drop at simulated recovery boiler conditions.

The furnace conditions and combustion parameters used in these model analyses are summarized in Table 6. The results of the model serve as a benchmark for others who wish to implement the radiative properties. Sensitivity studies were performed to determine the effect of radiative properties particle heat transfer and combustion results. The following sections describe these results.

4.1 SINGLE DROP COMBUSTION MODEL

A transient, one-dimensional model for black liquor drop combustion was previously developed to predict the heating rate and internal temperature gradients as a function of furnace temperature and particle size (Verrill and Wessel, 1995). The model accounts for drop aerodynamics, heat transfer, and chemical reaction. Reaction mechanisms for char burning and alkali release used in the model are described elsewhere (Verrill and Wessel, 1996) and are similar to those recommended by Wåg et al. (1995). The furnace environment (incident radiation, gas velocity, species, and temperature) is assumed uniform and invariant with time. The particle position can be fixed in space with a cross flow of gas as in a captive-drop furnace. Alternatively, the particle position and velocity can be permitted to vary with time based on aerodynamic drag and gravitational forces, simulating entrained flow reactor or actual recovery

Table 6. Furnace Conditions and Black Liquor Combustion Parameters Used in Model Analyses

	Captive Drop Furnace	Laminar Entrained Flow Reactor	Simulated Boiler Conditions
Furnace Conditions			
Gas Temperature (°C)	600,750,900	900	900,1000,1100
Gas Composition (% by Vol.)			
N2	95	100	66
O2			5
CO2			10
H2O			15
CO	5		2
H2			2
Gas Vertical Velocity (m/s)	0.61, 1.83	-0.279	1.0
Initial Drop Conditions			
Solids (%)	70.0	100.0	70.0
Temperature (°C)	115.0	115.0	115.0
Density (g/cm^3)	1.38	1.566	1.380
Diameter (mm)	2.0	0.10	2.0
Velocity (m/s)	0.0	-0.214	-10.0
Black Liquor Solids			
Elemental Composition (% Wt)			
Carbon	37.80	34.90	37.80
Hydrogen	3.60	3.05	3.60
Nitrogen	0.00	0.00	0.00
Sulfur	5.40	2.90	5.40
Sodium	19.30	22.65	19.30
Potassium	1.00	0.62	1.00
Chlorine	0.40	0.67	0.40
Oxygen	32.50	35.21	32.50
Higher Heating Value (kJ/kg)	14,500	13,000	14,500
Devolatilization Parameters			
Carbon Yield	0.40	0.53	0.40
Sulfur Yield	0.35	0.35	0.35
Initial Char Sulfate Reduction	0.54	0.54	0.54
Volumetric Swelling Factors			
Drying	3.375	1.0	3.375
Devolatilization	27.0	27.0	27.0

boiler conditions. The model is similar to the drop combustion model used in B&W's three-dimensional recovery furnace model (Wessel, et al., 1995; Wessel and Verrill, 1996), but includes more detail for radial heat transfer and temperature distribution within the drop, and can be run independently of the time consuming, full-furnace simulation.

Emissivity and absorptivity correlations for black liquor (Table 4) were implemented in the model as a function of surface composition, surface temperature and incident radiation temperature. The transition from black liquor to dry solids properties was approximated by linear interpolation of property correlations with amount of solids. A step change from dried solids to char properties is assumed to occur when devolatilization is complete. The transition from char properties to smelt is assumed to occur at the end of char burning. Smelt properties are used through out the remainder of the calculation assuming that properties do not change with smelt oxidation and solidification. The radiative properties of lignite coal or constant emissivity (and absorptivity) can also be specified for evaluating model sensitivity.

4.2 2 mm CAPTIVE DROPS

Black liquor combustion experiments were previously conducted at the Institute of Paper Science and Technology (IPST) in a tube furnace (Verrill, et al., 1994). Individual drops of industrial black liquors, of 2 mm average initial diameter, were formed on a fine wire and inserted into the laboratory furnace with a relative gas velocity of 0.61 and 1.83 m/s and at temperatures of 600, 750 and 900°C. After 5-60 seconds exposure to a pyrolytic environment (95% N_2 with 5% CO), the char was withdrawn and quenched with nitrogen gas. Timed observation of drop behavior in the furnace was recorded on video tape in the IPST experiments and characteristic combustion times were determined.

Heat transfer was predicted for drying and devolatilization of 2 mm captive drops simulating the conditions in the IPST tube furnace. The combustion stage times calculated by the single drop model are compared to measured values in Table 6. While it is not possible to identify the beginning and ending points of drying and devolatilization from captive-drop experiments, the times to the onset of swelling and maximum swollen volume (MSV) can be

precisely measured. A parameter for internal radiative heat transfer was adjusted to provide the best fit with experimental times to MSV. Modeling parameters were then held constant for all other simulations. Considering the range of experimental variability, the model accurately predicts the time to MSV for captive drops in a flowing, non-combustive gas. The onset of swelling, determined from the video images, falls between the predicted beginning of devolatilization and the end of drying.

Table 7. Comparison of Measured and Predicted Drop Combustion Times*

Temperature (°C)	Gas Velocity (m/s)	Predicted beginning of devol.	Measured onset of swelling	Predicted end of drying	Predicted time to MSV	Measured time to MSV
600	0.61	0.82	3.8 ± 0.6	5.48	6.25	6.4 ± 1.0
750	0.61	0.39	1.9 ± 0.2	3.51	3.62	3.2 ± 0.3
750	1.83	0.30	1.9 ± 0.2	3.11	3.21	3.2 ± 0.3
900	0.61	0.22	1.2 ± 0.2	2.30	2.33	2.3 ± 0.4

*All times in seconds

Figure 11 shows predicted heat transfer results for drying and devolatilization of a 2 mm captive drop at 900°C. The stages of drying and devolatilization are not distinct, but overlap significantly due to steep temperature gradients within the particle. The center of the particle is still drying at the saturation temperature of black liquor, while the outside layers undergo devolatilization and char burning. Radiation comprises the most significant mode of heat transfer to the particle surface. Heat transfer increases significantly with surface area as the particle swells to MSV then decreases to zero as the particle approaches the furnace temperature. The particle becomes uniform in temperature after about 2.3 seconds, when devolatilization is complete.

The effect of particle emissivity on drop heat transfer during drying and devolatilization of a 2 mm captive drop is shown in Figure 12. The radiative properties for black liquor, lignite

coal and constant emissivity (ε = 0.7, 0.8, 0.9 and 1.0) were use in the model. Emissivity has a large effect on drying and devolatilization times for large drops because radiation is the dominate mode of heat transfer to the particle surface. For black liquor and lignite coal properties, a step change in emissivity occurs at approximately 2 seconds because char burning begins in the outer most layer of the particle, and the emittance properties of char are used. Drying and devolatilization times vary by 20 % for the range of properties considered. The results for constant emissivity of 0.9 are closest to those using black liquor property correlations.

4.3 0.1 mm ENTRAINED PARTICLES

Heat transfer was predicted for combustion of 0.1 mm dried black liquor particles simulating conditions in the laminar entrained flow reactor (Reis, et al, 1995). Experiments in the LEFR used dry black liquor solids, 90-125 μm, in nitrogen with 0% O_2, 4%O_2 and 21% O_2 environments at furnace temperatures ranging from 700 to 1100°C. The particle heating rate was of the order of 10^4-10^5°C per second, and the residence time was 0.6 to 0.8 seconds. The samples were quenched to stop the reactions, the solid products of combustion were collected and chemically analyzed. Characteristic combustion times, swollen volume, and particle temperature were not measured.

Figure 13 shows predicted heat transfer results for devolatilization of a 0.1 mm free falling particle at 900°C in 100% N_2, 0.279 m/s co-flowing gas. In contrast to large drops, the temperature is nearly uniform within the particle and convection is the most significant mode of heat transfer to the particle surface. Heat transfer is initially positive as the particle heats up, becomes negative when the particle exceeds the furnace temperature, then approaches zero as the particle approaches the furnace temperature. The particle temperature exceeds the furnace temperature near the end of devolatilization because devolatilization is slightly exothermic in the model. Devolatilization is completed quickly (0.061 seconds) compared to the particle residence time when the solid products are collected (0.70 seconds).

The effect of emissivity on particle heat transfer during devolatilization of a 0.1 mm free falling particle is shown in Figure 14. The radiative properties for black liquor, lignite coal and

constant emissivity ($\varepsilon = 0.7$ and 1.0) were use in the model. In contrast to large drop results, emissivity has very little effect on devolatilization times for small particles because radiation is not the dominate mode of heat transfer to the particle surface. Devolatilization times vary by 2.5 % for the range of properties considered.

4.4 RECOVERY BOILER CONDITIONS

The drop combustion model was used to predict the combustion behavior of a 2 mm free falling drop at recovery boiler conditions. A gas atmosphere of 66% N_2, 5% O_2, 10% CO_2, 15% H_2O, 2% CO and 2% H_2 at 900, 1000 and 1100°C were chosen as typical conditions. The particle is released with an initial downward velocity of -10 m/s in a uniform upward flowing gas at 1 m/s. The particle continues to react until the end of smelt oxidation, even though it would most likely impact a wall or the char bed before the end of char burning in an actual boiler.

Predicted combustion times are shown in Table 8. Drying and devolatilization at 900°C are completed more rapidly than in the IPST laboratory furnace due to initially higher heating rates from convective heat transfer. These effects may be exaggerated by the idealized conditions used in the model, because significant gradients in gas temperature and velocity are known to exist near a black liquor nozzle. Predicted times for char burning are in reasonable agreement with predictions made with a less detailed model for black liquor char combustion. (Wåg, et al., 1995), considering the differences in liquor composition and devolatilization parameters that were used.

Figure 15 shows detailed results for combustion of a 2 mm free falling drop at 1000°C. Behavior during drying and devolatilization is similar to the results for the captive drop furnace. During char burning, the particle temperature remains at approximately 900°C due to the endothermic reactions of gasification by CO_2 and H_2O and alkali sulfate reduction. After char burning, the particle is heated above the surrounding gas temperature due to the exothermic reaction of alkali sulfide oxidation. The particle temperature approaches the surrounding gas temperature after smelt oxidation is completed. Radiation is the dominate mode of heat transfer to the particle surface.

Table 8. Predicted Drop Combustion Times at Recovery Boiler Conditions*

Temperature (°C)	End of Drying	Time to MSV	End of Devolatil-ization	95% Carbon Burnout	100% Carbon Burnout	End of Smelt Oxidation
900	1.59	1.59	1.64	6.15	7.80	9.30
1000	1.32	1.29	1.35	3.82	5.19	7.28
1100	1.12	1.04	1.13	2.51	3.47	5.78

*All times in seconds

The effect of particle emissivity on drop heat transfer is shown in Figure 16 for radiative properties of black liquor, and constant emissivity values of 0.7 and 1.0. Similar to the captive drop furnace results (Section 4.2), emissivity has a large effect on drying and devolatilization times. Reaction times to the end of char burning and smelt oxidation also vary by approximately 0.5 seconds (10 to 15%) for the range of emissivity considered. For the radiative properties of black liquor, a step change in emissivity occurs at approximately 1 second because char burning begins in the outer most layer of the particle, and the properties of char are used in the model. A step change in emissivity also occurs at the end of char burning (approximately 5 seconds) because smelt properties are used. These sudden transitions are consistent with the rapid changes observed during black liquor drop combustion experiments.

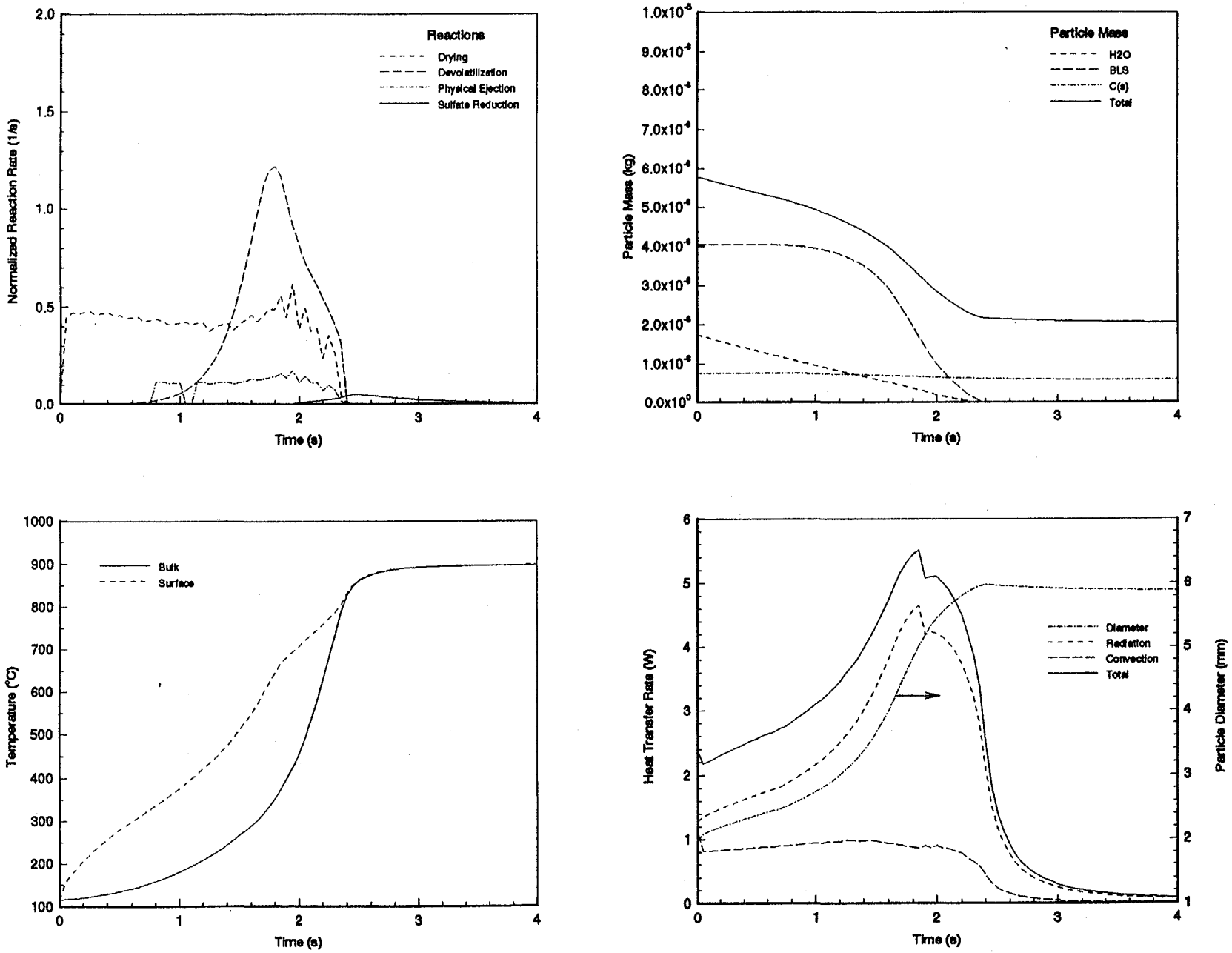

Figure 11. Drying and Devolatilization of 2 mm Captive Drop at 900°C, 95% N_2, 5% CO, 0.61 m/s

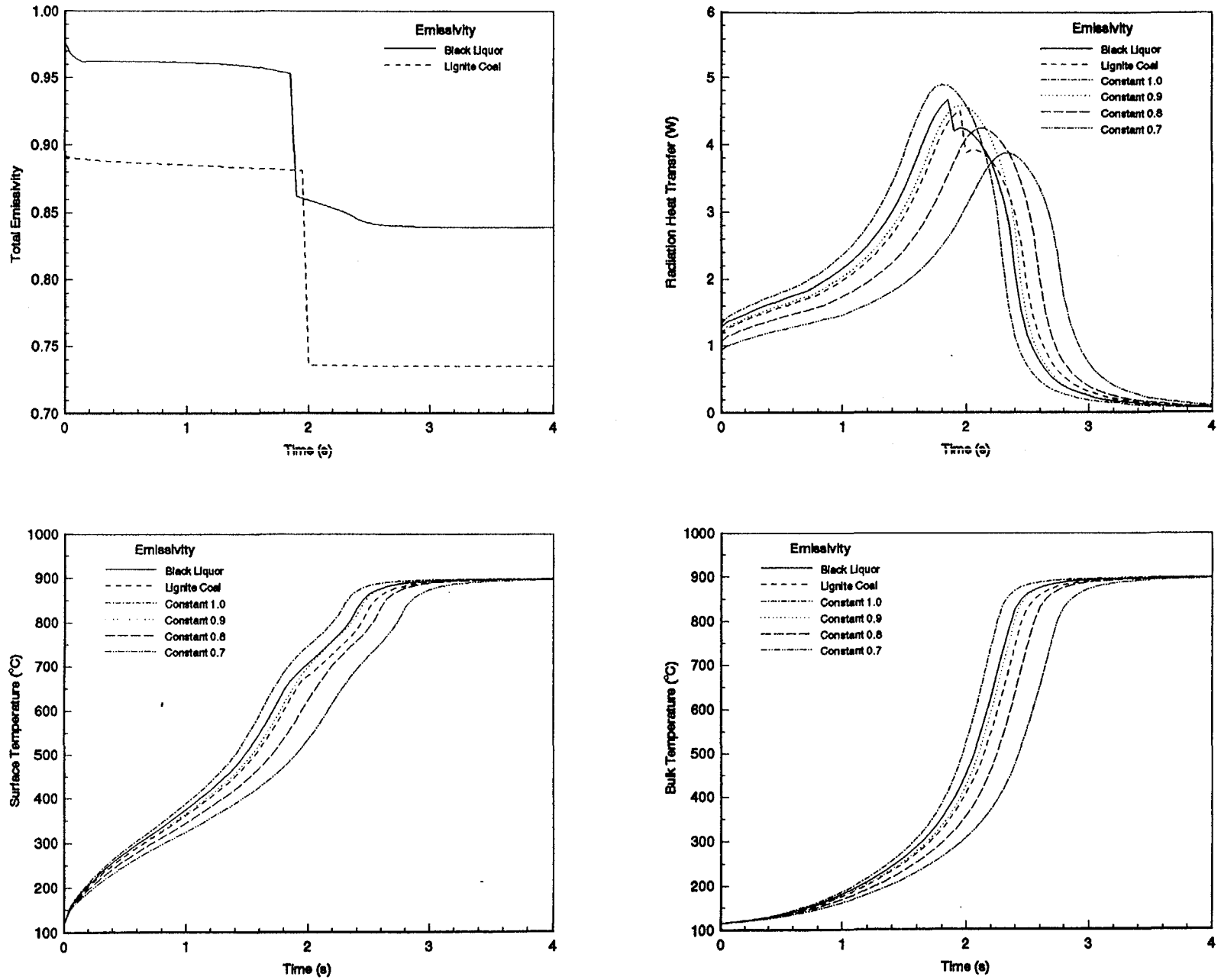

Figure 12. Effect of Emissivity on Heat Transfer of 2 mm Captive Drop at 900°C, 95% N_2, 5% CO, 0.61 m/s

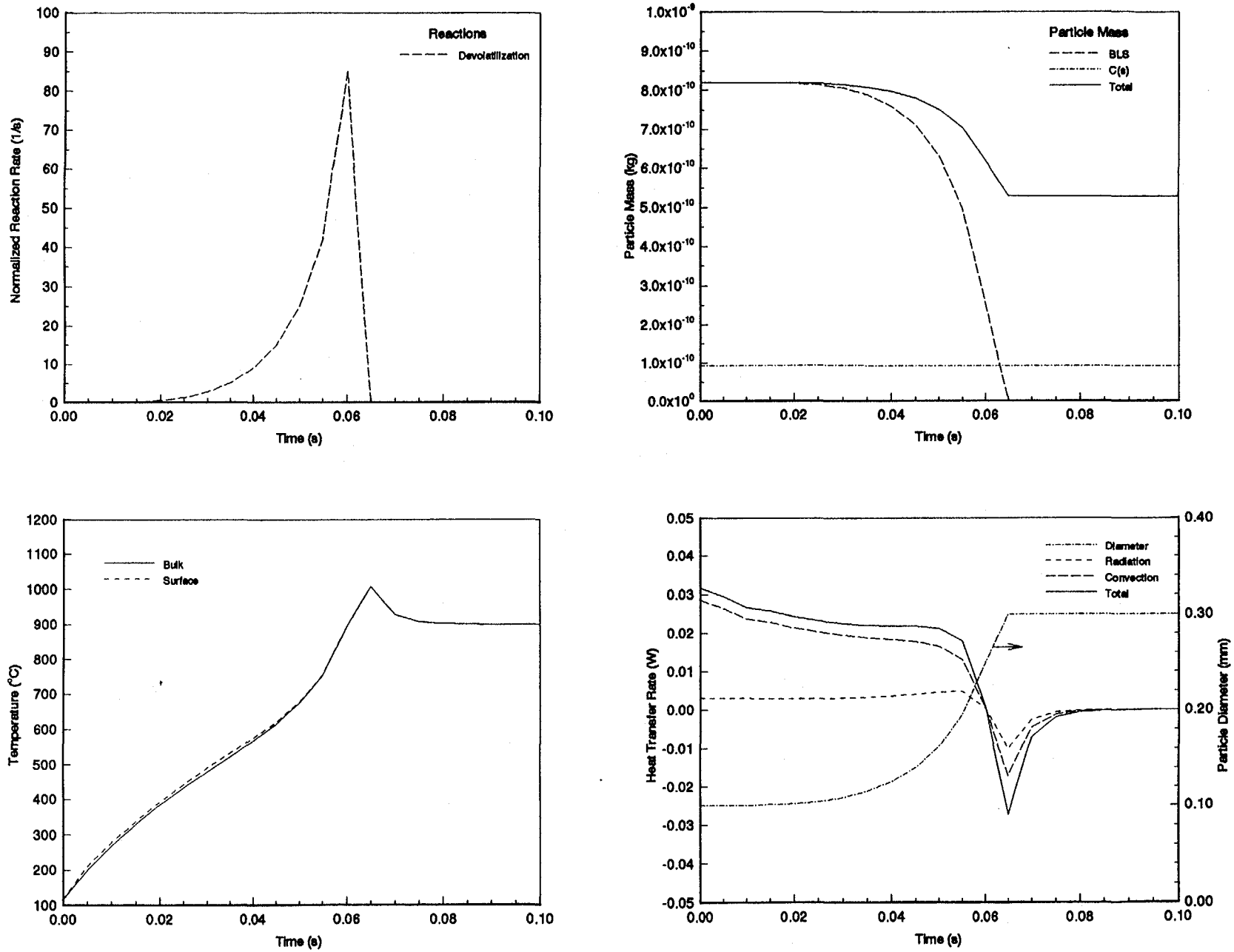

Figure 13. Devolatilization of 0.1 mm Falling Particle at 900°C, 100% N_2

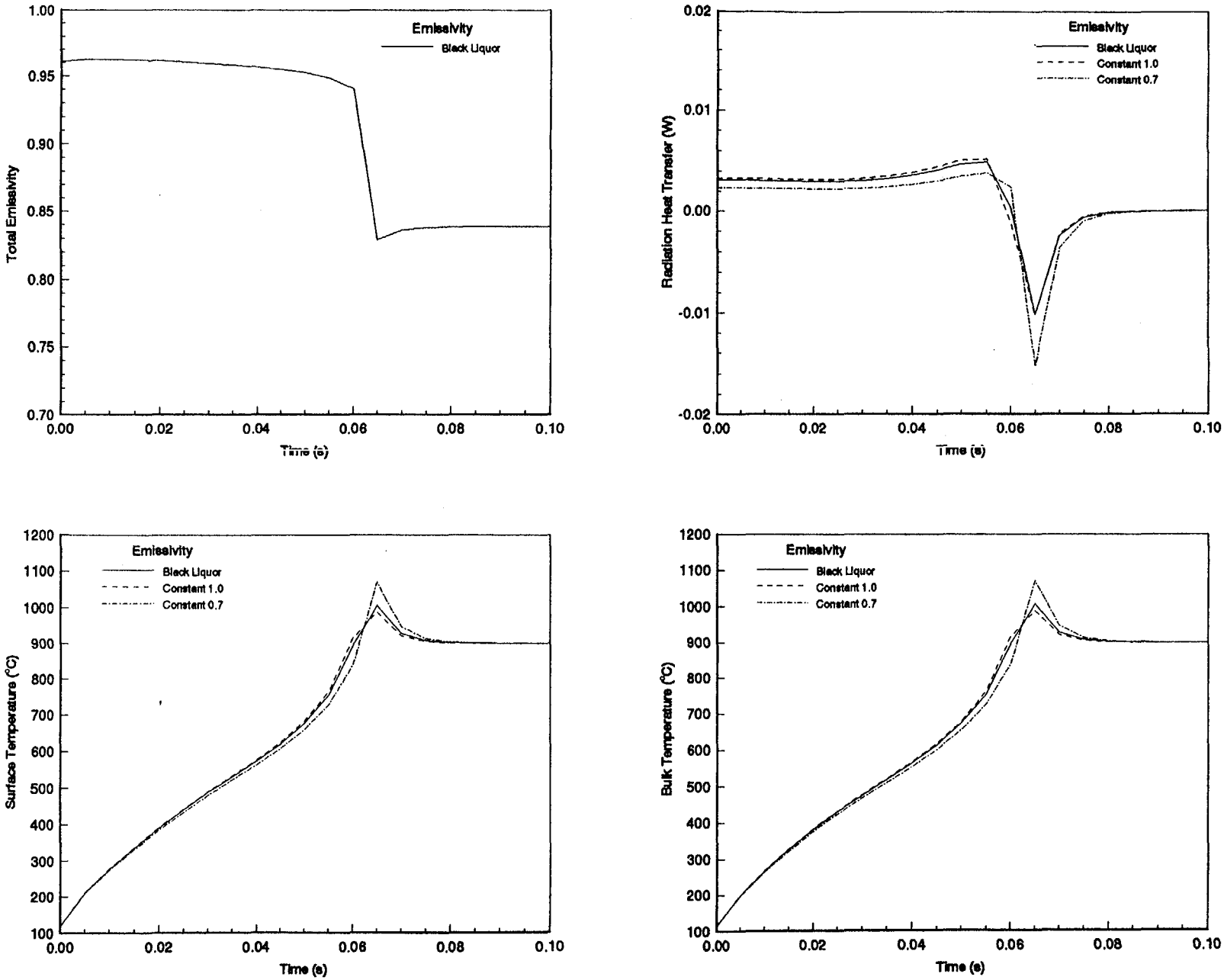

Figure 14. Effect of Emissivity on Heat Transfer of 0.1 mm Falling Particle at 900°C, 100% N_2

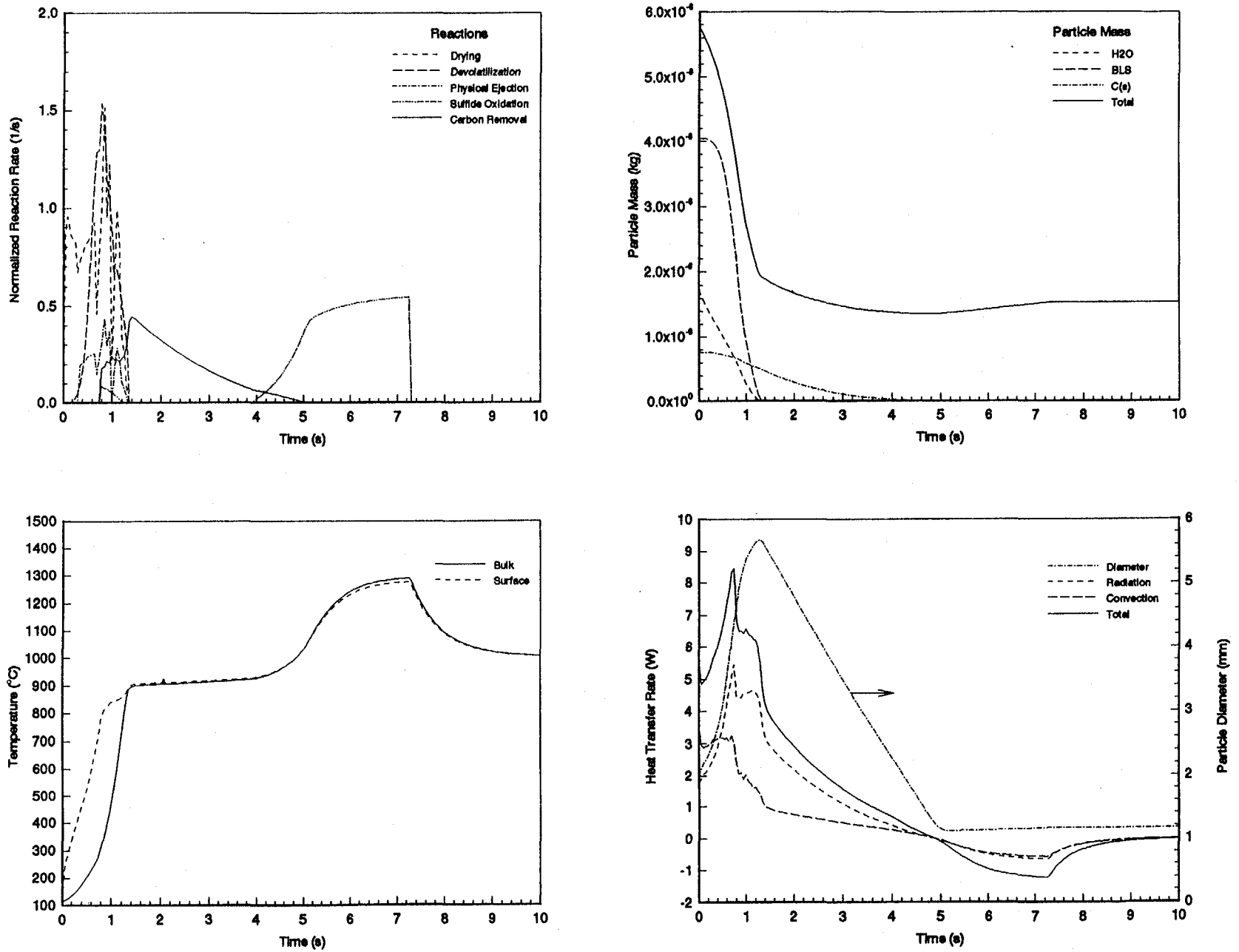

Figure 15. Combustion of 2 mm Falling Drop at Recovery Boiler Conditions
1000°C, 66% N_2, 5% O_2, 10% CO_2, 15% H_2O, 2% CO, 2% H_2

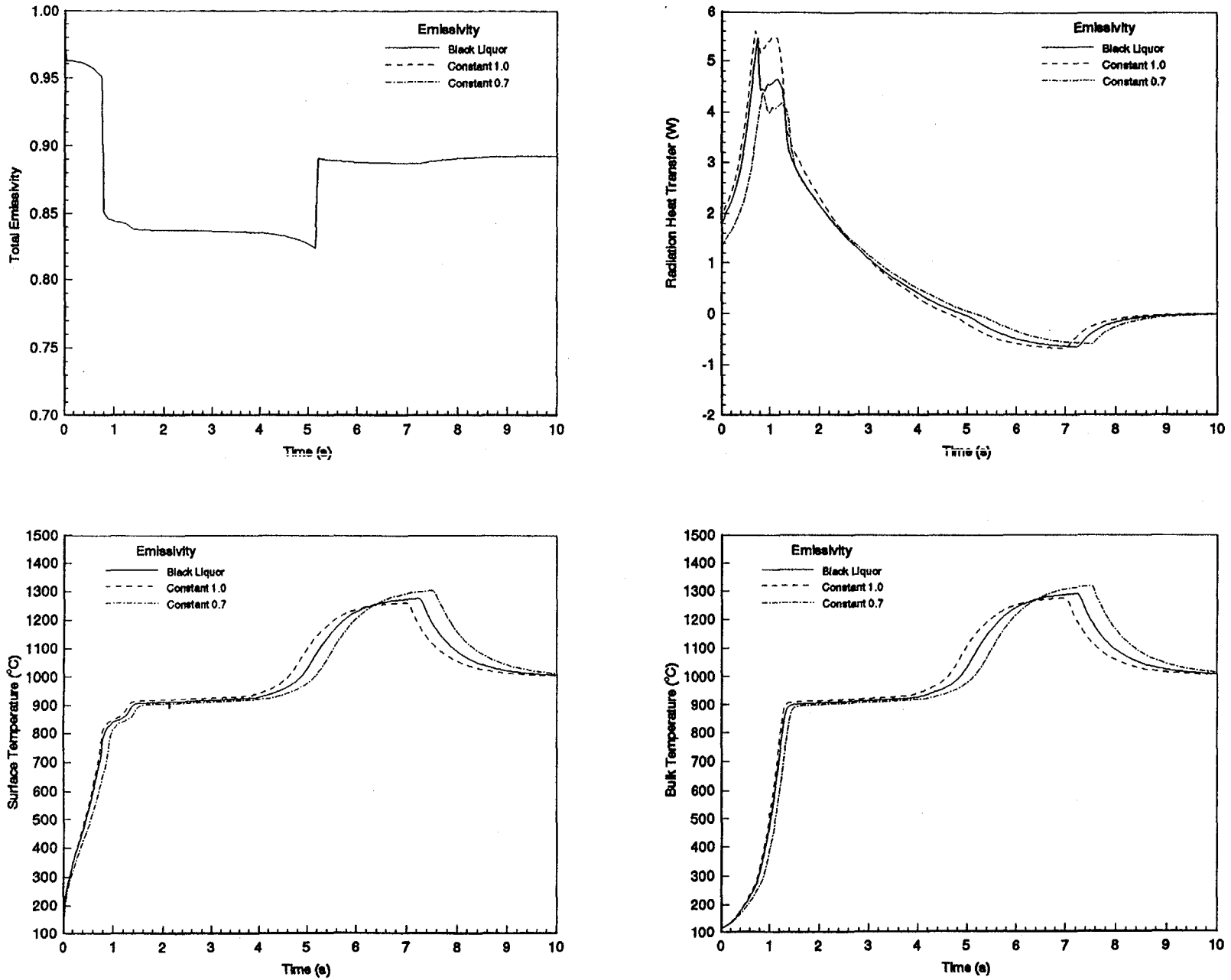

Figure 16. Effect of Emissivity on Heat Transfer of 2mm Falling Drop at Recovery Boiler Conditions 1000°C, 66% N_2, 5% O_2, 10% CO_2, 15% H_2O, 2% CO, 2% H_2

5.0 CONCLUSIONS AND RECOMMENDATIONS

Spectral emittance measurements of black liquor, dried solids, char, molten smelt and salt cake were successfully completed. The uncertainty in these measurements is 6 to 7 percent for wavelengths 1 to 5 μm and about double for wavelengths greater than 6 μm. For high temperature emittance measurements, additional uncertainty was introduced at wavelengths below 3 μm because molten smelt and salt cake samples were partially transparent. Calculated total emittances are valid for temperatures 200 to 1600°C in which spectral data span most of the blackbody spectrum.

Engineering correlations were successfully developed for radiation properties of black liquor, dried solids, char, molten smelt and salt cake for temperatures 100 to 1800°C. The correlations fit total emittance curves with an R-squared better than 99.9% and standard error less than 0.1% for temperatures 200 to 1600°C, but can be reasonably extrapolated to temperatures as low as 100°C and as high as 1800°C. Correlations for total emissivity and absorptivity should be used to calculate surface radiation heat transfer. Equations for particle emission, absorption and scattering coefficients should be used to calculate heat transfer for black liquor drop combustion. Particle properties are valid for the large particle limit ($\pi d/\lambda >> 1$) typical of black liquor spray combustion in recovery boilers ($d > 100$ μm, $\lambda < 10$ μm).

Radiation properties have a large effect on predicted burning times for conditions used in captive drop experiments and for combustion of 2 mm drops at simulated recovery boiler conditions. Therefore, accurate radiation properties are needed to understand and interpret experimental results for black liquor combustion, and to predict heat transfer and combustion of black liquor spray in numerical models of a recovery furnace. Modeling results for heat transfer and combustion of single black liquor drops should be used as a benchmark for others who wish to implement the radiative properties.

Radiation properties also have a large effect on furnace heat flux distribution because they are dependent on the physical characteristics, melting point and temperature of recovery boiler deposits. A large decrease in total emittance is expected to occur at the transition from

molten smelt to powderous salt cake (fume) deposits on the furnace walls and convective surfaces. The highly porous nature of fume deposits probably contributes to it's low emittance at low wavelengths, due to internal scattering of transmitted radiation.

Radiative properties characterized in this work provide some of the basic tools needed to calculate heat transfer in recovery boilers. However, additional work is needed to characterize radiative properties of gas entrained aerosol particles and to continue characterization of thermal and radiative properties of inorganic deposits. Radiative properties of inorganic aerosol are needed to understand the effect of gas-entrained, submicron fume particles on furnace heat transfer. More detailed measurements are needed to characterize radiation properties of partially transparent materials (smelt and fume deposits) over a range of conditions (temperature, chemical composition, physical characteristics, layer thickness and substrate materials).

6.0 REFERENCES

Bohren, C.F. and D.R. Huffman, *Absorption and Scattering of Light by Small Particles*, John Wiley and Sons, New York, (1983).

Edwards, D.K. and A. Balakrishnan, "Thermal Radiation from Combustion Gases," *International Journal of Heat and Mass Transfer,* Vol. 16, pp.25-40, (1973).

Fiveland, W.A. and J.P. Jessee, "Comparison of Discrete Ordinates Formulations for Radiative Heat Transfer in Multidimensional Geometries," Journal of Thermophysics and Heat Transfer, **9**(1), 1994.

Frederick, W.J., "Combustion Processes in Black Liquor Recovery: Analysis and Interpretation of Combustion Rate Data and an Engineering Design Model, Report No. 1," *Department of Energy Report,* DOE/CE/40637-T8, (1990).

Frederick, W.J. and M. Hupa, "Combustion Properties of Kraft Black Liquors," Department of Energy Report, DOE Contract No. DE-FG02-90CE40936, (1993).

Nowak, P., Matys, P. Sabhapath, P. Abdullah, Z. and M. Salcudean, "Numerical Study of a Kraft Recovery Furnace," *Proceedings TAPPI/CPPA International Chemical Recovery Conference*, Toronto (1995).

Reis, V.V., Frederick W.J., Wåg, K.J., Iisa, K., and S.A. Sinquefield, "Effects of Temperature and Oxygen Concentration on Potassium and Chloride Enrichment During Black Liquor Combustion," *Tappi Journal*, 78(12):67-76 (December, 1995).

Siegel, R. and J.R. Howell, *Thermal Radiation Heat Transfer*, 2nd Ed., McGraw Hill, New York, (1981).

Wåg, K.J., Frederick, W.J., Grace, T.M., and M. Kymäläinen, "Sulfate Reduction and Carbon Removal During Kraft Char Burning," *Proceedings TAPPI/CPPA International Chemical Recovery Conference*, Canadian Pulp and Paper Association, Montreal p. B89 (1995).

Wall, T.F., Bhattacharya, S.P., Zhang, D.K., Gupta, R.P. and X. He, "The Properties and Thermal Effects of Ash Deposits in Coal-Fired Furnaces," *Progress in Energy and Combustion Science*, **19**, pp. 487-504 (1993).

Wessel, R.A., Parker, K.L., and Akan-Etuk, A., "Three-Dimensional Model of a Kraft Recovery Furnace," *Tappi Engineering Conference,* Orlando, Florida (1993).

Wessel, R.A., Parker, K.L., and C.L. Verrill, "Three-Dimensional Kraft Recovery Furnace Model; Implementation and Results of Improved Black Liquor Combustion Models," *Tappi Engineering Conference*, Dallas, Texas (1995).

Wessel, R.A. and C.L.Verrill, "Validation of Combustion and Fume Formation Models for an Operating Kraft Recovery Boiler," *Tappi Engineering Conference*, Chicago, Illinois (1996).

Verrill, C.L. and R.A. Wessel, "Sodium Loss During Black Liquor Drying and Devolatilization - Application of Modeling Results to Understanding Laboratory Data," *Proceedings TAPPI/CPPA International Chemical Recovery Conference*, Toronto, Ontario (1995).

Verrill, C.L. and R.A. Wessel, "Detailed Model of Alkali Release During Black Liquor Drop Combustion," submitted to Tappi Journal, September (1996).

Verrill, C.L., Grace, T.M., and K.M. Nichols, "The Significance of Sodium Release During Devolatilization on Fume Formation in Kraft Recovery Boilers," *J. Pulp Paper Sci.* 20 (12):J354-J360 (1994).

APPENDIX A
FACILITIES AND TECHNIQUES

A.1 SPECTRAL EMITTANCE

Spectral and total emittance measurements for this project were performed at the High Temperature Spectral Emittance Measurement Facility. The facility consists of a high temperature furnace, optics including a grating monochromator, a series of photodetectors, and a personal computer-based data acquisition system. Figure 2 is a schematic of the facility.

The method used at the Spectral Emittance Measurement Facility to determine the spectral emittance of a surface requires instrumentation to measure the temperature of the emitting surface and to measure the intensity of the emitted radiation by wavelength. Additionally, a radiation standard is required to provide a calibration source for the instrumentation.

The sample is heated from behind using the high-temperature furnace at the facility. The furnace is designed to heat 2-inch square samples. When necessary, a 2-inch square metal plate is used to support the sample. The sample is heated to the desired temperature as measured using thin gauge thermocouples and/or a hand-held pyrometer.

A gold-plated mirror and zinc selenide lens are used to collect and image energy radiated from the sample surface onto the input slit of the grating monochromator. The ruled grating in the monochromator diffracts incoming radiant energy into a spectral continuum, which is imaged at the output slit. Different wavelengths are passed through the slit by rotating the angle of the monochromator using a stepper motor drive. The selected wavelength was measured using a precision potentiometer located internal to the monochromator.

Each ruled grating for the monochromator spanned a wavelength range of about 3:1. Four different gratings were used to span the wavelength range from 0.6 to 14.4 μm, which also provides overlap between gratings.

To prevent measurement errors caused by second-order diffraction, order sorting filters (essentially high-pass filters) are set in front of the input slit of the monochromator. One of four filters is selected, depending on the wavelength of light measured.

Three photodetectors are used to measure light intensities from 0.6 to 14.4 μm. A room-temperature silicon/germanium detector sandwich spans the range from 0.6 to about 1.8 μm; a liquid nitrogen-cooled indium-antimonide/mercury-cadmium-telluride (InSb/HgCdTe) dual detector sandwich is used to measure light intensities from about 1.4 to 14.4 μm. AC coupling in the pre-amp circuits of the InSb/HgCdTe detectors requires modulation of the incident light energy. This was accomplished using a shutter operating at a frequency of about 40 Hz.

The thermopile detector that was used to measure total emittance directly has a spectrally neutral coating that is highly absorptive from 0.2 to greater than 50 μm. To protect the sensing element, the detector is covered with a zinc selenide window that yields an effective wavelength range of about 0.6 μm to about 18 μm.

The method for experimentally measuring spectral emittance from high temperature surfaces is based on Planck's law for blackbody radiation:

$$E_{b\lambda}(\lambda,T) = \frac{C_1 \lambda^{-5}}{e^{C_2/\lambda T} - 1} \qquad \text{(A-1)}$$

where:

$E_{b\lambda}(\lambda,T)$ = monochromatic emissive power of a blackbody

λ = wavelength (μm)

T = absolute temperature (K)

C_1 = 3.74×10^4 (W-μm^4/cm^2)

C_2 = 1.44×10^4 (μm-K)

If T and λ are known, $E_{b\lambda}(\lambda,T)$ may be calculated and compared with the measured radiation from the sample. The emittance of the sample is generally a function of wavelength, temperature, angle, and possibly time. The surface normal spectral emittance at any temperature is:

$$\varepsilon_\lambda = \frac{E_\lambda(\lambda,T)}{E_{b\lambda}(\lambda,T)} \qquad \text{(A-2)}$$

where $E_\lambda(\lambda,T)$ is the measured radiation from the deposit surface at a temperature (T), and wavelength (λ) and $E_{b\lambda}(\lambda,T)$ are defined in Equation A-1. Thus, for a blackbody, $\varepsilon_\lambda = 1$. To obtain the total emittance of the deposit, Equation A-2 is integrated over all wavelengths:

$$\varepsilon = \frac{1}{\tilde{\sigma}T^4}\int_0^\infty \varepsilon_{(\lambda)} E_{b\lambda}(\lambda,T)\, d\lambda \qquad \text{(A-3)}$$

In practice, ε_λ is measured over a limited wavelength range that represents most of the emitted energy. For temperatures between 700°-2200°F (371°-1204°C), more than 90 percent of the emitted radiation is within the wavelength range of 0.7 to 14.4 μm.

Data Acquisition and Reduction

Before testing, the optical instrumentation is calibrated using a blackbody radiation source. In this procedure, the blackbody source is set up as the sample, and data is recorded as in a normal test. This calibration data at each wavelength is then normalized using Planck's blackbody radiation equation evaluated at the temperature of the blackbody standard. Calibration constants, C_λ, are then determined as:

$$C_\lambda = \frac{V_{pd}}{E_{b\lambda}(\lambda,T)} \qquad \text{(A-4)}$$

where V_{pd} is the measured photodetector voltage. Sets of calibration constants are determined this way for each of the photodetectors and for each of the monochromator gratings.

The total radiation pyrometer is calibrated similarly, where the thermopile voltage output generated by viewing a blackbody source is measured at several different temperatures. Since the thermopile is responsive to total radiation, the measured signal is normalized by the Stefan-Boltzman equation. Thus, the thermopile calibration constant is evaluated as:

$$C_t = \frac{V_t}{\tilde{\sigma}T^4} \tag{A-5}$$

where V_t is the measured thermopile signal, $\tilde{\sigma}$ is the Stefan-Boltzman constant, and T is the absolute temperature of the blackbody standard.

Test data are reduced using the calculated calibration constants and the measured surface temperature of the sample. The spectral emittances are calculated as:

$$\varepsilon_\lambda = \frac{V_{pd}}{C_\lambda E_{b\lambda}(\lambda,T)} \tag{A-6}$$

The spectral emittance values are then screened and averaged at regions of overlap to arrive at a set of spectral emittances as a function of wavelength.

The total emittance is determined from the thermopile data as,

$$\varepsilon = \frac{V_t}{C_t \tilde{\sigma}T^4} \tag{A-7}$$

where C_t is the calibration constant for the thermopile and is determined from Equation A-5.

The total emittance is also calculated from the spectral data by integrating the spectral emittance over all measured wavelengths. Thus,

$$\varepsilon = \frac{\int_{\lambda 1}^{\lambda 2} \varepsilon_\lambda E_{b\lambda}(\lambda,T)\,d\lambda}{\int_{\lambda 1}^{\lambda 2} E_{b\lambda}(\lambda,T)\,d\lambda} \tag{A-8}$$

Equation A-8 can be evaluated at the test temperature to calculate an integrated total emittance for direct comparison to that determined using Equation A-7. Provided that the spectral emittance is relatively constant with temperature, Equation A-8 also can be used to evaluate total emittance at different temperatures.

A.2 SPECTRAL REFLECTANCE

Spectral reflectance is measured using most of the same equipment as spectral emittance, with the addition of an 8 inch diameter integrating sphere. As shown in Figure 1, a blackbody radiation source is used to illuminate the entrance slit of the monochrometer. The wavelength separated light passes through the monochrometer exit slit and is filtered to eliminate second order diffraction from the gratings. A zinc selenide lens collects and focuses the light at the sample port of the monochrometer. A shutter is located between the lens and the entrance port of the integrating sphere.

Data Acquisition and Reduction

Data acquisition is conducted in the same manner as with spectral emittance. The photo-detector voltage is measured as a function of wavelength over the wavelength range of about 0.6 to 14.4 μm. The photo-detector voltages are measured for an open hole (V_{hole}) representing a reflectance of 0.0, a gold coated target (V_{gold}) with a known reflectance, and for a test sample (V_{samp}) of unknown reflectance. The reflectance of the sample is determined as a linear interpolation between the measurements for the open hole ($\rho = 0.0$) and for the gold. That is:

$$\rho_{samp} = \rho_{hole} + \frac{\rho_{gold} - \rho_{hole}}{V_{gold} - \rho_{hole}} (V_{samp} - V_{hole}) \qquad \text{(A-9)}$$

where all variables are determined as a function of wavelength.

APPENDIX B

SPECTRAL ABSORBANCE AND EMITTANCE DATA

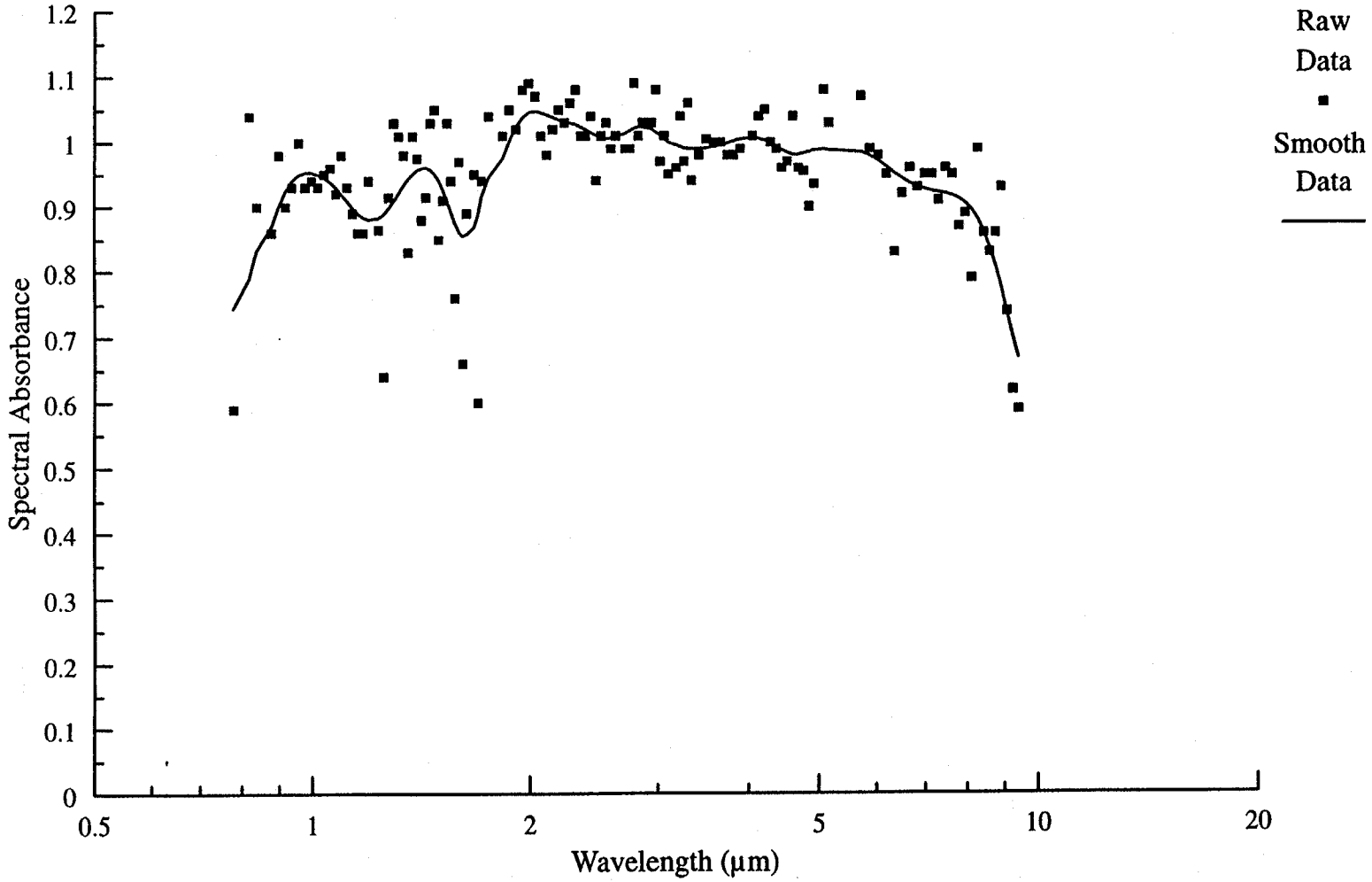

Figure B1. Spectral Absorbance of 67% Solids Black Liquor Liquid (Sample 1), Measured At 25 C

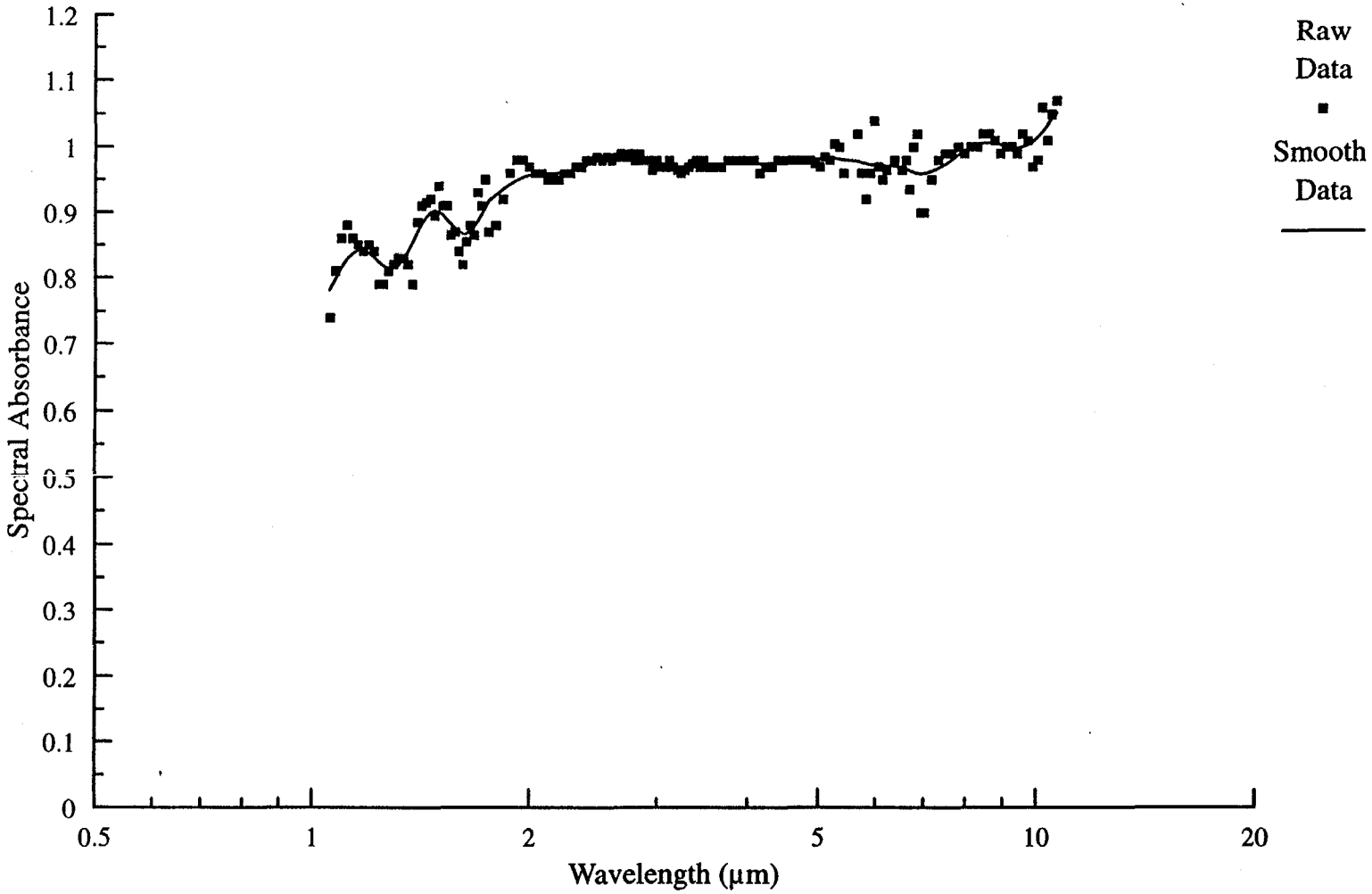

Figure B2. Spectral Absorbance of 67% Solids Black Liquor (Sample 2), Measured At 25 C

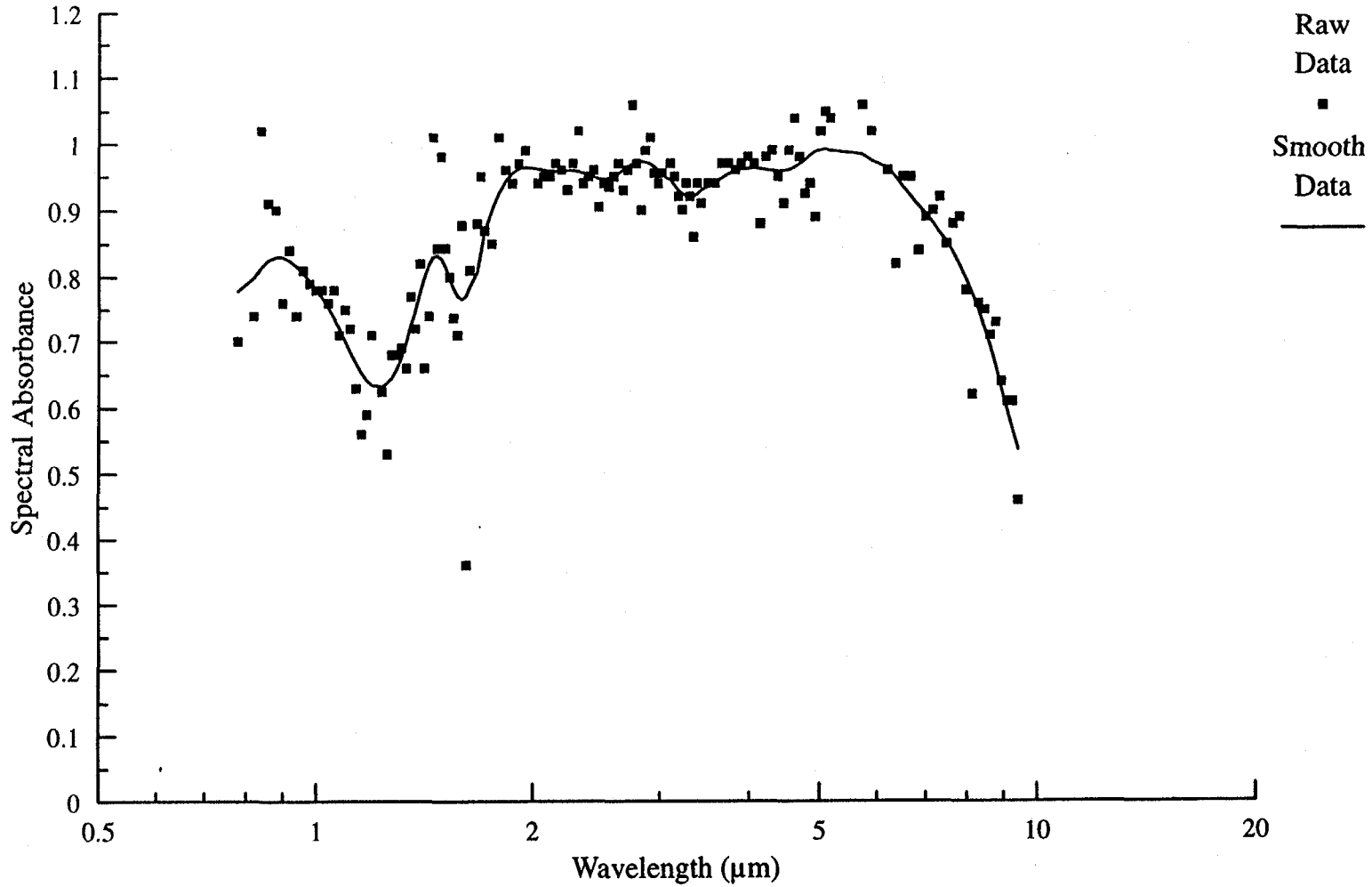

Figure B3. Spectral Absorbance of Black Liquor Dried Solids (Sample 1), Measured At 25 C

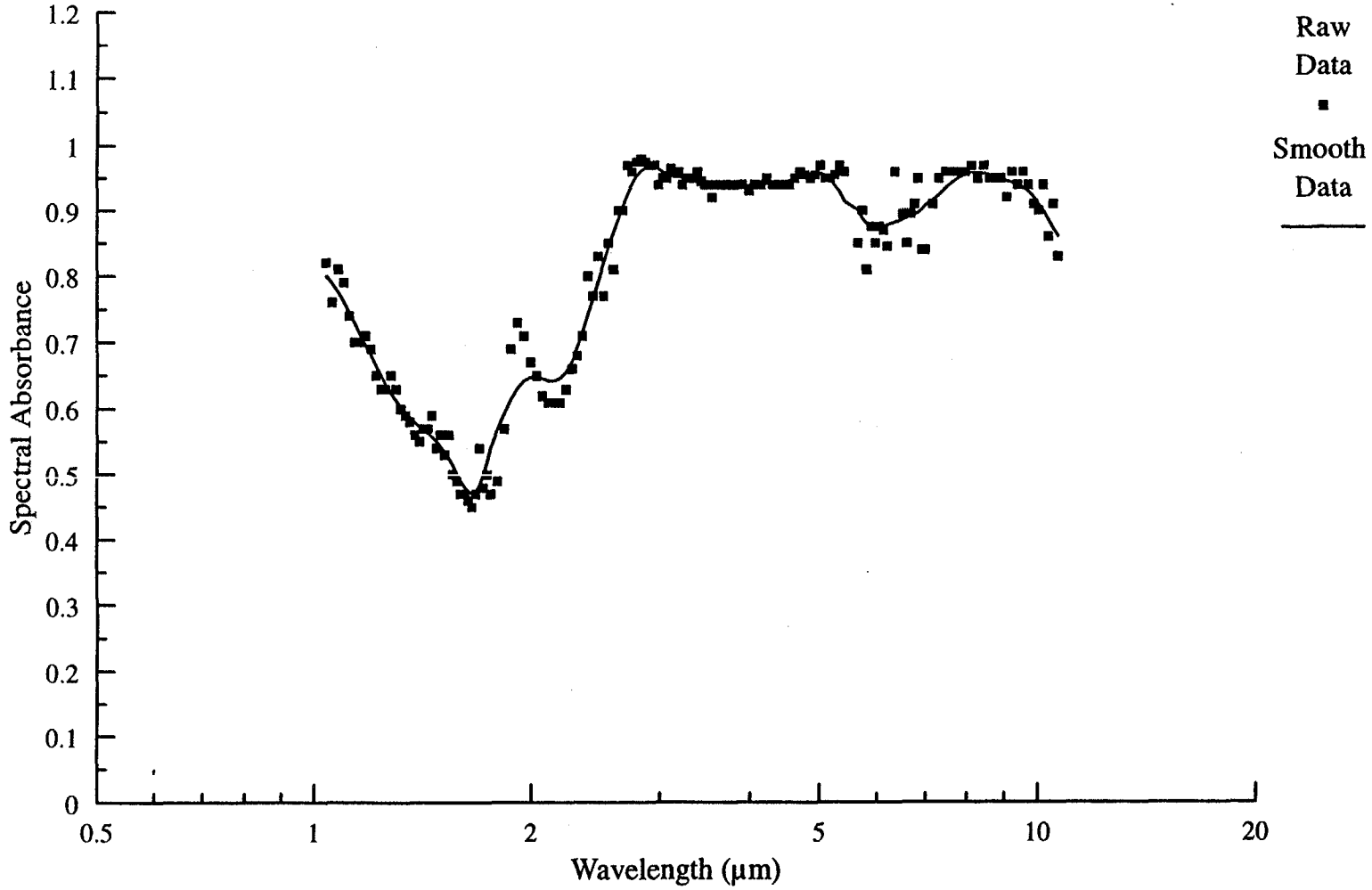

Figure B4. Spectral Absorbance of Dried Black Liquor Solids (Sample 2), Measured At 25 C

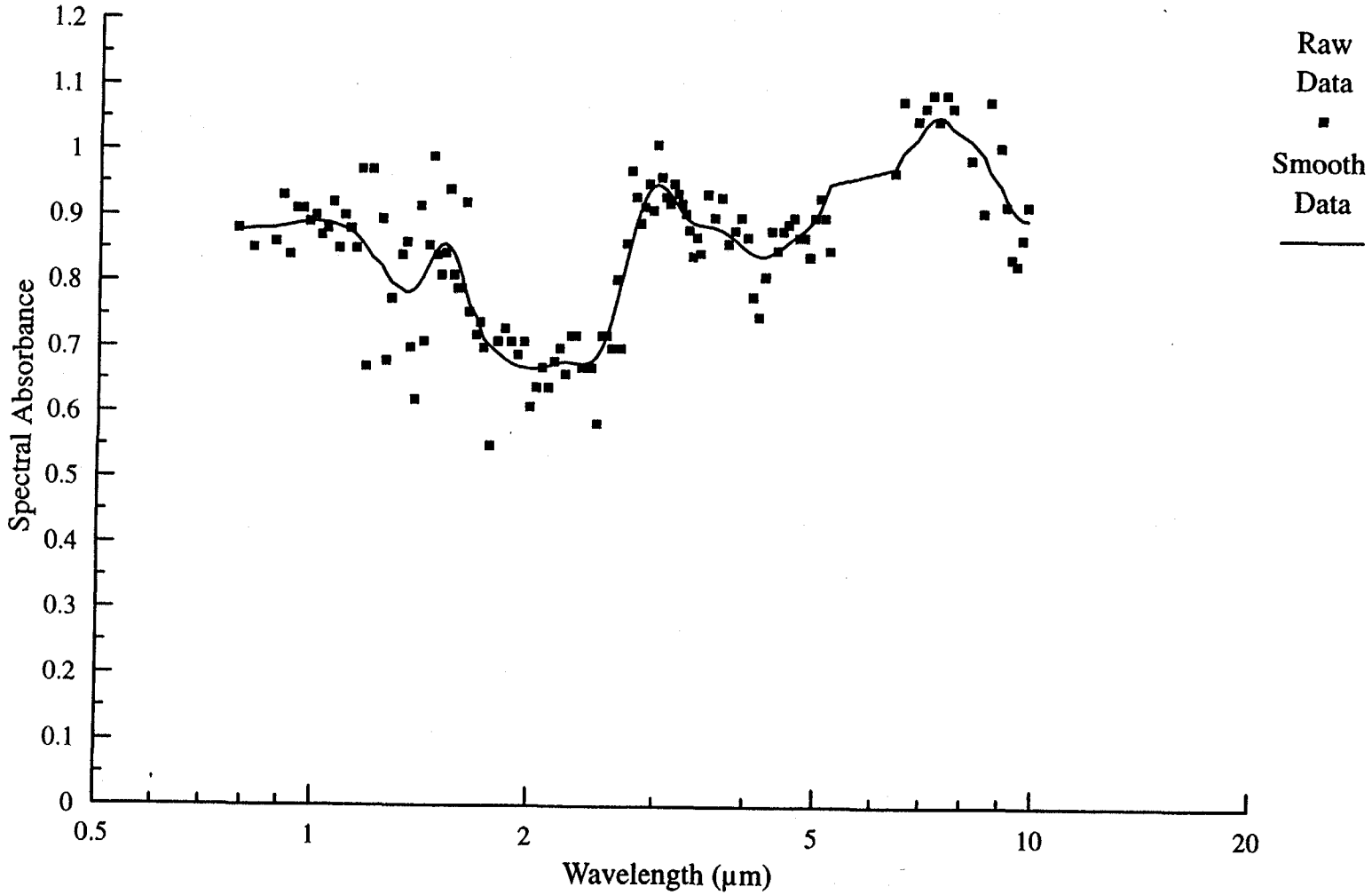

Figure B5. Spectral Absorbance of Black Liquor Char, Measured At 25 C

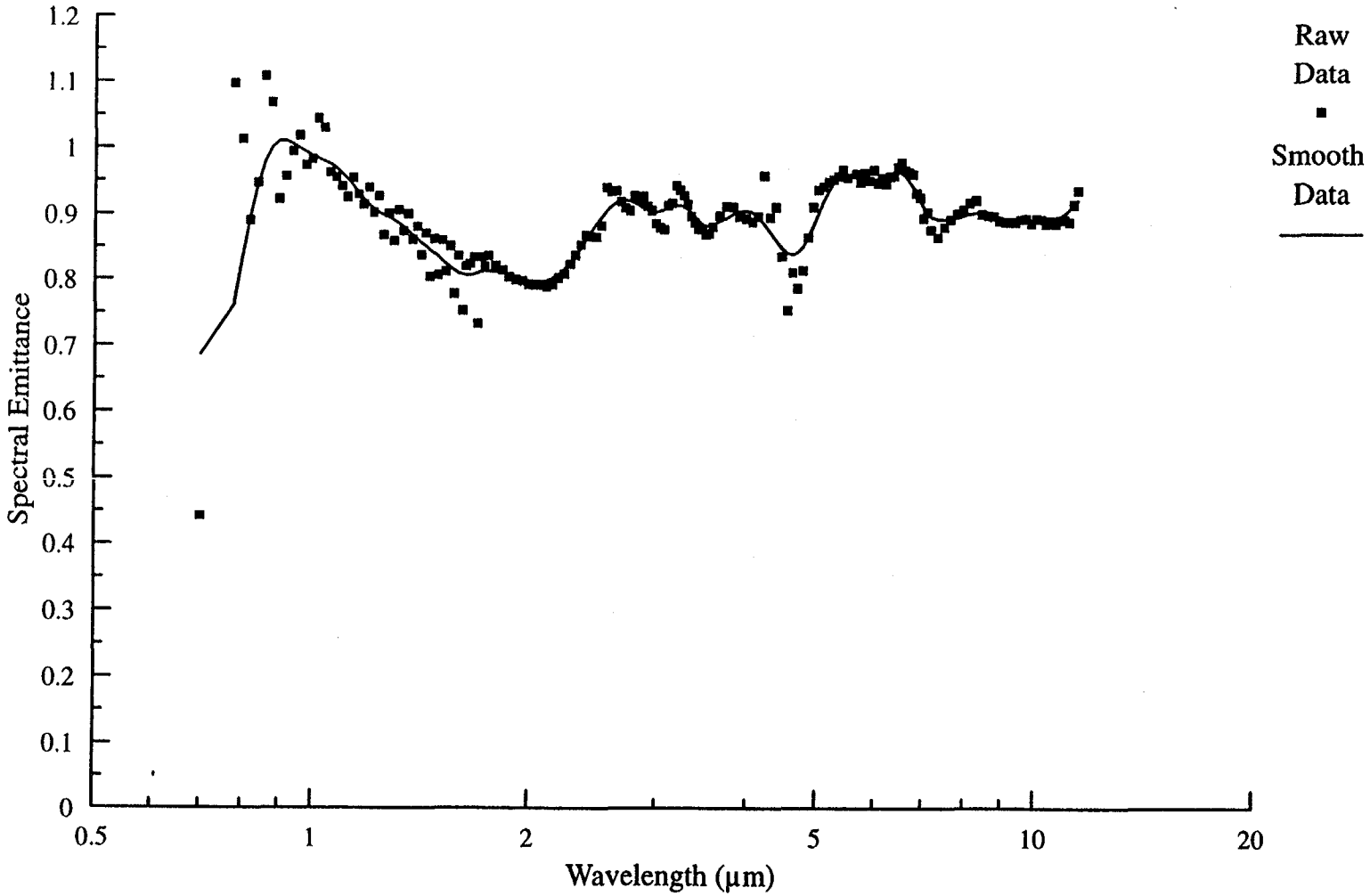

Figure B6. Spectral Emittance of Industrial Smelt Sample A, Measured At 847 C

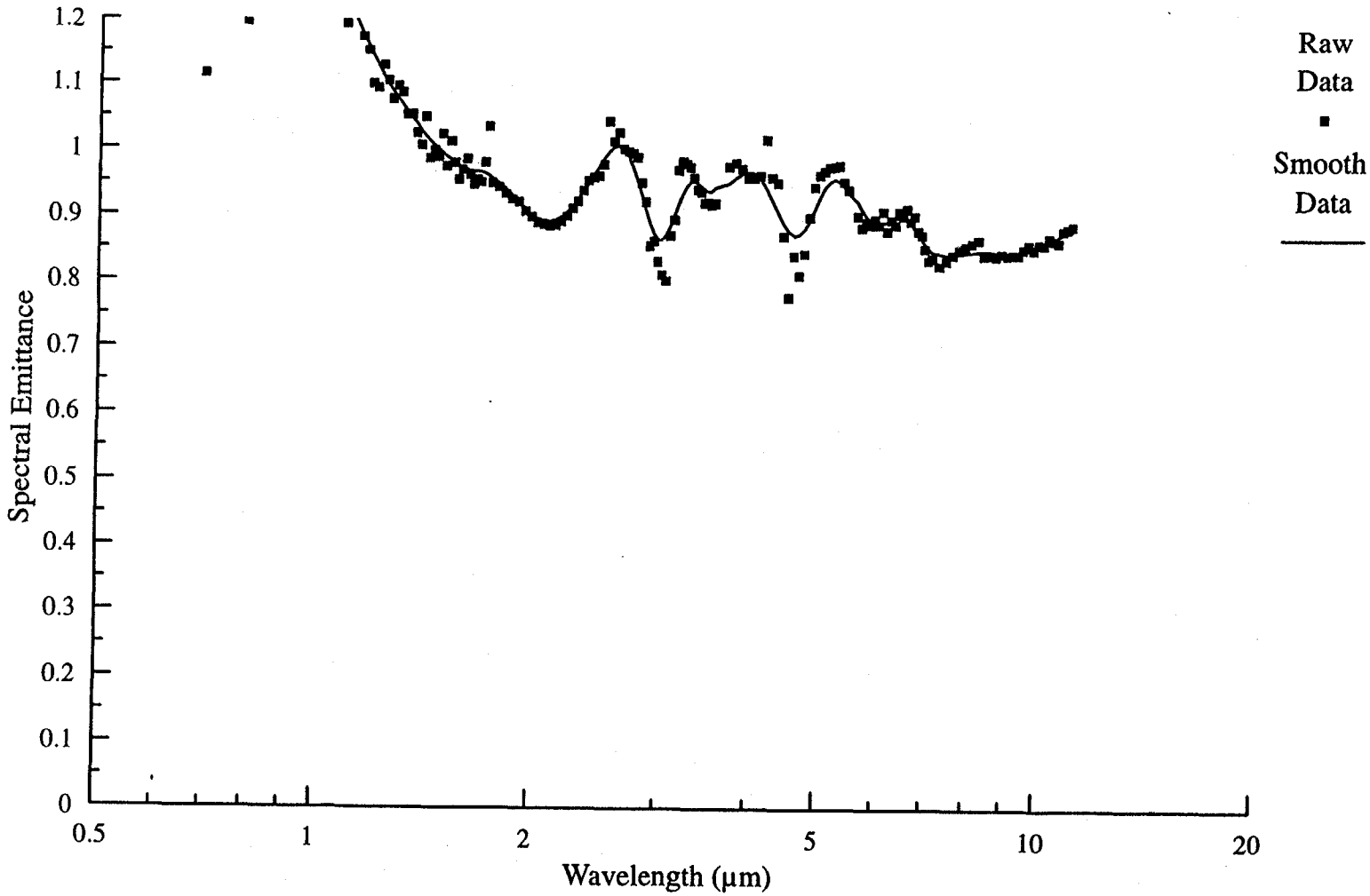

Figure B7. Spectral Emittance of Industrial Smelt Sample C, Measured At 848 C

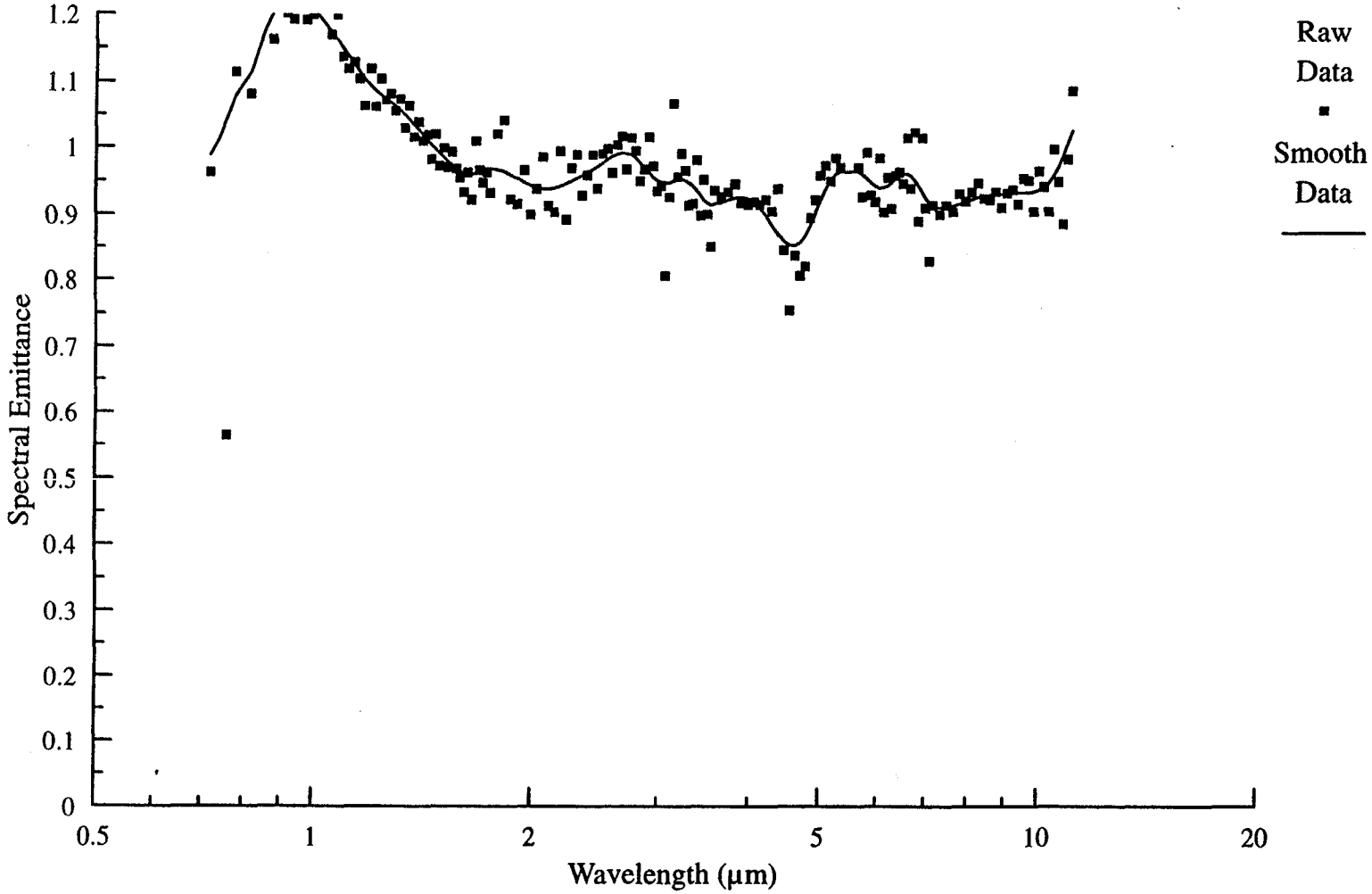

Figure B8. Spectral Emittance of Industrial Smelt Sample E, Measured At 813 C

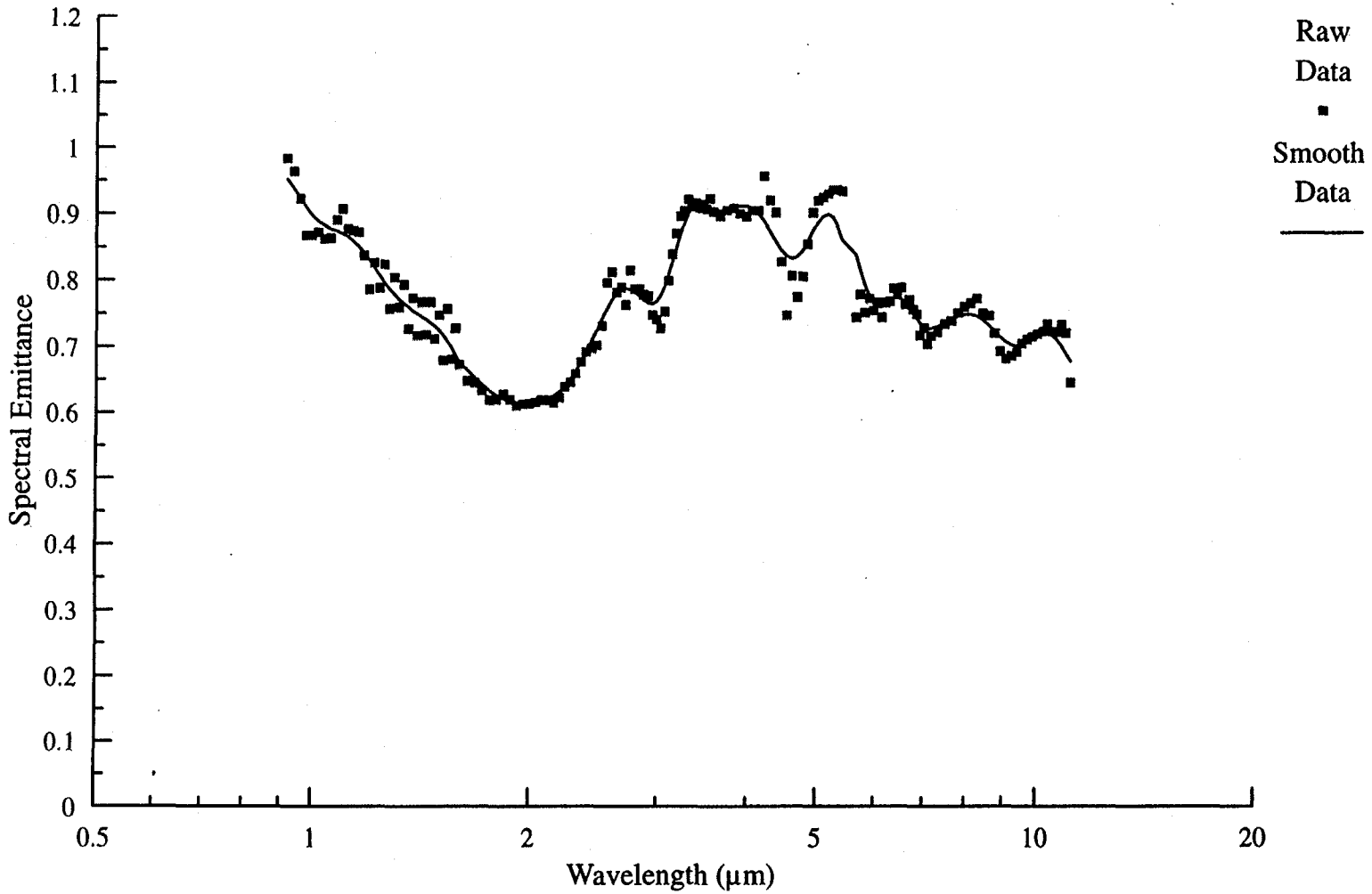

Figure B9. Spectral Emittance of Synthetic Oxidized Smelt Sample A, Measured At 931 C

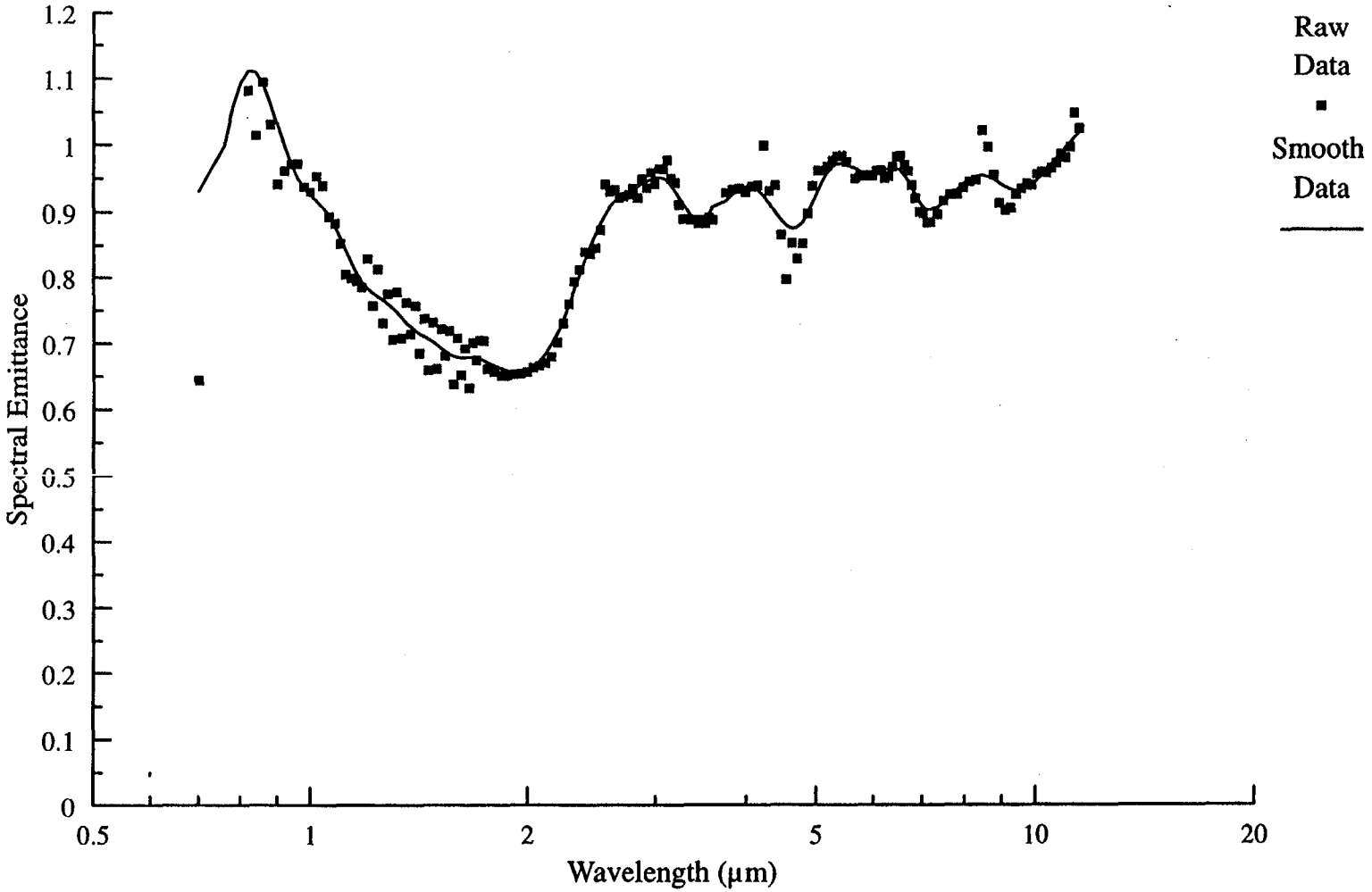

Figure B10. Spectral Emittance of Synthetic Oxidized Smelt Sample B, Measured At 871 C

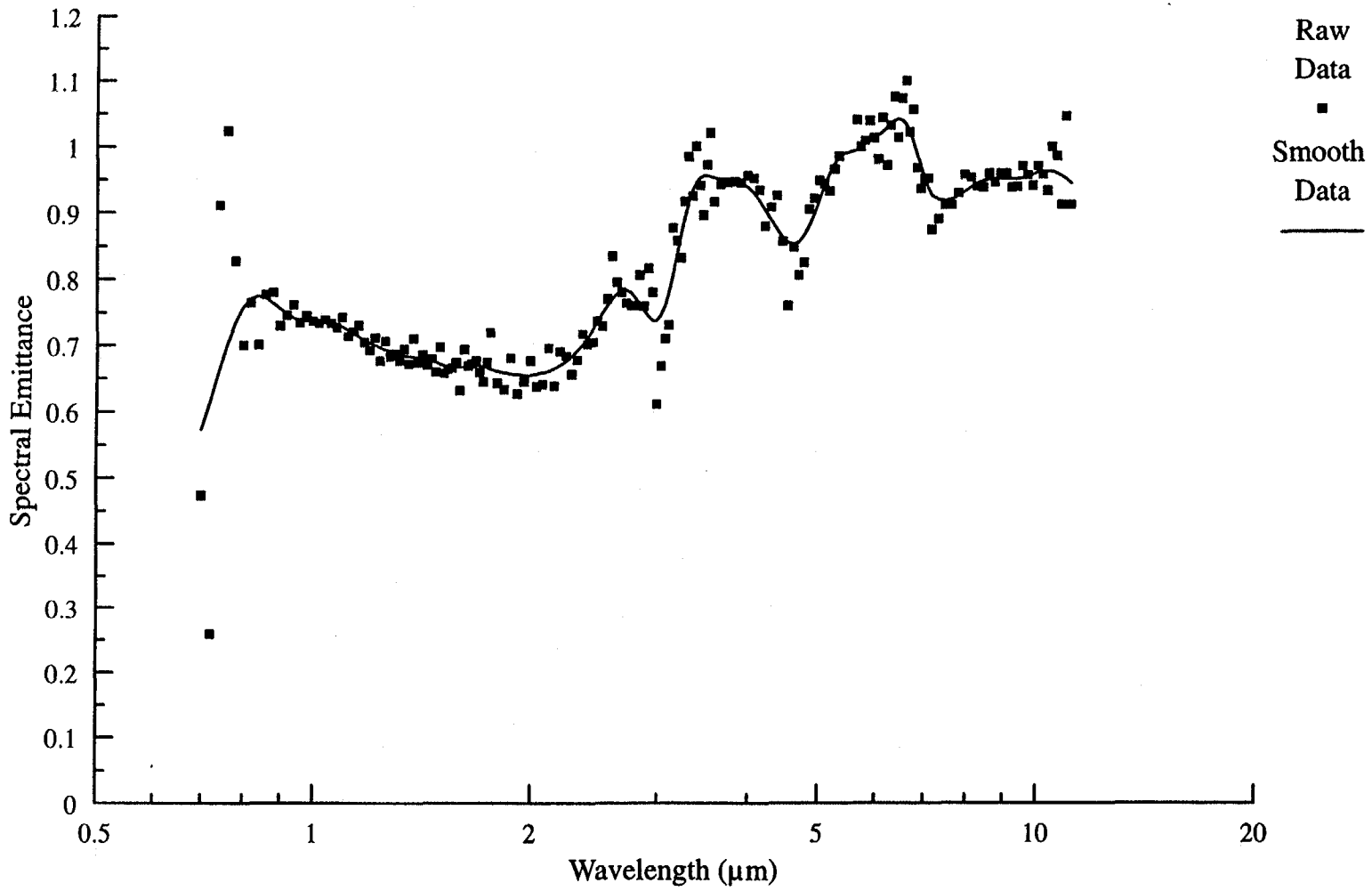

Figure B11. Spectral Emittance of Synthetic Reduced Smelt Sample B, Measured At 872 C

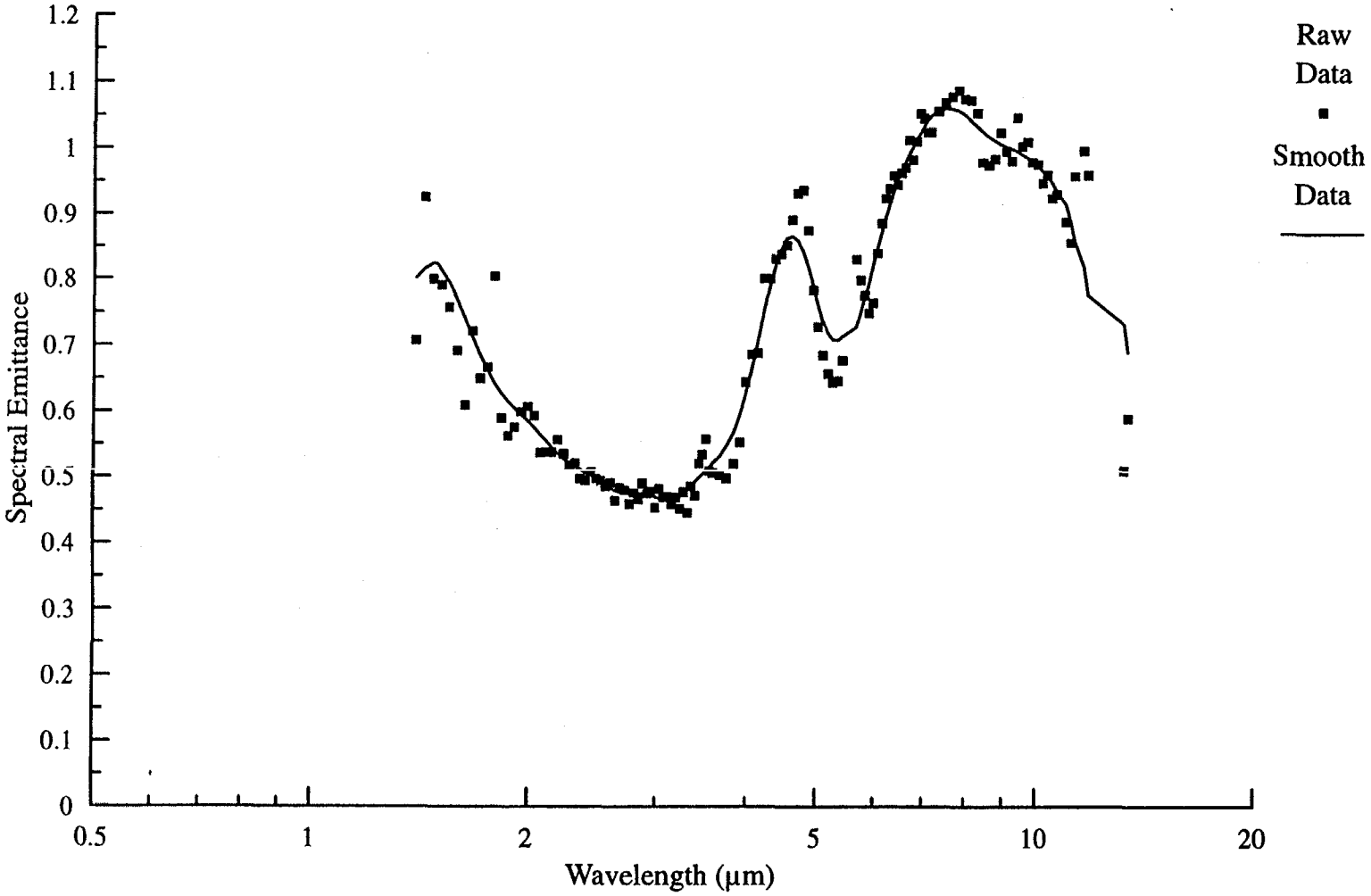

Figure B12. Spectral Emittance of Packed Economizer Dust, Measured At 466 C

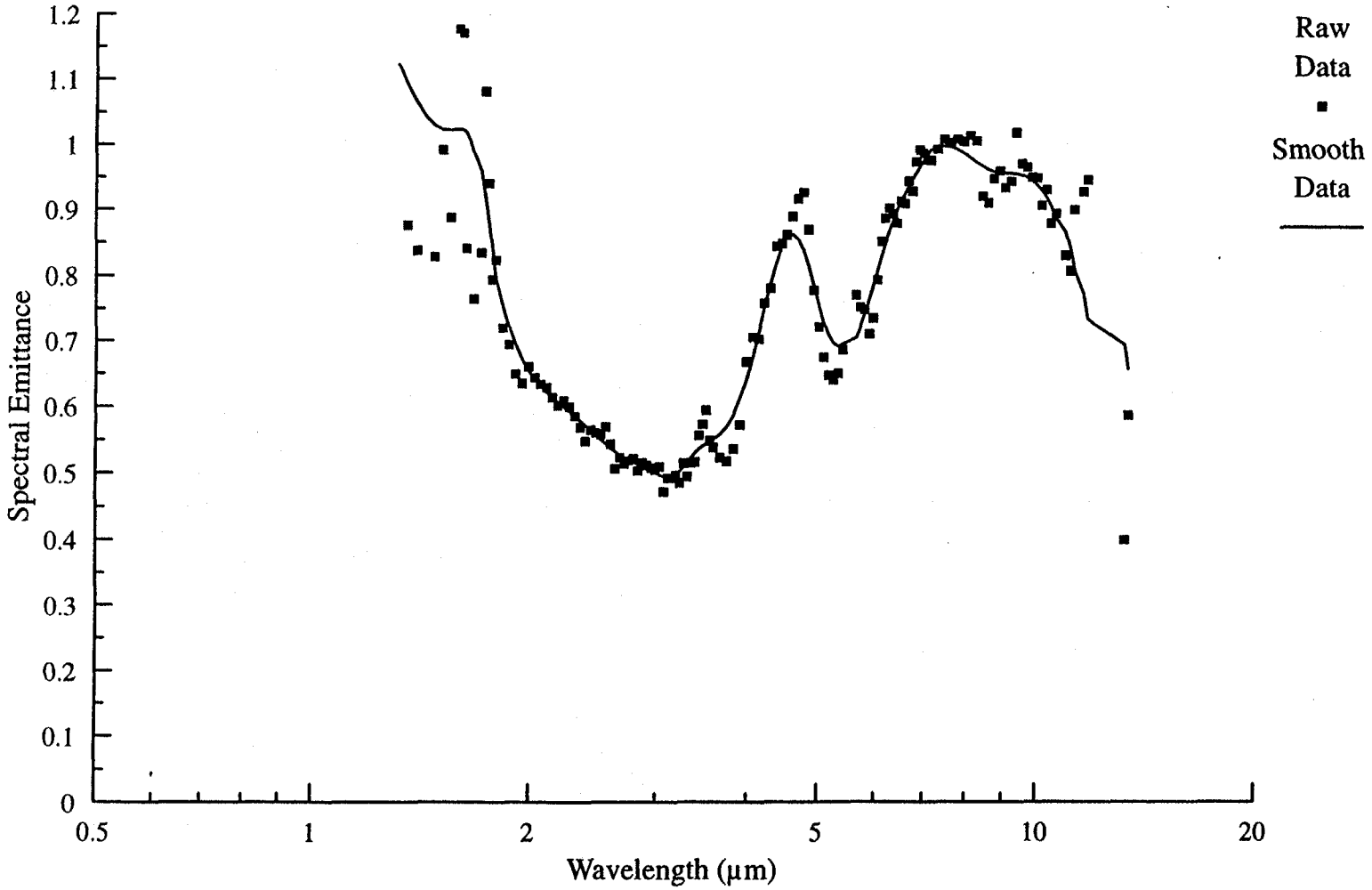

Figure B13. Spectral Emittance of Packed Economizer Dust, Measured At 468 C

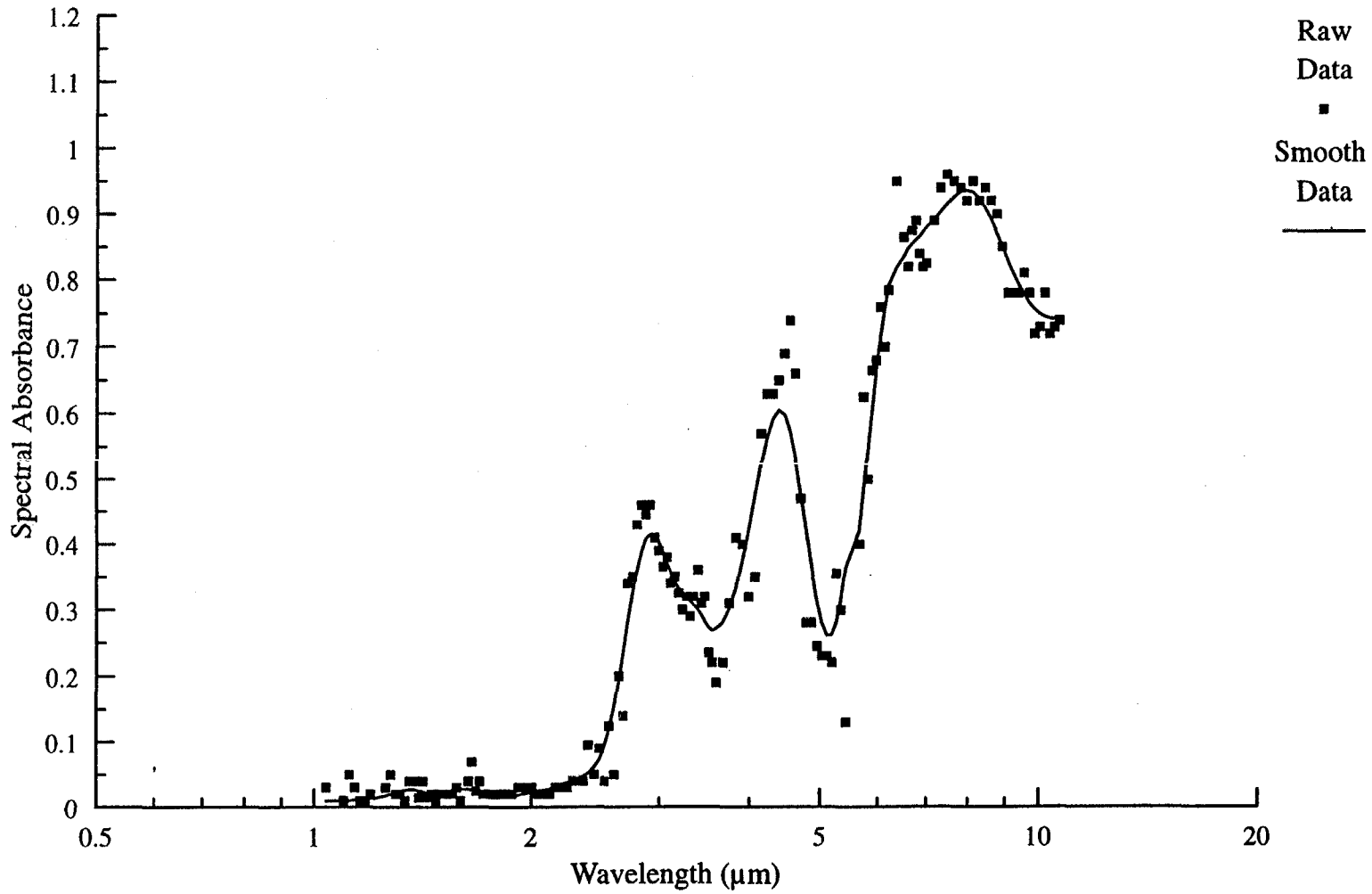

Figure B14. Spectral Absorbance of Fume Deposit, Measured At 25 C

RADIATIVE HEAT TRANSFER

DETERMINATION OF THE OPTICAL CONSTANTS OF ASH SAMPLES FROM KRAFT RECOVERY BOILERS[1]

by:

Artit Samretvanich, and W. J. Frederick

[1] The results included here were part of the M.S. thesis of Artit Samretvanich

Contents

INTRODUCTION

Heat transfer plays an important role in the operation and efficiency of combustion systems such as recovery boilers. Thermal radiation is the dominant mechanism of heat transfer in the combustion zones of these boilers. The radiative properties of the fume and carry-over particles transported by the gases determine how they absorb, transmit, reflect, and scatter radiant energy. They are critical properties in modeling them. Unfortunately, no data was available in the literature, prior to this study, on these properties and how they vary with particle composition. Knowledge of the radiative properties of carryover and fume particles is needed to improve the value and utility of detailed computational models of kraft recovery boilers.

Fume particles, the sub-micron aerosol particles formed during black liquor combustion, have an enormous potential to absorb, reflect, and scatter radiation because of their high total surface area. One of the goals of this study was to determine a fundamental property of fume particles, the complex index of refraction, from which the thermal radiative properties are obtained. The other goal was to determine to what extent the complex index of refraction varied with fume particle composition. In the work reported here, the optical constants were determined for ash samples collected from the electrostatic precipitators of kraft recovery boilers and their pure inorganic component alkali salts.

OBJECTIVES

The overall objective of this study was to obtain the optical constants of precipitator catch samples from kraft recovery boilers, and the constants for their pure inorganic components. The specific objectives were:

1. to determine the real and imaginary parts of the refractive index of the precipitator catch particles for wave numbers covering the range of importance for radiative heat transfer (500 cm^{-1}-5000 cm^{-1}),

2. to determine the effects of composition of the precipitator particles and obtain new reference data for the optical constants for pure inorganic salts, and

3. to relate the measured results to absorption and scattering mechanisms in kraft recovery boilers.

LITERATURE REVIEW

Introduction

There are many several ways for measuring the complex refractive index of a material. The suitable technique for a particular material depends on several factors such as the wavelength range measurement, the type of material being used and availability and quality of the optical element at the wavelength range.

Generally, no one technique is suitable for the entire wavelength range. A combination of the two or more techniques usually has to be used.

Technique of Measuring the Real and Imaginary Part of the Refractive Index

In 1970 and 1975, Ashkin[1] and Grams[2], respectively, use the light scattering technique for determination of size distributions and optical constants of aerosol materials. Particles were kept dispersed in a focal volume by making them flow in a gas stream. The optical constants were estimated by measuring at least two angle of angular scattered intensities and employing Mie theory. This method can be applied to many particle types. However, it is difficult to perform in both the equipment setting and calculation.

The study of Willis[3], was conducted by dispersing the particles in a flowing gas at room temperature and illuminated with a mercury lamp (λ=0.546 μm). The complex refractive index was computed by measuring the relative intensities of two linearly polarized components of the scattered light. The result was found to have an error an order of magnitude larger than it would be expected for a dielectic material at this wavelength.

Photoacoustic technique was a direct technique to measure absorption of light, Roesseler and Faxvag[4]. Particles in a focal volume are illuminated by light chopped at audio frequencies. Because of the absorption of the particles, a pressure oscillation occurred and was detected by microphone. Only absorbed light causes heating so absorption can be measured even in presence of scattering.

The measurements for acetylene smokes and diesel emissions have been reported using wavelengths of 0.5 and 10 μm. In principal, it should be possible to calculate the absorption index from the photoacoustic spectra. However, if the particles are weakly or moderately absorbing as is the case with fly ash particles, large light energies are requires. Moreover, for in-situ measurements on particles where volatile matter is lost during heating of the particles, this may be cause a larger error.

The KBr pellet transmittance technique was used for measuring the imaginary part of the refractive index for fly ash at wavelength 3 μm to 40 μm by Volz[5]

This technique consists of dispersing a small amount of powder in KBr powder, compressing the mixture under vacuum to form a thin disc, and then measuring the spectral transmittance of the disc. The imaginary part of the refractive index, *k*, was determined from the relation shown below.

$$T = \exp\left(- \frac{4\pi k M_s}{\lambda \rho_s A_p} \right)$$

Here, T is the measured transmittance, λ is the wavelength, M_s is the mass of fly ash added to the KBr powder, ρ_s is the density of the fly ash, and A_p is the area of the pellet.

This expression is not applicable if the particles have sizes comparable to or larger than the wavelength because they may then scatter and absorb at the same time.

The combustion method of emission and transmission (E/T) spectroscopy performed using a Fourier Transform infrared (FT-IR) spectrometer was employed by Solomon[6] et al., 1986. In this paper, a new method for the online chemical characterization of gas-suspended particulate and liquid droplet stream was reported. Emission and transmission measurements were conducted in a specially designed cell surrounding the intersection of the FT-IR beam with the sample stream.

The transmission and emission were measured from the samples, and a quantity referred to as normalized radiance or emission/transmission (E/T) spectra was calculated. The material optical constants were determined by using Mie theory. A quantitative spectrum of a finely dispersed coal in a pressed KBr pellet, a non-quantitative photoacoustic spectrum for fine particles suspended on a thin membrane and E/T "absorbance" spectrum was compared by using the same coal.

From the comparison, it was found that photoacoustic spectroscopy (PAS) can be performed without sample preparation, but spectra are typically non-quantitative and often distorted by saturation effects. The KBr pellet spectrum also has distortion of the band due to the Christiansen effect. This effect caused by variation in the real part of the index of refraction near the absorption band, which affects the scattering contribution. This method is applicable when the scattering and absorption effects can be separated.

The E/T absorbance spectrum method provides the most quantitative absorbance spectrum (for samples of known particle size) and can be obtained with the least sample preparation. Moreover, the E/T absorbance spectrum is free from scattering and band distributions. However, the signal-to-noise ratios problems still have an effect the absorption spectrum that may cause the significant error for the optical constants.

Goodwin[7] et al., 1989, performed an experiment study of the infrared optical constants of coal slag. The real and imaginary parts of the refractive index were determined from transmittance and reflectance measurements, from the visible range to 13 μm. Measurements were made with thin, polished glassy slag wafers at room temperature. The optical constants were determined directly from the appropriate relations from electromagnetic theory for the trasmittance/reflectance of a plane-parallel slab incorporating the multiple oscillator model.

The error resulting from the transmittance measurement contributed to the uncertainty in the imaginary part of the refractive index, k, because of the logarithmic dependence of k on the measured transmittance. The error in k was generally dominated by the uncertainty in the wafer thickness. Furthermore, the experimental setup was difficult to make owing to the complicated equipment in measurement of both transmittance and reflectance.

Foster[8] et al., 1967, used a plane polarized light reflection technique to measure the real and absorption index of a series of carbon in the wavelength region 1 to 10 microns at room temperature. By considering a plane-polarized monochromatic beam reflected at non-normal incidence from the surface of an absorbing medium, a phase difference is introduced between the two components whose electric vectors lie parallel to and perpendicular to the plane of incidence.

The optical constants may be calculated from the appropriate Fresnel coefficients by considering on the phase angle and reflectivities. The result of the optical constants seemed to be limit by its range of useful application and showed quite large error. In addition, the experimental apparatus was complicated due largely to the many mirrors and optical accessories needed to be set the appropriate angle.

The infrared optical constants, n and k, of swelling and non-swelling coals, their respective char products, and limestone at room temperature obtained by a particle extinction technique using compressed KBr pellets have been studied by Brewster and Kunitomo.[9] They assumed spherical particles and used Mie theory for the particle extinction measurements in conjunction with normal specular reflectance measurements from polished specimens. Instead of using the Fresnel equation, experimental data for the extinction efficiency $\overline{Q}_{ext}(\hat{n}, x, N(r))$ of micron-sized particle suspensions

was used to infer the values of n and k according to Mie theory. In Mie theory, if the particle size and wavelength are known, $\overline{Q}_{ext}$ will be a function of only n and k. Therefore, measurement of one more independent quantity that is also a function of n and k should allow for their implicit solution.

As the second independent quantity, normal specular reflectance (R_N) was measured with an infrared prism-type spectrophotometer using polished specimens of coal and limestone. The two equations must be solved simultaneously to get n and k.

$$R_N = \frac{\left[(n-1)^2 + k^2\right]}{\left[(n+1)^2 + k^2\right]}$$

$$\overline{Q}_{ext}\left(\frac{\hat{n}}{n_w}, \lambda, \alpha, \beta\right) = \frac{\int_0^\infty \pi r^2 Q_{ext}\left(\frac{\hat{n}}{n_w}, x\right) N(r)dr}{\int_0^\infty \pi r^2 N(r)dr}$$

where R_n = normal specular reflectance

n = real part of refractive index

k = imaginary part of refractive index

$\overline{Q}_{ext}$ = effective polydispersion extinction coefficient

r = particle radius

n_w = refractive index of KBr

N(R) = particle size distribution function, number/volume.

X = particle size parameter, $\pi d/\lambda$

The values of the complex part of the refractive index for coal were found to be about an order of magnitude smaller than previously reported values determined by only Fresnel reflectance techniques.

Owing to the extreme difficulty in satisfying the stringent requirements for experimental determination of n and k, even this technique is subject to inaccuracy. The assumption of spherical particles, polydispersity effects, difficulty in measuring particle density, etc., all introduce error in the analysis. For char specimen, the specular reflectance was not feasible and therefore a dispersion equation curve fitting technique was applied to the extinction data to get n and k.

There is some doubt regarding the assumption of Brewster and Kunitomo[9], that particles remain in particle form without agglomeration even after mixing with KBr and particles may remain as individual particles only if used in a small number.

In 1993, Im and Ahluwalia[10] later analyzed the Brewster and Kunitomo data on char optical constants. They found some discrepancy while using Mie theory and the dispersion equation. They suggested that an extinction measurement alone should be sufficient for deriving optical constants and also recommended a need to distinguish between absorption and scattering contributions to extinction. Moreover, In Kunitomo's data the extinction was accounted on the forward scattering that leads to a high value of the imaginary part of the refractive index (the forward scattering should be separated from the absorption).

Solomon[6] et al. and Markham et al., [11,12] have further studied the optical constants by using a modified version of Kunitomo's particle extinction technique to find the refractive index of char and coal. Pellets were prepared using 1-2 mg of sample in 150-300 mg of Kbr and CsI. They measured the particle size using SEM photographs and assumed that some size distribution is preserved inside the pellet after mixing. Transmission spectra were obtained for both pellets and a combination of Mie theory and Kramer-Kronigs analysis was used to fit both the spectra to get values of real and absorption index.

In the experiment, they accounted for scattering in the forward direction within the acceptance angle of the detector. They obtained values of n and k of the same order as those of Brewster and Kunitomo. Solomon et al. also found that the forward-scattered radiation may effect the transmittance significantly depending on both the wavelength and size distribution.

In 1973, Peterson and Knight[13] had developed an alternative procedure of the Kramer-Kronigs relation in order to get either absorption index or real index by using the consequences of causality and analyticity combined with a time-domain method. The real and imaginary parts can be related to each other by observing that physical system can respond to a physical system's impulse response, see the detail in chapter 3, and the Fourier transforms of these response functions.

This new procedure shows large gains of computational efficiency over the classical Kramer-Kronigs approach.

Measurement of Optical Constants for Fly ash, Char and Coal

Measurements of the optical constants of fly ash have been reported in several studies. There are several techniques used to determine the optical constant of fly ash, char and coal. However, the lack of available data is still a the problem.

Willis[3], as discussed in the last section, studied the optical constants of ash dispersed in a flowing gas at room temperature and illuminated with a mercury lamp. The reported values for the imaginary part of the refractive index were a order of magnitude higher than would be expected for a dielectric material at this wavelength.

In 1981, Gupta and Wall[14] found Willis's data to be meaningless because the Fresnel relations which he used in obtaining his values are validity only for uniform plane media.

The imaginary part of the refractive index for fly ash of unspecified composition for the range between 0.5 μm and 40 μm was examined by Volz[5]. Volz used the KBr pellet transmittance technique consisting of dispersing a small amount of powder in KBr powder, compressing into a disc, and then measuring the spectra's transmittance of the disc. The values of k ranged from 0.0048 at 0.5 μm to nearly 1.0 at 40μm. It was found later that the constraints on the equations used in Volz' analysis were unsatisfied, and that had led to a significant error in measured value of k. At wavelengths where k was small, the value calculated from the Volz equation was too large. This was due mainly to the neglect of scattering in Volz's equation. At wavelengths where k was of the order of one, the predicted k value was

too small, owing to the non-linearity of the relationship between the extinction coefficient of the particles and k.

Low[15] et al. , and Gupta and Wall[14] have presented results for the imaginary part of the optical constant for fly ash measured in-situ at the furnace exit of a pulverized-coal utility boiler. The values of k were inferred from the measured emission. They ranged from 0.01to 0.02. However, the later measurements of Gupta and Wall using an improved of the radiometric probe resulted in value of k approximately a factor of 2 lower for the same coals. Gupta and Wall showed that both their results were biased by the presence of up to 10% residual carbon at the furnace exit.

Low et al., assumed that the carbon was primarily in the form of large unburned char particles (having small total surface area) so that the contribution of the carbon to the measured absorption coefficient could be neglected. Gupta and Wall checked this assumption by making the experiments on sample ash, before and after burning off the remaining carbon, in which the KBr technique was used. These measurements showed that burning off the residual carbon in the ash resulted in a factor of 2 decrease in k. This resulted in the value of k reported by Low et al. and Gupta and Wall being high due to the presence of unburned carbon in the furnace exit. The scattering may also have affected the value of k.

The results of the two studies (Willis[3] and Volz[5]) were shown by later investigators to be incorrect owing to the method employed. The in-situ measurements of Low et al. and Gupta and Wall were also biased by the presence of the residual carbon.

Experiment studies of the infrared optical constants of coal slag are presented in 1989 by Goodwin[7] et al. The real and imaginary parts of the refractive index were determined from transmittance measurements on thin polished glassy slag wafers at room temperature from visible wavelengths to 13 microns. Goodwin presented a mixture rule for the glassy ash samples by relating the refractive index to chemical composition. The rule for determining n was based on the mass fraction of the mineral constituents SiO_2, Al_2O_3, CaO, MgO and Fe_2O_3.

From these experiments, the imaginary part of refractive index, k, depends primarily on the iron, silica, and hydroxide content of the coal slag. Iron is the dominant absorber for $\lambda<4\mu m$. A correlation was developed for the effects of Fe on k in this wavelength range, accounting for the dependence on both total Fe content and its oxidation state. The presence of hydroxide in the slag results in two absorption bands at 2.8 microns and 7 microns.

The value of k in the longer wavelength region was controlled by the silica content of the slag. The absorption in the 5-8 μm regions compared well with that of fused silica and appeared to be caused by combination and overtone vibrational absorption. In 8-13 μm region, the optical constants were determined by the fundamental vibrational resonance of Si-O-Si and Si-O. A mixture rule was developed to predicted the real part n of the refractive index for the wavelength range 1-8 μm in terms of the oxide components SiO_2, Al_2O_3, CaO, MgO, TiO_2 and Fe_2O_3.

Moreover, Goodwin also found that the temperature had an effect on the absorption index in the Fe absorption region from 1 μm to 8 μm. k increases with increasing temperature. Nonetheless, for the reduced slag (less amount of iron content), the value of k was very slightly affected by increasing temperature (up to 1200 ^{0}K).

Brewster and Kunitomo[9], as mentioned in the preceding section, employed a transmission technique using small coal particles dispersed in KBr, and made set of measurement involving normal specular reflectance on polished specimens of coal. The result complex indexes were an order of

magnitude lower than those of Foster and Howarth. Absorption index showed considerable wavelength dependence. A strong absorption band near 9 μm wavelength that increased with decreasing coal rank was observed. The trend for decreasing of the absorption index was explained by the fact that for higher rank coals, more of the carbon was presented as "fixed-carbon" and less as aliphatic and aromatic hydrocarbon molecules where vibration appear to be the primary source of absorption in the infrared region.

Solomon[6],1986, used the extension of the Brewster and Kunitomo[9]to examined further study of the optical constant and emission properties of three different coals. He found that the value of the refractive index obtained by using Mie theory and Kromer-Kronigs relation were quite similar to that of emission and transmission (E/T) method but more comfortable and easier to employ.

However, data on the optical properties of fume particles from Kraft recovery boilers have not been ever reported. In this study, experiments were conducted to investigate the radiative properties of fume particles by using the KBR extinction technique along with a scattering model based on Mie theory and a relationship between the real and imaginary part of refractive index, the Kramers-Kronig relationship.

Conclusions and implication for the present study

1. Each measurement technique has its own advantages and drawbacks. The technique best suited to a particular material depends on several factors: the type of material being tested, expected values for the optical constants, the wavelength range, and the availability and quality of the optical elements.

2. The accurate determination of optical constants of a material is a difficult task. It requires not only accurate instruments but also well characterized samples.

3. For coal char and fly ash, the real and absorption index are relatively insensitive to instrumental techniques. The carbon content appeared to be the most significant determining effect. The higher the carbon content, the higher are the real and absorption index. The amount of iron and silica content and the oxidation state of Si also have an effect on the absorption index.

4. A technique based on extinction measurements with particles suspended in KBr pellets, and employing Mie theory to interpret the data, should provide a simple and more straightforward method of obtaining accurate optical constant data.

Based on this analysis, the method of Solomon[6] and Kunitomo[9] were applied in this study to determine the optical constants of the ash samples taken from different recovery boilers in pulp and paper industries.

The KBr extinction technique (KBr pellet method) was used to obtain the absorption spectra of the materials, and Mie theory was employed with the alternative Kramer-Kronigs relation to calculate the extinction coefficient, and compare predicted and experimental absorption data, and determine the accurate optical constants, n and k, respectively. Details of the calculation and procedure are discussed in a subsequent section of this appendix.

THEORY

In this section, the optical constants are defined by the electromagnetic theory and related to the experimental quantities. The theory of electromagnetic is discussed in the second section of the chapter

after the importance of thermal radiation. The radiative properties of the particles are outlined in the following section. Finally, the techniques of measuring real and absorption index are presented.

The Optical Constants

Electromagnetic theory

The treatment of absorption and scattering of light by small particles is related by the Maxwell's equations that describe the important of the thermal radiation with a macroscopic approach. Moreover, they govern the propagation of electromagnetic radiation both in vacuum and in real matter.

Maxwell's equations can be written in the complex form

$$\nabla \cdot D = \rho_F \qquad \text{------ (1)}$$

$$\nabla \times E + \frac{\partial B}{\partial t} = 0 \qquad \text{------ (2)}$$

$$\nabla \cdot B = 0 \qquad \text{------ (3)}$$

$$\nabla \times H = J_F + \frac{\partial D}{\partial t} \qquad \text{------ (4)}$$

where the electric displacement D and magnetic field H are defined by

$$D = \varepsilon_0 E + P \qquad \text{------ (5)}$$

$$H = \frac{B}{\mu_0} - M \qquad \text{------- (6)}$$

and E = the electric field

B = the magnetic field

P = the electric polarization

M = the magnetization

μ_0 = permeability of free space

ρ_F = charge density

J_F = free charges

These four equations are insufficient in themselves to describe all the properties included in the electromagnetic theory. The additional constitutive relations are also needed:

$$J_F = \sigma E \qquad \text{----- (7)}$$

$$B = \mu H \qquad \text{----- (8)}$$

$$P = \varepsilon_0 \chi E \qquad \text{---- (9)}$$

where σ is conductivity, μ is permeability and χ is electric susceptibility.

If the electromagnetic fields are harmonic in time, then Maxwell's equation can be written in simpler form:

$$\nabla \cdot (\varepsilon E_c) = 0 \qquad \text{------ (10)}$$

$$\nabla \times E_c = i\omega\mu H \qquad \text{------ (11)}$$

$$\nabla \cdot (\mu H_c) = 0 \qquad \text{------ (12)}$$

$$\nabla \times H_c = -i\omega\varepsilon E_c \qquad \text{------ (13)}$$

where ε is the complex permittivity of medium and μ is the complex permeability.

The two coefficients $\varepsilon(\omega)$ and $\mu(\omega)$ completely characterize the electromagnetic properties of the medium at frequency ω. The permittivity can also be related to the susceptibility $\chi(\omega)$ which characterizes the effects of band charges and the conductivity $\sigma(\omega)$, which characterizes the effects of free charge

$$\varepsilon(\omega) = \varepsilon_0 [\, 1 + \chi(\omega) \,] + i\frac{\partial(\omega)}{\omega} \qquad \text{----- (14)}$$

These phenomenological coefficients (σ,μ,χ and ε) are described the properties of the electromagnetic in each medium. For an example in the free space, the permittivity $\varepsilon(\omega)$ is solely specified the electromagnetic properties because $\mu(\omega) = \mu_0$ (constant).

Complete information on the interaction of radiative properties is contained in the function of $\varepsilon(\omega)$ and $\mu(\omega)$. The measurable quantities are determined by solving the macroscopic equation of Maxwell's with known $\varepsilon(\omega)$ and appropriate boundary conditions. However, there are many classes of materials for which these assumptions are not valid. Hence, Maxwell's equations are restricted to materials that are uniform, isotropic and linear with respect to their radiative properties.

In an infinite medium with uniform properties, the general solutions of Maxwell's equations are transverse plane waves, given by

$$E_c = E_0 \exp(ikx - i\omega t) \qquad \text{----- (15)}$$

$$H_c = H_0 \exp(ikx - i\omega t) \qquad \text{----- (16)}$$

where E_0 and H_0 are constant vectors and wave vector k is defined as

$$k = k' + ik'' \qquad \text{----- (17)}$$

By substitution, $k = k' + ik''$ in (15) and (16)

$$E_c = E_0(-k''\cdot x)\exp(ik'x - i\omega t) \qquad \text{----- (18)}$$

$$H_c = H_0(-k''\cdot x)\exp(ik'x - i\omega t) \qquad \text{----- (19)}$$

$E_0(-k''\cdot x)$ and $H_0(-k''\cdot x)$ are the amplitudes of the electric and magnetic waves, and $\phi = k'x - \omega t$ is the phase of the waves.

From the condition of transversality, k is perpendicular to E_0 and H_0, so,

$$k\cdot E_0 = k\cdot H_0 = E_0\cdot H_0 = 0 \text{ and obtain } \quad k\cdot k = \omega^2\varepsilon\mu \qquad \text{---- (20)}$$

The wave vector of a homogeneous wave may be written $k = (k' + ik'')\hat{e}$, where k' and k'' are nonnegative and $\hat{e}$ is a real unit vector in the direction of propagation.

So, $k = k' + ik'' = \omega N/C_0$, where C_0 is the speed of light in vacuum and the complex refractive index N is

$$N = C_0\sqrt{\varepsilon\mu} = \sqrt{\frac{\varepsilon\mu}{\varepsilon_0\mu_0}} \qquad \text{----- (21)}$$

$$N = n + ik \equiv C_0\sqrt{\varepsilon\mu} \qquad \text{----- (22)}$$

The dispersion relation ($k\cdot k = \omega^2\varepsilon\mu$) may be written in terms of the complex refractive index as

$$k\cdot k = (\omega N/C_0)^2 \qquad \text{----- (23)}$$

If the refractive index is real (k=0) then k is real and the electric and magnetic fields in the medium are plane waves with constant amplitude. Hence, equating equations (18) and (23), and expressing them in terms of the wave number ($\frac{\omega}{C_0} = \frac{2\pi}{\lambda}$), one gets, for a homogeneous wave in dielectric media (zero conductivity):

$$E(x,t) = E_0 \exp(i2\pi nx/\lambda - i\omega t) \qquad \text{----- (24)}$$

and for a homogeneous wave in an finite conductivity media:

$$E(x,t) = E_0 \exp(-2\pi kx/\lambda)\ \exp(i2\pi nx/\lambda - i\omega t) \qquad \text{----- (25)}$$

where the direction of propagation is taken to be the x direction and the phase velocity is $C = \frac{C_0}{n}$.

The term $\exp(-2\pi kx/\lambda)$ in equations (24) and (25) shows attenuation which is an absorption of energy of the wave as it travels through the medium. k is called the extinction coefficient in the medium.

The optical constants are composed of two terms, n and k, where n describes how the wave propagate in the medium and k accounts for absorption of energy of the wave as its travels through the medium.

The energy flux at any point in the medium is determined by the Poynting vector, |S|. For a homogeneous wave propagating in the x direction, the magnitude of the Poynting vector is

$$|S| = \frac{1}{2}\mathrm{Re}\left\{\sqrt{\frac{\varepsilon}{\mu}}\right\}|E_0|^2 \exp\left(-\frac{4\pi k x}{\lambda}\right) \qquad \text{----- (26)}$$

Sometimes, the magnitude of S is denoted by I, either called the irradiance (its dimensions are energy per unit area and time) or intensity.

Equation (26) may be rewritten as

$$\frac{I(x)}{I_0} = \exp(-\alpha x) \qquad \text{----- (27)}$$

where I(x) is the radiance at position x and I_0 is its value at arbitrary initial point.

The coefficient α is the absorption coefficient, given

$$\alpha = \frac{4\pi k}{\lambda} \qquad \text{----- (28)}$$

The Kramers-Kronig Relations

The Fourier transform is used to justify the relation between P and E (or E and H) because it is uncertainty a low that all electromagnetic fields must be harmonic in time. If the Fourier transform $X(\omega)$ of a function X(T) is expressed as a product of Fourier transforms, then

$$X(\omega) = Y(\omega) \cdot Z(\omega)$$

By using the convolution theorem

$$X(t) = \int_{-\infty}^{\infty} Y(t-t')Z(t')dt'$$

where

$$Y(t) = \frac{1}{2}\int_{-\infty}^{\infty} Y(\omega)\exp(-i\omega t)d\omega$$

For example, the polarization (dipole moment per unit volume) induced by the applied field is

$$P(\omega) = \varepsilon_0 \chi(\omega) E(\omega) \qquad \text{----- (29)}$$

The real, true dependent polarization is given by the Fourier transform as

$$P(x,t) = \int_{-\infty}^{\infty} G(t-t')E(x,t')dt' \qquad \text{----- (30) where}$$

$$G(t) = \frac{1}{2\pi} \int_{0}^{\infty} \varepsilon_0 \chi(\omega) \exp(-i\omega t) d\omega \qquad \text{----- (31)}$$

The function G(t) describes the time response of the polarization to an abrupt change in the electric field. Due to the casualty, if a steady electric field is applied to a sample of matter for a sufficient period of time, a steady polarization will be induced in the sample. However, if the electric fields were suddenly removed, the polarization would not immediately drop to zero but would decay according to a characteristic time constant so, G(t) must be zero for $t < 0$. This gives the restriction for the equation (21) that the casualty condition may satisfy only if the susceptibility satisfies the relations

$$\chi'(\omega) = \frac{2}{\pi} P \int_{0}^{\infty} \frac{\omega' \chi''(\omega)}{\omega'^2 - \omega^2} d\omega' \qquad \text{----- (32)}$$

$$\chi''(\omega) = -\frac{2\omega}{\pi} P \int_{0}^{\infty} \frac{\chi(\omega')}{\omega'^2 - \omega^2} d\omega' \qquad \text{----- (33)}$$

where P is the Cauchy principal value of the integral

$$\lim_{a \to 0} \int_{-\infty}^{\omega - a} \frac{\chi'(\omega)}{\omega' - \omega} d\omega' + \int_{\omega + a}^{\infty} \frac{\chi(\omega')}{\omega' - \omega} d\omega'$$

and ω' is the particular frequency where χ' and χ'' needs to be evaluated.

Equations (32), (33) are examples of Kramers - Kronig relations. They show that the real and imaginary parts of susceptibility are related, which means that if one part is known at all frequencies, the other part may be computed. The Kramers-Kronig relationship requires the assumptions that these equations are linearity and causality

These equations can apply to a very wide range of physical systems, since the frequency response function of any causal linear system must obey the relations similar to these. This leads to the important result that the optical constants n and k are related by the Kramers - Kronig relations.

$$n(\omega) = 1 + \frac{2}{\pi} P \int_0^{\infty} \frac{\omega' k(\omega')}{\omega'^2 - \omega^2} d\omega'$$

$$k(\omega) = 1 + \frac{2}{\pi} P \int_0^{\infty} \frac{\omega' k(\omega')}{\omega'^2 - \omega^2} d\omega'$$

Radiative Properties of Particles

Radiative properties of single particles

When the electromagnetic wave (or photon) passes through the medium with particles, some of electromagnetic wave may be attenuate, which depends on the properties of particles and medium. The attenuation of light (electromagnetic wave) may compose of the absorption and the scattering. The scattering may occur in three separate phenomena as shown in Figure 1.

1. Diffraction: waves never come into contact with the particle, but their direction of propagation is altered by the presence of the particle.

2. Reflection by a particle : waves reflected from the surface of particle

3. Refraction in a particle: waves that penetrate into the particle, and after partial absorption, re-emerge with a different direction or propagation.

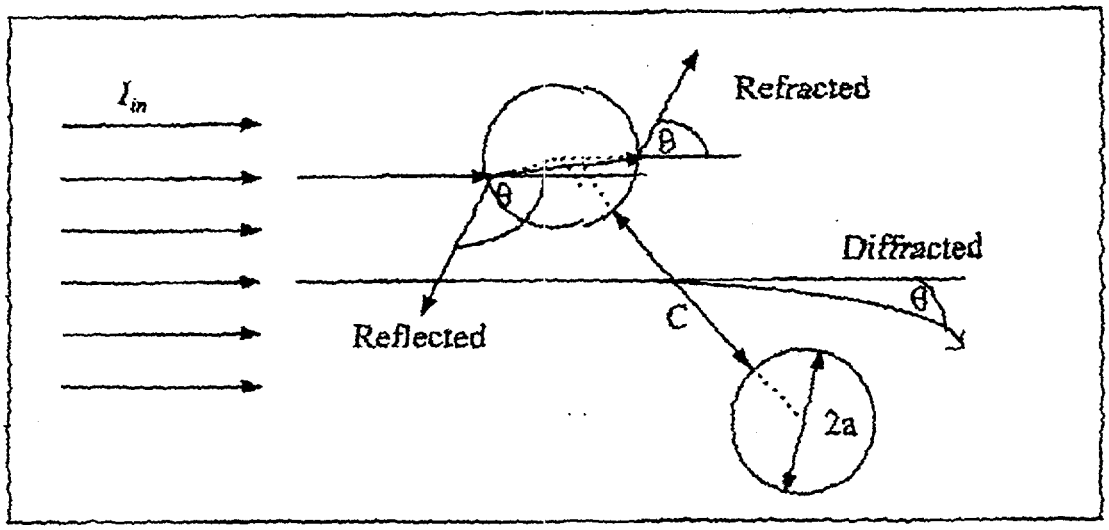

Figure 1. Interaction between electromagnetic waves and spherical particles. C is the interparticle distance, and a is the paricle radius.

Although absorption is usually the dominant mode of the attenuation in homogeneous media, scattering is not entirely absent. In some media, the scattering becomes more important. The scattering of single particle can be considered in a variety of ways such as optical properties, particle size, particle shape and the incident radiation. Figure 2 shows the parameters affecting scattering in a single particle.

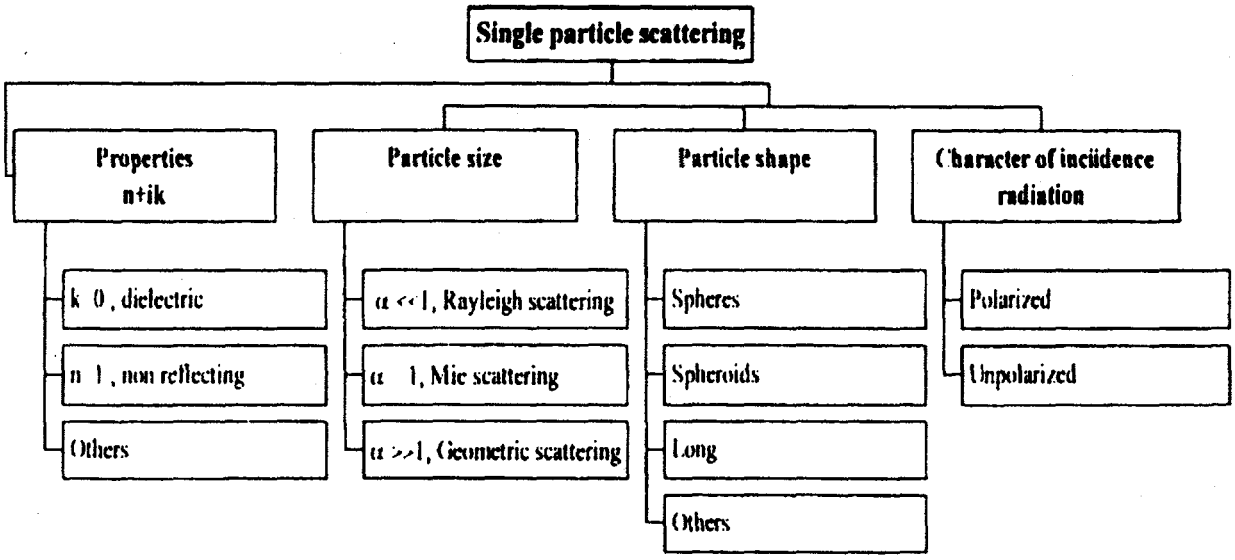

Figure 2. The parameters that affect scattering in a single particle.

The absorption and scattering characteristics of a particle are determined by two parameters.

1. the particle size parameter x, which is defined as $ka = 2\pi Na/\lambda = \pi ND/\lambda$ where D is the particle diameter and x is the wavelength of radiation

2. the complex refractive index (N) of the particle material.

The radiative properties of single particles are the phase function, Albedo, forwardness factor, absorption cross-sections, absorption efficiencies, absorption coefficients, scattering cross-sections, scattering efficiencies, scattering coefficients, extinction cross-sections, extinction efficiencies and extinction coefficients. Figure 3 shows the radiative properties of single particles.

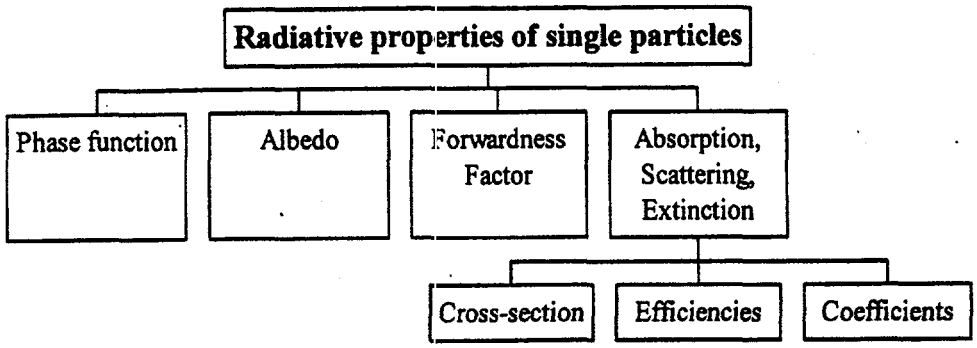

Figure 3. Radiative properties of single particles.

The cross-sections.

The cross-sections are defined as the ratio of the energy loss to the incident energy flux, having the units of area. The extinction cross-section is summed between the scattering cross-section and the absorption cross-section, i.e.

$$C_{ext} = C_{sca} + C_{abs}$$

where C_{sca} = scattering cross-section and C_{abs} = absorption cross-section

The extinction cross-section is the total extent of absorption and scattering.

The efficiencies (or efficiency factors)

The efficiency has been used more than cross-section because of its dimensionless. The efficiencies are defined as

$$Q_{ext} = \frac{C_{ext}}{G}, \quad Q_{sca} = \frac{C_{sca}}{G}, \quad Q_{abs} = \frac{C_{abs}}{G}$$

$$Q_{ext} = Q_{sca} + Q_{abs}$$

where G is the particle cross-sectional area projected onto a plane perpendicular to the incident beam ($G = \pi a^2$ for sphere of radius a). The extinction efficiencies can never be greater than unity.

The coefficients(a_n and b_n)

The coefficients are defined as the fraction of the energy loss from the propagating wave per unit distance of the travel and therefore have dimensions inverse of length. The value of a_n and b_n can be found from the calculation in "Bohren C.F. and Huffman, D.R., *Absorption And Scattering of Light by Small Particles.*[16]

The Albedo of single scatter(ω)

The albedo of single scatter is defined as the ration of the amount of radiation scattered in all direction to the total radiation intercepted by it. Albedo varies from zero for a purely absorbing particle to one for anon-absorbing particle depending on the complex refractive index of particle material and the size of particle.

Normally, small particles have high albedo values. On the other hand, large particles have low albedo values. The albedo may scatter radiation in both forward and backward directions depending on its refractive index and size. Figure 4 shows the schematic representation of Isotropic and Anisotropic scatter by a single particle.

The forwardness factor (g) denotes the degree of anisotropy of its scattering character and is defined as the average cosine of the scattering angle, or the symmetry parameter.

$$g = <\cos\theta> = \int_{4\pi} p\cos\theta d\omega$$

where p is the phase function and is outlined in the next section.

For fully forward scattering, it assumes a value of g equal "1", "-1" for fully backward scattering and "0" for isotropic (the same in all directions) scattering or scatter having forward-backward symmetry.

For single particle, the size parameter (x) decreases from a large value to unity, scatter increases and transfers from being predominantly forward to having a significant backward component.

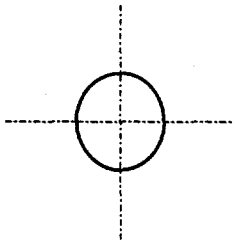

Isotropic Scatter (g = 0)

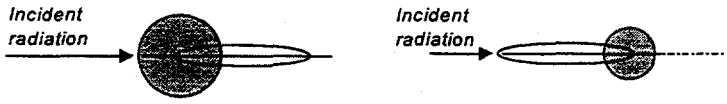

Anisotropic Forward Scatter (g>0) Anisotropic Back Scatter (g<0)

Figure 4. Schematic Representation of Isotropic and Anisotropic Scatter by a Single Particle.

Phase function $p(\theta,\phi)$

Phase function describes the detailed behavior of scattering in all four steradian. It is defined as the ratio of the energy scattered in the (θ,ϕ) direction per unit solid angle to the total energy scatted in such a way that integration of $p(\theta,\phi)$ over 4π steradians is unity

The polar angle (θ) is the angle that the direction of scatter makes with the incident direction. The polar angle may be termed as the angle of scatter. The azimuth angle (ϕ) is the angle in the plane normal to the incident direction.

The phase function may be defined as

$$\frac{1}{4\pi}\int_0^{2\pi}\int_0^{\pi} p(\theta,\phi)\sin\theta d\vartheta \cdot d\phi = 1$$

or

$$\frac{1}{2}\int_{-1}^{1} p(\mu)d\mu = 1.0 \quad \text{where } \mu = \cos\theta$$

From the Mie theory, a procedure can be developed to determine all of the radiative properties. This is described in a later section of this appendix. According to this theory, the particle size parameter will determine the interaction of the particles with the thermal radiation (light):

1. For $x << 1.0$: absorption and emission is directly proportional to the concentration of particles and scattering of radiation is not significant (this is the case for extremely fine particle, D $\approx$0.01 microns).

2. For $x \approx 1.0$: Both absorption/transmission and scattering are significant. Scatter in this case is predominately forward direction but with significant proportions in both sideways and backward directions.

3. For $x >> 1.0$: Absorption and emission are proportional to the projected area of particles, and although the scattering of radiation is significant, most of the scattered radiation is forward direction.

Radiative properties of a particle cloud.

In the actual equipment, the occurring of the small particles may consider as the cloud particle. In this section, the classification of scattering is outlined.

The radiative properties of a particle cloud can be obtained from the single particle properties. The procedure depends on the system of particles.

Single/multiple scatter

If a single ray of radiation transversing through the medium is scattered only once before leaving it, this is defined to be single scattering. On the other hand, if more than one scattering occurs per ray, the medium is said to be multiple scattering. Therefore, multiple scattering referred to the interaction of a scattered wave with another particle.

To define medium as single or multiple scattering, the optical depth (τ_s), the product of physical path length (L) and the scattering coefficient. For single scattering, $\tau_s < 1$.

Independent/dependent scattering

When the interaction of the particle with the radiation field is not affected by the proximity of the neighboring particles, It is called independent scattering. Otherwise, It is called dependent scattering. The independent theory assumes no electromagnetic interaction between the various particles in the system and each particle has the same incidence. The interference of the waves scattered from the different particles is also neglected. The independent scattering must has the interparticle distance (C) larger than 0.5 ($\frac{C}{\lambda} > 0.5$) compared to the size and wavelength and there must be no interaction between the scattered fields. The energy absorbed (or scattered) by a collection of particles is the algebraic sum of the energy absorbed (or scattered) by each particle.

If the influences of the neighboring particles have an effect to the scattering and absorption characteristic of a particle in a medium, It is said to be dependent effects. Dependent effects bear to heat transfer applications like fluidized bed, packed-beds, reactors, deposited soot layer and soot agglomerates (Tien and Drolen[17]). Figure 5 shows the regime map for independent and dependent scatter.

The extent of dependent affects on the complex refractive index, particle size and volume fraction of the particles in the equipment. Dependent effects can be determined from the Maxwell's equation of electromagnetic theory provided information on the packing arrangement of the particles, and the boundary conditions are available. The complete solution is, however, very difficult to obtain. Dependent effects have been analyzed in the literature of either very small particle (Rayleigh size) or large particle (0.2 mm or above). No studies appear to have been reported for the intermediate size range of particles.

No approaches or appropriated theories are also available for modeling dependent effects involving particles in the intermediate size range. In this study, the procedures are discussed only for the independent and single scattering because the intermediate size range used in this study is approximately 1. Further, some previously studies showed that for the ash particles, considering only the independent and single scattering should be enough to predict the radiative properties of particles, even though the dependent effects will have fairly significant effects on the optical constants.

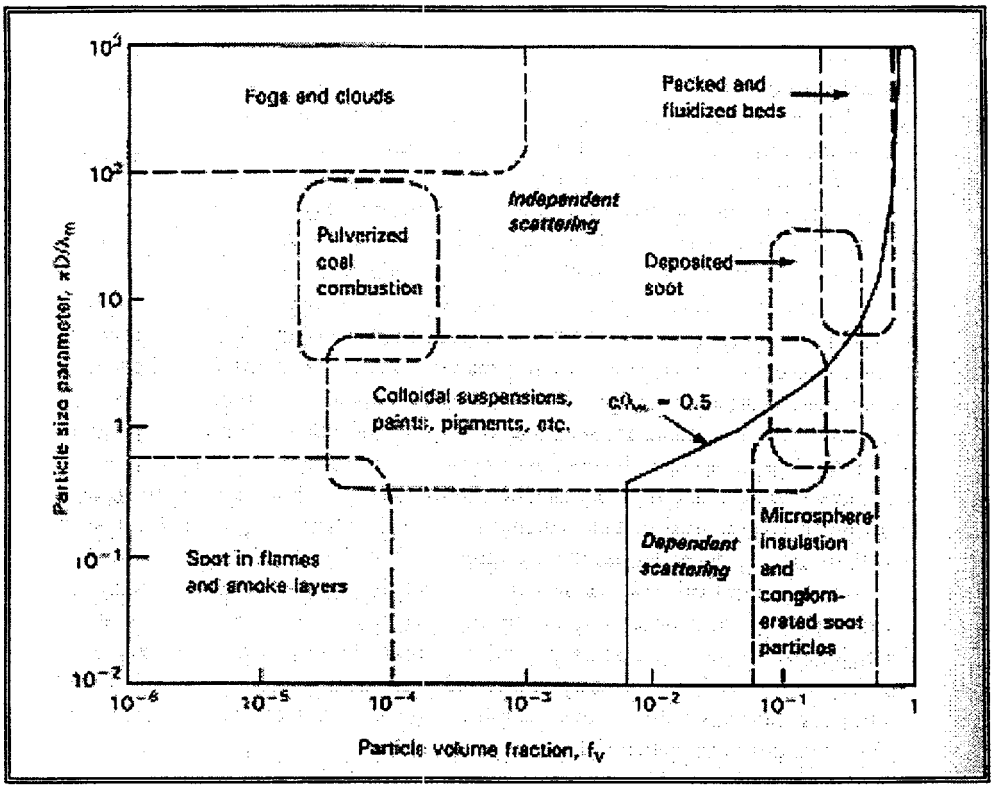

Figure 5. Map of independent and dependent scattering regimes as a function of particle size parameter and volume fraction.

Technique of Measuring Real and Absorption index

There are various experimental techniques used to obtain the optical constants data. The technique best suited to a particular material depends on several factors such as its accuracy, the type of material being used, the expected values for the optical constants, wavelength range of measurement, size parameter and availability and quality of both optical elements and equipment.

Generally, no one technique is suitable for the entire wavelength. A combination of two or more techniques has to be employed.

In order to find two unknown quantities, n and *k*, either of the following are required:

1. Two independent measurements

2. One measurement and a suitable theory such as Mie theory or a relationship linking n and *k* (i.e. Kramers-Kronig)

In this study, the particle extinction technique was employed. Measurements were made with fine particles dispersed and suspended in an infrared transmitting material (KBr). It was assumed that the particles were not agglomerated, and of the same size as before suspension in the KBr. Interpretation of the infrared transmission was interpreted by applying the Mie theory and Kramers-Kronig relationships to get values of real and absorption index. This particle extinction technique was used in this study

because the other techniques were far more difficult to perform experimentally, or far more difficult conceptually. When compared with other techniques, this one is relatively simple and highly accurate.

Particle extinction technique

The micron-sized particles were suspended in KBr and assumed that particles were in particulate form in the same size as before suspension. The transmissions across the pellet were measured and then converted to the absorption by using the Fourier transform spectrometer (FT-IR). The detail of FT-IR is discussed in the subsequent section.

Mie Theory

Mie theory is used for solving the problem of the scattering and absorption properties by assuming the simple case of single-particle scattering that is a plane electromagnetic wave scattered by a uniform spherical particle (homogeneous particle).

First, the wave equation is solved in a coordinate system appropriate to the problem, and then the electric and magnetic fields are required to satisfy continuity conditions on the surface of the sphere. The result expressions give the extinction and scattering efficiencies and the particle phase function. The incident plane wave must also express in a form as an infinite series of spherical (wave functions) in order to complete the solution.

The Mie solution depends on only two parameters: the refractive index of the particle relative to the surrounding medium, $N= n +ik$, and the ratio of the particle size to the wavelength which is expressed in the form

$$x= \pi D/\lambda$$

where D = diameter of the particle and x = size parameter.

The solutions have different properties depending on whether x is small, comparable to, or large compared with unity and also depend on whether the electric vector in the incident wave is perpendicular to or parallel to the scattering plane. Details of the calculation procedure are provided in Addendum A of this appendix.

Kramers-Kronig relationships

In order to calculate the absorption index after obtaining the approximate real index from the Mie theory calculation, the Kramers-Kronig relations are used by considering the consequences of causality and analyticity. By extending the fast Fourier algorithm along with the time-domain method to the Kramers-Kronig relationships. The determination of optical constants can be determined faster than ordinary Kramers-Kronig relation.

Frequently, two quantities of physical interest can be theoretically related to the real and imaginary parts of a complex function. The real and imaginary parts in turn can be related to each other by observing that the physical system can response to a physical input only after the time of that input but not before.

The time-domain method is based on two simple observations:

1. A physical system's impulse response, which is zero for negative times, can be expressed as a sum of two functions that have, respectively, even and odd parities; the two functions are equal for positive times and have opposite signs for negative times.

2. The Fourier transforms of these two functions are, respectively, the real and imaginary parts of the same physical system's frequency response.

The impulse response I(t) of a linear system, in the time domain following the input of an impulse, is the Fourier transform of the frequency response, F(ω)

$$I(t) = \frac{1}{2\pi} \int_{-\infty}^{\infty} F(\omega) \exp(i\omega t) d\omega \qquad \text{----- (1)}$$

where the frequency response is given by

$$F(\omega) = \int_{-\infty}^{\infty} I(t) \exp(-i\omega t) dt \qquad \text{----- (2)}$$

The condition of causality is $I(t) = 0$ for $t<0$ ----- (3)

Because I(t) is real, i and ω appear in equation (1) only in the combination iω, and therefore

$$F(-\omega) = F(\omega)^{*} \qquad \text{----- (4)}$$

or

$$F(\omega) = S(\omega) + iA(\omega) \qquad \text{----- (5)}$$

where S(ω) is real and symmetric [even, $S(\omega) = S(-\omega)$] about $\omega = 0$, and A(ω) is real and anti-symmetric [odd, $A(\omega) = - A(-\omega)$] about $\omega = 0$.

If S(ω) from eq.(5) is inserted for F(ω) in eq. (1), a real symmetric function of time, $I_S(t)$, will be the real anti-symmetric function $I_A(t)$.

Because eq. (1) is a linear relationship,

$$I(t) = I_S(t) + I_A(t) \qquad \text{----- (6)}$$

For the causality relation eq. (3),

$$I_A(t) = -I_S(t) \quad \text{for } t<0 \qquad \text{----- (7)}$$

Because $I_A(t)$ and $I_S(t)$ are of opposite symmetry types, eq. (7) implies

$$I_A(t) = I_S(t) \quad \text{for } t>0 \qquad \text{----- (8)}$$

Equation (7) and (8) define $I_A(t)$ in terms of the known I_S and the inverse transform (2) yields finally

$$iA(\omega) = \int_{-\infty}^{\infty} \exp(-i\omega t) I_A(t) dt \qquad \text{----- (9a)}$$

$$iA(\omega) = -\int_{-\infty}^{0} \exp(-i\omega t) I_S(t) dt + \int_{0}^{\infty} \exp(-i\omega t) I_S(t) dt \qquad \text{----- (9b)}$$

$$iA(\omega) = -\frac{1}{2\pi} \int_{-\infty}^{0} \exp(-i\omega t) dt \int_{-\infty}^{\infty} s(\omega) \exp(i\omega t) d\omega + \frac{1}{2\pi} \int_{0}^{\infty} \exp(i\omega t) dt \int_{-\infty}^{\infty} S(\omega) \exp(i\omega t) d\omega$$

----- (9c)

To calculate the imaginary part of the frequency response from the real part, first, Fourier transform the real part to the time domain eq.(1), second, invert algebraic signature for all negative time eq.(7), and third, Fourier transform back to the frequency domain eq.(9a). The result will be the imaginary part of the frequency response.

Similarly, in order to calculate the absorption index from the known real index, this alternative Kramers-Kronig relation can be used effectively.

3.3.4 Fourier Transform Infrared Spectroscopy

Disperse infrared spectroscopy had traditionally been an important tool in fuel characterization because most organic and mineral components absorb in the infrared region. Fourier transform infrared (FT-IR) spectroscopy offers many advantages that can extended the usefulness of infrared studies of coal and other hydrocarbons. FT-IR provides high sensitivity because of its high-energy throughput and its ability to co-add spectra.

Fourier transform infrared (FT-IR) absorption spectroscopy has been used previously as an in-situ diagnostic for gas species concentration and gas temperature. Recently, the applications of emission/transmission spectroscopy were used for measuring particle temperatures in non-combusting media, measuring particle emittance, measuring temperature and concentration of gases and soot on both combusting and non-combusting media, and quantitative infrared analysis of gas suspended solids.

There are two features of FT-IR spectrometers that are ideal for this purpose.

1. FT-IR spectrometers modulate their source radiation; each source frequency has a unique modulation frequency. The detector is sensitive only to the modulated radiation so that unmodulated emitted and reflected furnace radiation does not interfere with the measurement of reflectance or transmittance. This feature eliminates the need for chopping, and it permits simultaneous detection at all frequencies.

2. FT-IR spectrometers are fast and sensitive because they measure all frequencies simultaneously.

Other advantages of the FT-IR are the digital storage of spectra and the availability of many data analysis routines that were developed to take advantage of the computer that an FT-IR requires. These routines permit such operations as baseline corrections, library searches, solvent and mineral subtractions, spectral synthesis, and factor analysis.

Summary

1. In order to calculate the complex refractive index of ash, the transmission method (KBr extinction technique) by dispersing powdery samples in infrared transmassive material (KBr) was employed. The particles were assumed to be spherical and homogeneous in composition, and the Mie theory was used to calculate the efficiencies or cross-section of absorption and the scattering curve. Finally, the Kramers-Kronig relation was applied to find the absorption index of the materials.

2. The calculation for the extinction efficiencies or extinction cross-section in Mie theory was provided by the code (computer program) of " Bohren and Huffman[16].

3. The simulation programs to calculate the complex refractive index from Mie theory code and Kramers-Kronig relation (the program includes all the calculations) was purchased from Advanced Fuel Research, East Hartford, CT.

EXPERIMENTAL METHODS

Introduction

As discussed earlier, the KBr extinction technique gives reasonable results for the determination of n and *k* (optical constants) and, moreover, requires less complicated equipment and measurement procedures. In this study, transmission infrared spectroscopy of the powdered materials dispersed into the KBr pellets was used to obtain the real absorption and scattering spectra of the materials.

Ash samples taken from kraft recovery boilers were examined including the pure inorganic material for being the reference of the specific bands in the wavelength regions. A Fourier transform spectrometer (FT-IR) was employed to collect the signal data and then convert to the absorption spectrums data. For preparing the pellet samples, the KBr pellet die kit and the pellet pressure press were used.

Mie theory can be used for predicting the interaction of light with particles of a size comparable to that of the wavelength of light by assuming the simple case of homogeneous single-spherical particle scattering. With these constraints, scattering depends on two parameters, the refractive index of the particle relative to that of the surrounding medium, and the ratio of the particle size to the wavelength. On this basis, Mie theory was used to predict the extinction coefficient using an approximate set of n and *k* and compare with the experimental data.

Finally, the alternative Kramers-Kronig relation (time domain version) was employed to precisely determine the refractive index of the ash particles.

A computer program of Mie theory, published in Bohren and Huffman[16] was modified to take into account the finite acceptance angle of the detector. It was used along with the simulation program provided by Advanced Fuel Research, Inc., to reduce the extremely difficult iterative calculation process.

Experimental Set-up

Fourier-transform infrared spectrometer

In this study, a Fourier-transform infrared Michelson MB series 100 spectrometer used to obtain transmission and absorption data. A gas-tight compartment was constructed over the top of FT-IR to eliminate the effects of moisture and other impurities in the gas path, and to protect the instrument. The characteristics of the FT-IR are as follows:

Laser type : He-Ne with wavelength 632.8 nm, 25uW max.

Detector : MCT, ranging from 500 - 5000 cm^{-1}

Spectral characteristics : 4 cm^{-1} resolution and 32 scans (co-added)

Wave number range : 400-7800 cm^{-1}

A data acquisition computer was connected to the detector to convert raw signal into the spectrum signal through the DSP board. Lab-Calc software program was used to process the infrared spectrum data.

KBr pellet maker kit and pellet pressure press

An evacuable stainless steel KBr pellet die and hydraulic press were used to produce 13 mm KBr pellet that contained samples of the precipitator catch samples.

Material samples

The precipitator catch (ash) samples used in this study were obtained from six different kraft recovery boilers. Spectra for samples of reagent grade sodium and potassium sulfates and carbonates were also obtained to provide specific reference band spectra.

Sample	Designation
Mill samples (precipitator catch)	A1[1]
	A2[1]
	B
	C
	D
	E
	F
Pure Inorganic material	Na_2SO_4
	Na_2CO_3
	K_2SO_4
	K_2CO_3

[1]For recovery boiler A, samples of ash were obtained from both halves (north and south) of the electrostatic precipitator. They are designated A1 and A2, respectively.

The precipitator catch samples were analyzed for ionic components, and the bulk density of each was measured.

Sample Preparation

All the material samples should be dried in an vacuum oven at least 3-4 days. This was critical because moisture in the samples will result in absorption peaks that interfere with peaks from the spectra

of the inorganic salts. Moreover, moisture can cause the problems in the process of making the pellet. Pellets made from improperly dried ash turn white instead of transparent. This is due largely to the escaping of water from the pellet, thus causing microcracks in the pellet. These microcracks affect the scattering and absorbance of incident radiation by the samples.

After drying, the samples were ground to a size of less than 10 microns so as to insure that their absorbance would be is large. This makes the analysis more accurate. The contribution of scattering to the absorbance at low wave number is small, and this makes it easier to separate the effect of scattering and absorbance. Particle sizes were checked with a scanning electron microscope.

For each pellet, about 50 mg of the desired ash sample was placed into a stainless steel capsule, 1/2 " diameter and 1" long. The capsule was sealed with the electrical tape and placed into a Spex mixer/mill for at least 20 minutes.

Mass of Sample in Pellet

The amount of the samples use for making each pellet has to be chosen according to the density of the samples in order to make sure that the absorbance is high enough to avoid noise level (typically 0.4-0.5) and not exceed the saturation level (approximately 1.5). Materials such as precipitator catch samples have an index of refraction close to that of KBr (which has low scattering) and large absorption peaks. It was necessary, therefore, to produce 2 pellets for each analysis: one to determine accurately the scattering (n_0), which requires a large sample mass to have enough absorbance above the noise level, and the other to determine the absorption (k_v), which requires a small sample mass to avoid saturation. For the ash samples, the amount typically used for making a pellet was about 1.5-2.0 mg for the determination of n_0 (the scattering). For k(v) (the absorption), a smaller amount, about 0.5-1.0 mg, was used to avoiding saturation. When two pellets are made, the model is run for the determination of k_v with the low-mass pellet with the values of n_0 and particle size obtained from the high-mass pellet.

Pellet Pressing

Quantitatively place about 300 mg KBr in a mixing capsule, stainless vial. Accurately transfer the sample to the mixing capsule, and add the mixing ball. Use appropriate amounts of sample (between 0.5 and 2.0 mg) depending on the sample density. Secure the cap onto the mixing capsule using electrical tape. Mix the sample for 30 seconds in the Spex mixer/mill to break up any ash particle agglomerates. Remove the stainless steel mixing ball from the vial. Clean the pellet press and dry it at low temperature in a vacuum oven. Pour the KBr/sample mixture over the pellet die after taken from the vacuum oven in order to eliminate the moisture in the sample during the mixing and pressing process. Drop the plunger in slowly and turn it each direction to spread the mixture evenly. Connect the vacuum hose at the bottom of the pellet press assembly, place the stainless steel block on the plunger, and press to 10 tons. Hold at 10 tons for about 30 seconds. Release the pressure, remove the vacuum hose and remove the die by using the plastic open ring on the top and apply pressure to force the die and pellet out. Use the tweezers to place the pellet into the pellet holder, and place the pellet holder into the socket on the FT-IR

Absorbance Measurement

Before getting the transmission spectrum, the FT-IR should be turned on ald allowed to equilibrate for at least 15 minutes with dry N_2 circulating in the FT-IR and on the top compartment where the transmission spectra will be kept. This is necessary to eliminate the moisture in the machine. All data should be collected as interferograms or single beam spectra because of the consistency. The reference absorbance has to be taken before and after taking the absorbance spectrum of the samples in order to get an accurate value of the reference background. Take the average of two background scans to use as the

reference. Weigh the KBr pellet and record the weight. Take the ratio the sample scan tot the reference scan and convert to absorbance. It is also necessary to measure the absorbance of a pure KBr pellet to account, in the model, for the scattering due to the pellet and the KBr themselves.

In order to get good reproducibility in the spectrum values, several runs may be needed at each condition.

Possible Problems

Care must be taken to eliminate the information of microcracks in the KBr during the few minutes following the pressing of the pellet. Microcracks make the pellet turn from transparent to whitish, and they contribute to scattering. They are likely caused by water escaping the pellet, which results in stress in the KBr. The problem may not occur with certain materials such as coal, possibly because coal allows some stress relief. In the case of non-transparent pellets, the following precautions should be used:

- using previously-dried KBr and particles mixture before pellet pressing to avoid a high moisture content
- measuring the FT-IR spectrum pellet immediately after pressing, while the pellet is still transparent.

Uncertainty in Absorbance data

The uncertainty in absorbance is estimated to be ±0.05 absorbance units. In order to insure a good signal/noise ratio, it is thus important to use a sufficiently large amount of sample which will give a large enough absorbance curve without reaching the saturation point which occurs at a level of absorbance greater than ~1.5.

Scattering Model: Mie Theory

The scattering model is based Mie Theory, and is implemented as the computer code included as Addendum B at the end of this appendix. The predicted parameter, extinction efficiency, is the result of the interaction of the light with the spherical particles of size comparable to the wavelength.

A modification of the original program was introduced in order to account for the finite (nonzero) acceptance angle of the detector. F(V) is referred to the extinction accounting for the acceptance angle.

n and *k* Determination Method

Summary of method

1. Mie theory is used, with trial values of $n_\nu = n_o$ (a constant), $k_\nu = 0$ and a particle diameter D, to calculate a smooth scattering curve which matches the shape of the measured absorbance at high wave numbers (above 1500 cm^{-1}). The value of n_o influences primarily the amplitude of the absorbance in the whole range ν without changing the shape of the curve, while the value of D has an impact on the shape of the absorbance as a function of ν (curvature of the curve)

The first guess for $k_\nu = 0$ corresponds to only the scattering effect of the particle (absorbance = 0) and will be used to find the correct k_ν value. The diameter of the particles may be first estimated from SEM pictures of the particles.

2. The scattering curve, plus a constant to account for the reflection from the pellet surface, is subtracted from the experimental absorbance spectrum and the result is assumed to be pure absorption $A_b(\nu)$, where

$$A_V = \frac{4\pi k_\nu}{\ln(10)\lambda} \times \frac{V_{pellet}}{A_p} = \frac{3}{4} \times \frac{M}{\rho} \frac{1}{A_p} \frac{1}{\ln(10)} \frac{F_\nu}{R}$$

where k_ν = absorption index (imaginary part of refractive index)

λ = wavelength

V_{pellet} = Volume of pellet

A_p = Area of the pellet, 13 mm diameter

M = mass of particles

ρ = density of the particles

F_ν = particle extinction efficiency accounting for the acceptance angle of the instrument

A_ν can be calculated from this equation because of the assumption that the particles absorb light in the same way of the a slab of similar pure material of a surface area equal to that of the pellet and of the same weight of the particles.

3. k_ν is calculated from this equation, and the alternative Kramers-Kronig relation is used to determine the correction dn_ν to n_0, which gives a first estimate of n_ν

4. For an increased precision of the values of n_ν and k_ν, another round of the calculations is performed, where the scattering curve calculated using the new value of n_ν is subtracted from the experimental curve. The result assumed to be absorption, from which k_ν is extracted. The scattering curve is then recalculated, using the determined n_ν and k_ν. This step insures full Kramers-Kronig consistency between n_ν and k_ν.

5. This step constitutes a refinement of n_ν and k_ν in the case of large particles and / or large absorption. Consequently, the refinement of n_ν and k_ν is done iteratively, and incremental changes of n_ν and k_ν, dn_ν and dk_ν, are calculated using still the same procedure of subtraction of the predicted absorbance from the experimental absorbance to achieve a perfect or almost perfect match between prediction and experiment.

Possible Limitations

D and n_0 compensation

The diameter of the particles, which is to be adjusted in the software program, has as influence on the value of n_0. Although this value should be pretty well defined by the shape of the scattering curve,

some certainties remain especially when large absorption peaks are present. In addition, the choice of the value of the "offset" parameter can influence the choice of D to fit the scattering contribution to the absorbance. By adjusting this parameter, the fitting process will be easier to proceed.

Choice of n_0 (below or above n_{Kbr})

The scattering of the particles in the pellet is due to the difference in index of refraction of the particles and the KBr. Consequently, two values of n_0 (on the either side of n_{Kbr} = 1.527) can give a similar scattering curve. This uncertainty can be resolved by different methods:

1. Usually, one has a rough idea of n_0 and can eliminate the non-physically realistic value.

2. In the case where both values are reasonable (especially in the vicinity of n_{Kbr}), one can perform the predictions for both values of n_0, and compare the fits. Thee result will be that one prediction is an almost perfect fit, while the other, while being good, does not fit the data as well around large absorption peaks, even by increasing the number of iterations. This is due to the fact that, around an absorption peak, the extinction curve is going to have slightly different shape depending on whether n_0 is higher or lower than n_{Kbr}. The value of n_0 that gives the best fit is the appropriate value.

3. If the both values give essentially the same fit with the experimental curve, other factors should be considered these include the composition of the sample and the values of the constants when compared with the pure components, temperature, and the effect of the particle size used in the calculation.

RESULTS AND DISCUSSION

In this section, the results of the measurement of the optical constants are presented and discussed. The characteristics of the samples used for the measurement are summarized in the first section. The absorbance spectra are shown in the following section. The overviews of the measurement of the optical constants are presented in the third section. Finally, the dependence of the optical constants on composition is examined in detail.

Characterization Measurements

In this study, optical property measurement were made with the four pure inorganic salts, Na_2SO_4, Na_2CO_3, K_2SO_4, and K_2CO_3, and seven ash samples taken from the precipitator catches in different recovery boilers. The ash samples came from six different North American boilers. Two of the samples (A1 and A2) came from the two different sides of the precipitator of the same recovery boiler. The rest (B-F) came from five different mill locations.

The elemental composition of each ash sample was determined by ICP and ion chromatography. They were analyzed at the Central Analytical Laboratory of the Department of Crop and Soil Science at Oregon State University or the Chemical Analysis Laboratory at the Institute of Paper Science and Technology. The apparent density of each ash sample was also needed to calculate the refractive index. The density measurements were made by a volume displacement method.[17]

Elemental composition

The elemental compositions of ash samples are summarized in Table 1. The results of the ICP and Ion Chromatography analyses are in the form of weight percent of the element presented.

Table 1. Major components of the ash samples.

Element	Material						
Weight-%	**A1**	**A2**	**B**	**C**	**D**	**E**	**F**
Na	31.64	30.78	31.53	29.05	31.61	22.70	26.85
K	5.40	5.06	4.08	6.80	4.80	9.96	6.08
Cl	4.67	2.28	14.26	2.70	2.70	0.31	1.69
SO_4^{2-}	42.97	46.15	43.83	52.51	46.22	65.92	60.58
CO_3^{2-}	14.41	13.62	5.2	8.38	12.72	0.10	2.25
Heavy metals and trace elements	0.021	0.024	0.014	0.078	0.030	0.022	0.022
Total	99.11	97.91	98.91	99.52	99.08	99.01	97.49
Cation/anion equivalence ratio	1.00	0.99	0.99	0.99	1.02	0.90	0.96

Table 2. Trace elements in the ash samples.

Element	Material						
ppm	**A1**	**A2**	**B**	**C**	**D**	**E**	**F**
P	17.0	13.0	10.8	57.2	50.4	41.2	35.6
Ca	68.0	97.0	36.6	166.0	120.0	116.0	68.0
Mg	31.0	40.0	34.4	69.2	50.8	12.3	44.4
Mn	28.0	31.0	9.9	49.6	16.8	13.3	37.5
Fe	21.0	10.0	8.5	295	22.9	12.1	41.2
B	8.0	8.0	8.5	12.6	14.0	2.92	5.8
Zn	32.0	41.0	31.5	134.8	23.7	22.9	56.4
Al[2]	<1.0	<1.0	<1.0	<1.0	<1.0	<1.0	<1.0
Si[2]	<1.0	<1.0	<1.0	<1.0	<1.0	<1.0	<1.0
Total	205.0	240.0	140.2	784.4	298.6	220.72	288.9

These analyses show that ash samples are typically high in sodium sulfate content. The samples cover a wide range of potassium, chloride, and carbonate content, however, from 4.0 to 10.0% potassium, 0.3% to 15.4% chloride, and 0.1-14.4% carbonate. All of the carbon shown as elemental carbon was present as carbonate. There were very small quantities of other elements such as calcium, phosphorus, magnesium, etc. (see Table 2). These ash samples probably cover most of the range of variation of composition encountered in precipitator ash from kraft recovery boilers.[18]

[2] The amount of Al and Si is less than the detectable scale of the ICP.

Sample densities

In analyzing the composition dependence of the optical constants, it is necessary to know the apparent density of the samples in order to find the number of particles used in each KBr pellet. To obtain accurate values of the optical constants, the number of particles needs to be known and the particles used in the pellet need to be homogeneous in order to avoid or at least minimize scattering effects.

The volume method, with glycerin as the suspending liquid, was used to determine the apparent density of the ash particles. It was chosen because it is a standard procedure and also because it works well with light, fluffy samples such as precipitator ash. The results of these measurements are given in Table 3.

Table 3. True densities of pure components and bulk densities of ash samples used in this study.

Material	Density (g/cm^3)
Na_2SO_4	2.698
Na_2CO_3	2.533
K_2SO_4	2.662
K_2CO_3	2.290
A1	0.472
A2	0.485
B	0.228
C	0.243
D	0.244
E	0.435
F	0.518

The density range is from 0.2 to 0.5 g/cm^3 for the recovery boiler ash samples. The calculations and data for the density measurements are provided in Addendum C of this appendix.

Particle diameter

In the KBr extinction technique, a small amount of sample was mixed with the KBr to make the pellet. The number of particles and the diameter of the particles need to be known in order to be able to calculate the values of optical constants of the ash mixtures.

Since agglomerates of the recovery boiler ash particles can be much larger than actual size of fume particles, the particles used in this study should be ground to a size of less than 10 microns in order to insure that : 1) the absorbance is larger, which makes the calculation procedure more accurate, and 2) the contribution of the scattering to the absorbance at low wave number (in the region where absorption is strong) is low, which allows a clear separation of the two components, i.e., absorption and scattering. A Spex mixer/mill is used for grinding for at least 20 minutes. The actual diameters of the particles produced were obtained from SEM photographs of the ground ash samples.

From the SEM pictures, the majority of particles and fume particle agglomerates are in the range between 0.5-11 microns. The mean diameter was obtained by counting number of particles in each size class, summing the surface area of the particles in each size class, and dividing by the total number of particles counted. The mean diameter of each particle was then calculated from the average surface area. The average particle size of each sample used in each experiment was summarized in Table 4.

Table 4. Average diameters of particles in the ash and ash component samples.

Material	Average diameter (microns)
Na_2SO_4	2.56
Na_2CO_3	2.77
K_2SO_4	2.95
K_2CO_3	2.73
A1	2.70
A2	3.00
B	1.98
C	1.76
D	2.18
E	1.35
F	1.48

The average diameter of particles in each sample depended on the grinding time and other characteristics of the individual ashes. The mean diameter of the pure inorganic alkali salts was around 2-3 microns, and for the ash samples 1-3 microns. The calculation procedure is shown in addendum D of this appendix.

Particles much larger than 1 micron in diameter were seen in the SEM pictures of the ground ash samples Those greater than 5 microns can weight the average particle diameter toward larger values if they are present in large numbers. The presence of large particles in the pellet also leads to a non-uniform particle size distribution. The value of the slab approximation thickness used in the calculation of the optical constants may vary widely, and would not work well for broad particle size distributions because absorption occurs too differently in small and large particles. The value of *k*, therefore, would vary widely and the analysis would give inaccurate values. Moreover, large particles absorb less compared to smaller particles, and the results probably would be hard to interpret because the contribution of scattering to absorption is high. In the case of an incident wave passing through the particles, it will cause a significant amount of forward scattering when large particles are present so that separation between the incident and forward scattering can be impossible to make. This would lead to a higher value of the absorption index as shown in the results of Kunitomo.[6] Fortunately, the small number of large particles presented in the SEM pictures (1-2 wt-% of the total range size) has a small effect in this study when compared with the huge number of small particle. There is virtually no control over how the particles will line up on mixing because the ash particles were light and fluffy and always agglomerated. Therefore, a narrow size distribution of the particle is preferable to ensure a uniform free scattering to reduce the contribution of scattering to absorption.

Absorbance Spectra of the Samples

The absorbance spectra of pure inorganic alkali salts were first examined in order to view the specific absorption bands and to generate reference spectra for the interpreting ash spectra. With ash samples, the effect of one component may completely overshadow the effect of others; weak or broad features of one component may become dominant and the sharp structures seen in individual components may be smoothed. What exactly would happen with mixtures was unclear, but depended on the concentration of the components. However, the pure inorganic alkali salts references provide a convenient means to compare the measured results with those of the mixed ash samples.

Inorganic alkali salts are known to absorb and emit at wavelengths that give characteristic region of their anions, with cations having little influence. Figure 6 shows the absorbance spectra of the pure inorganic alkali salts; Na_2SO_4, Na_2CO_3, K_2SO_4 and K_2CO_3 that were measured in this study.

From the results, Na_2SO_4 and K_2SO_4 give almost the same absorption pattern. That means that only the anion, sulfate, has an effect on the absorption bands. Sulfate absorbs (emits) in the region of 1240-1040 cm^{-1} (8.06-9.62 μm). It also exhibits weak but distinctive peaks in the 650-550 cm^{-1} (15.38-18.18 μm) region and a very weak band in the 1700-1500 cm^{-1} (5.88-6.45 μm).

$Na_2CO_3$and K_2CO_3 also give almost the same position and amplitude of absorption peaks so that only the carbonate group impacts the absorption band. Carbonate anions emit (absorb) significantly in the region of 1550-1350 cm^{-1} (6.45-7.41 μm). They also exhibit a weak peak at 940-840 cm^{-1} (10.63-11.9 μm) and a very weak peak in the region 750-650 cm^{-1} (13.3-15.38 μm).

The presence of hydroxides and hydrated species overshadow all the pure inorganic samples showing in the region of 3650-3000 cm^{-1} (2.74-3.33 μm) because of the stretching vibration of hydrogen (O-H), relating to the $\bar{\nu}_1$ (2.73 μm) and $\bar{\nu}_2$ (2.66 μm) vibrational modes of the free molecules (Bohren and Huffman[16]).

The absorption bands of these anion are due largely to the vibration of anion group in the infrared region (1.5-20μm). At this range, the vibration-rotation transition of molecules will dominate

over the electronic transition (dominated in the region 0.4-0.7μm). In the region where the electronic transition dominates, temperature has a significant effect on the absorption of the radiation wave, light, while in other regions, temperature has a fairly weak effect.

From figure 1, the absorption peak of the alkali salts appears only in the region 2000-400 cm^{-1} (5-25 μm). At higher wave numbers (>2000cm^{-1}), no other absorption peaks are present except for the hydroxide ion from water (vapor). However, the scattering effects still exist in this region (there is a slight positive slope toward the higher wave numbers) even though the amount of sample and particle size in the pellet was carefully monitored to ensure that the contribution between scattering and absorption would be low. The particle size distribution should be homogeneous to make sure that the slab approximation can be applied to thin pellets as well as to the amount of sample put into each pellet. From the experimental results, the appropriate amount of pure inorganic alkali salts needed in making the pellets was 1.0 mg per KBr 300 mg and 0.4 mg for ash samples per KBr 300 mg. These values were chosen so as not to saturate the FT-IR spectrum, or to have such weak signals that the signal to noise ratio became too small.

NaCl and KCl seems to be less significant when compared with the sulfate and carbonate anions because of small amounts being presented. Moreover, the effects of NaCl and KCl on the optical constants cannot be determined by the present method because of the transparency of KCl in IR range and because NaCl absorbs only at very high wavelengths (above 50 microns). Therefore, meaningful absorbance spectra of these materials were not obtained in this experiment. A summary of the absorption bands of the pure inorganic sulfates and carbonates is given in Table 6-5.

Table 5. Summary of the absorption bands of pure inorganic salts.

Inorganic Salts	Band regions (μm)	Band region (cm^{-1})	Band strength
Na_2SO_4	1240-1040	8.06-9.62	strong
	650-550	15.38-18.18	weak
	1700-1500	5.88-6.45	very weak
Na_2CO_3	1550-1350	6.45-7.41	strong
	940-840	10.63-11.90	weak
	750-650	13.30-15.38	very weak
K_2SO_4	1240-1040	8.06-9.62	strong
	650-550	15.38-18.18	weak
	1700-1500	5.88-6.45	very weak
K_2CO_3	1550-1350	6.45-7.41	strong
	940-840	10.63-11.90	weak
	750-650	13.30-15.38	very weak

The polarization mechanisms (electronic, vibration, and dipolar) are the major contributors to absorption at low frequencies. Each mechanism occurs at a different wavelength. In the infrared region, the vibration and rotation of the molecule when receiving energy or photons will be the dominant mode over the electronic mechanisms, active at very high wave numbers (typically in the ultraviolet and visible

regions), and dipolar mechanisms, active in the microwave regions. In between each region of absorption the material is transparent, with $k \sim 0$ and n = constant.

The n and k of a material are related according to the Kramers-Kronig relationship equations,

$$n(\omega) = 1 + \frac{2}{\pi} P \int_0^{\infty} \frac{\omega' k(\omega')}{\omega'^2 - \omega^2} d\omega'$$

$$k(\omega) = -\frac{2\omega}{\pi} P \int_0^{\infty} \frac{n(\omega')}{\omega'^2 - \omega^2} d\omega'$$

The real refractive index, n, will be constant at high wave number (>2000 cm^{-1}), i.e. in between the molecular absorption region and the electronic absorption region. It will be equal to the free-space value (n=1) at very high wave numbers (far above the electronic absorption bands) or high frequencies so that none of the polarization mechanisms can respond ($\lim_{\omega \to \infty} n(\omega) = 1$).

The absorbance spectra of ash samples were compared with the absorbance spectra of the pure inorganic salts as references. Figures 7-9 shows the absorbance spectra of the ash samples used in this study.

For ash samples A1 and A2, the absorbance bands appearing at 1240-1040 cm^{-1} (8.06-9.61 μm) is significant, and bands are seen distinctive at 1550-1350 cm^{-1} (6.45-7.47 μm) and 650-550 cm^{-1} (15.38-18.18 μm). There are very weak peaks at 940-840 cm^{-1} (10.63-11.90 μm) and 1700-1550 cm^{-1} (5.88-6.45 μm).

Like the absorption spectrum of ashes A1 and A2, samples B, C, and D are similar, with the band positions at almost the same wavelengths. On the other hand, samples E and F do not show the distinctive peaks at 1550-1350 cm^{-1} (6.45-7.47 μm) and 940-840 cm^{-1} (10.63-11.90 μm). These are the characteristic out-of-plane bending modes of carbonate ion (CO_3^{2-}). That means ashes E and F have only the absorption bands associated with sulfate anions (SO_4^{2-}). This agrees well with the composition data for ash E and F. There are only a few percent of carbonate in these two ashes (Table 6-1), and it is almost undetectable in their infrared spectra.

In summary, the absorption results seem to correspond to the reference spectra peaks from pure inorganic alkali salts, and were in line with the proportional composition of each sample.

The Measured Optical Constants

The absorption spectra obtained by the KBr extinction technique were used to calculate the optical constants of each sample via the Mie scattering theory and the Kramers-Kronig relationships. These calculations were performed using software purchased from Advance Fuel Research.

In the calculation program, three separate calculation windows appear. The first one was used for the KBr pellet data such as the absorbance spectrum, amount of sample used, offset parameter, the graph of the raw absorbance spectrum, the pure KBr spectrum, and the modified spectrum after subtracting the KBr spectrum from the raw absorbance spectrum. The offset parameter is used to offset the experimental absorbance to insure that the absorbance is close to 0 at low wave numbers, to account for any additional loss of light not related to the particles. The middle window displayed the variable inputs that must be

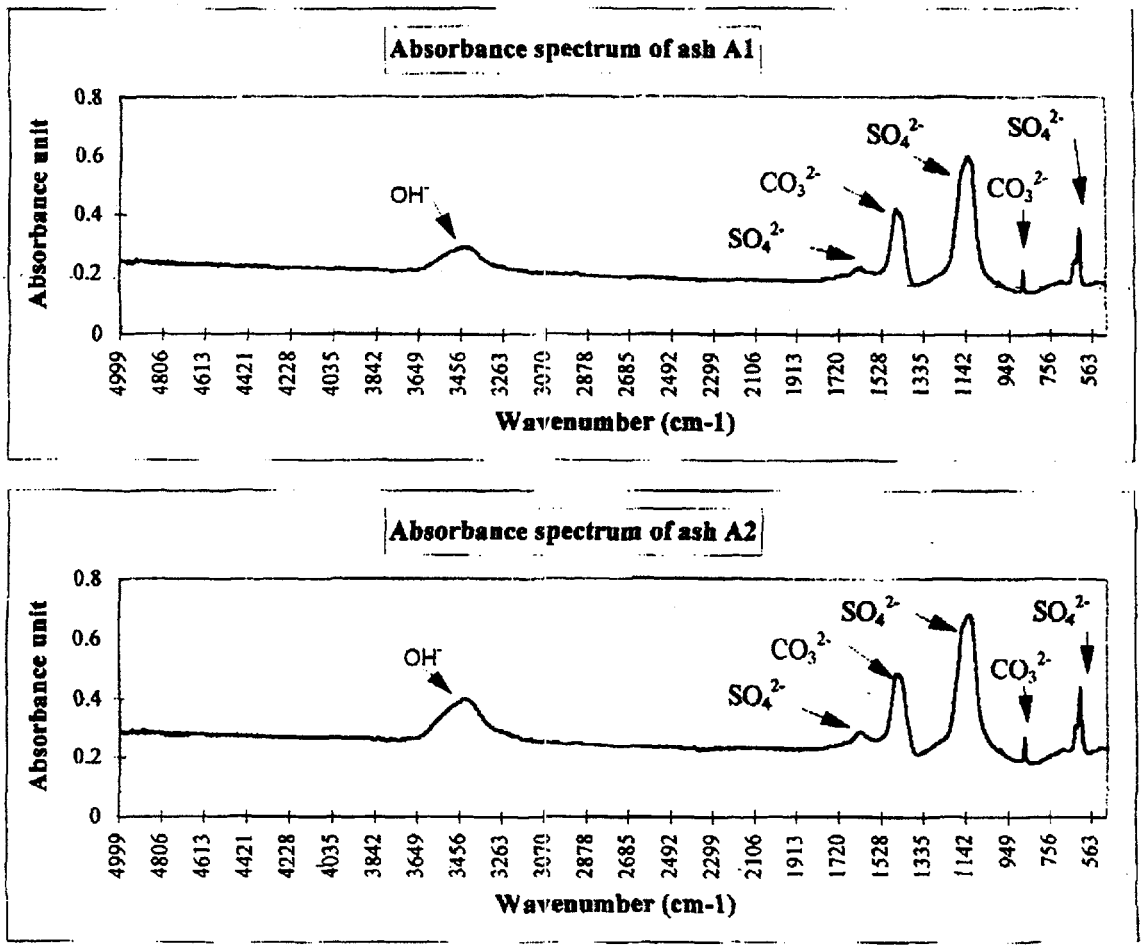

Figure 7. The Abosrbance of Ash A1 and A2

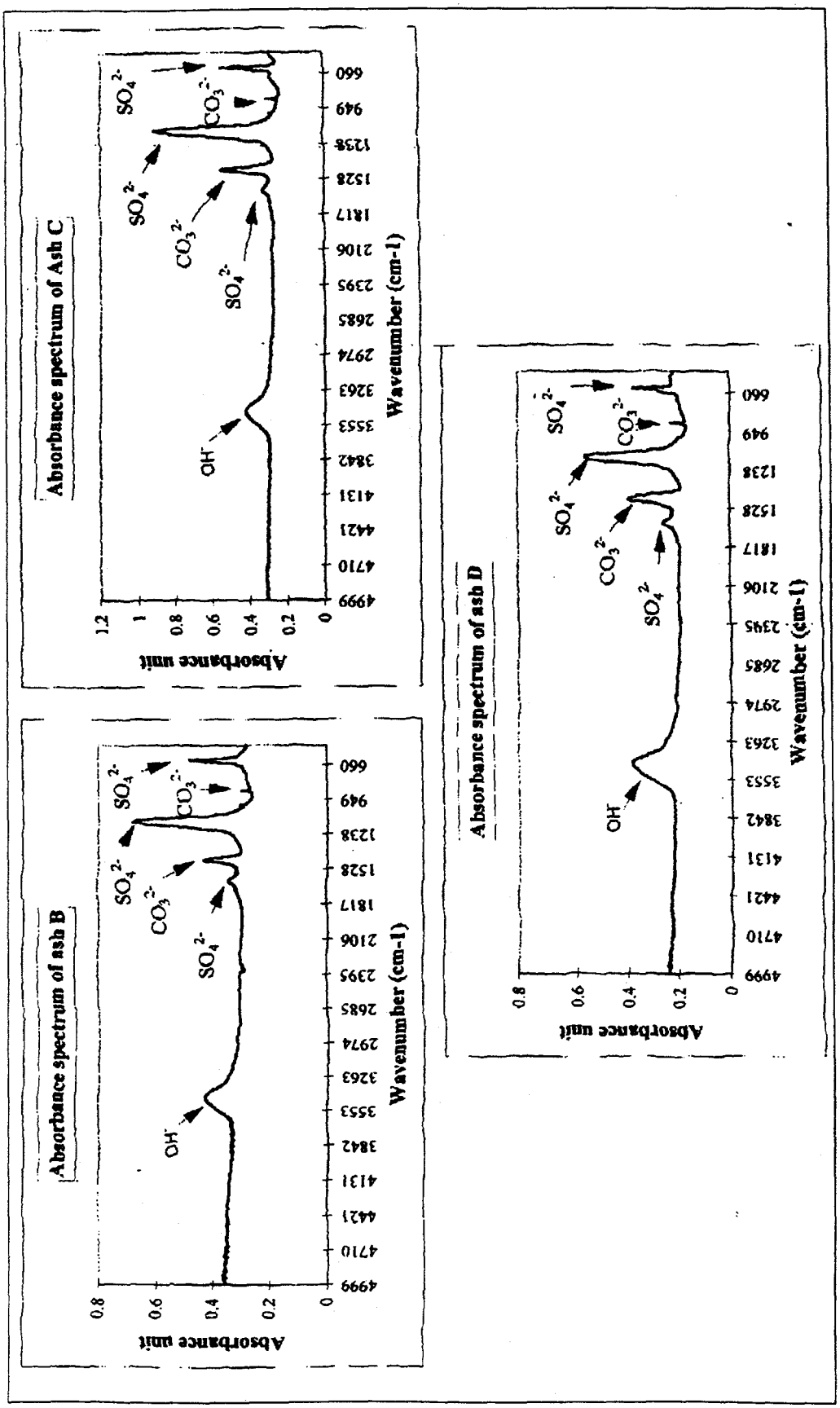

Figure 8. The Absorbance of Ash B,C, and D

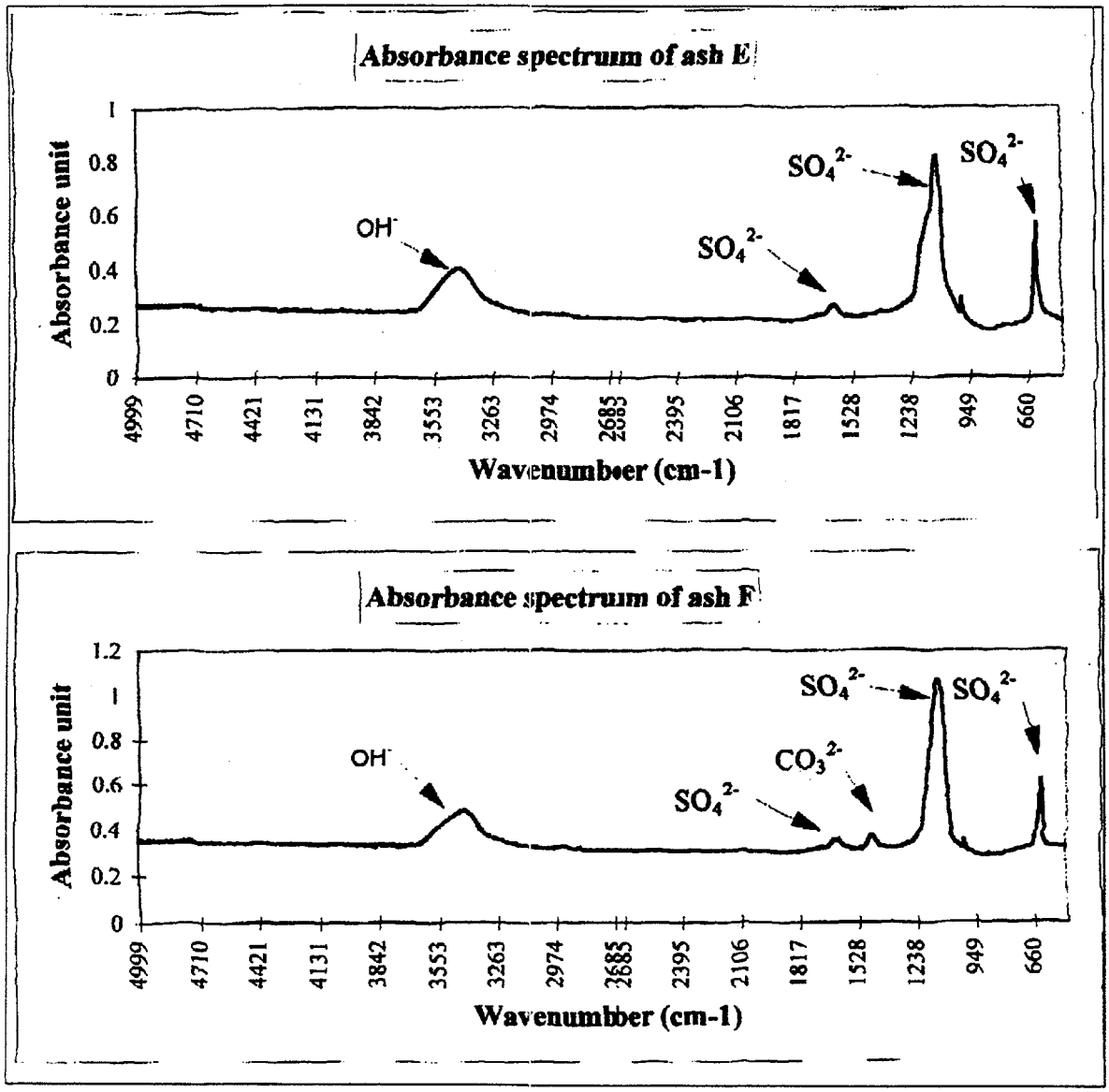

Figure 9. The Absorbance of ash E and F

provided. These include the density of the sample, the acceptance angle of the detector, and variables n_0 and D (diameter). The final window shows the graph of the predicted n and k value and a comparison between the experimental and predicted absorbance. The features of the simulation program are shown in Addendum B of this appendix. The absorption spectra of each sample, obtained by Fourier transform spectroscopy, was converted into a Lab View format file in order to be used with the simulation program. The program subtracts the absorbance spectra of pure KBr, which accounts for the scattering effect by KBr itself, and the corrected experimental spectrum is then compared with the predicted absorbance spectrum. After having filled in the appropriate input, the values of n_0 (a constant) and a particle diameter D (estimated from the SEM photographs), with $k(\nu) = 0$, are varied to match the predicted absorbance spectrum with general shape of the measured absorbance at high wave numbers (mostly above 1500 cm^{-1}). Once the optimal values of n_0 and particle diameter were obtained, $k(\nu)$ was calculated from equation (1). The Kramers-Kronig relation was employed to determine the correction $dn(\nu)$ to n_0, which gave a first approximation of $n(\nu)$. The precision in the values of $n(\nu)$ and $k(\nu)$ may be increased by increasing the number of iterations of this procedure. The experimental absorbance and the predicted absorbance versus wavelength should almost perfectly overlay when the optimal values of $k(\nu)$ and $n(\nu)$ are obtained. Details of the calculations are provided in Addendum A of this appendix.

As discussed in the Experimental Procedure section, the variables n_0 and D need to be estimated in order to get a perfect fit between the experimental and predicted absorbance in determining k, absorption index value. The particle diameter, which has an impact on the shape of the absorbance versus frequency, can be obtained from the average diameter of particle size from SEM pictures. On the other side, the n_0 value, which is constant at high wave number (>2000cm^{-1}) as discussed in the previous section, needs to be varied to find the perfect match of the scattering curve at high wave number by calculation of the smooth scattering curve from Mie theory. Once the right value is found, then this value is used to find the correction to the real part of the refractive index, ***dn***, from the Kramers-Kronig relation. The results of possible values of n_0 for pure inorganic salts are summarized in Table 6.

Table 6. n_0 values for pure inorganic alkali salts.

Material	$n_0(1)$	$n_0(2)$	Diameter (microns)	Selected n_0	n from literature[21]
Na_2SO_4	1.456	1.597	2.56	1.456	1.477
Na_2CO_3	1.428	1.626	2.77	1.626	1.535
K_2SO_4	1.460	1.593	2.95	1.460	1.495
K_2CO_3	1.446	1.606	2.73	1.606	1.531

The constant values of n_0 are the real part of the refractive index at high wave numbers (above 1500 cm^{-1}). The difference in index of refraction between the particles and the KBr causes the scattering of incident radiation. Consequently, two values of n_0, $n_0(1)$ and $n_0(2)$, located on either side of n_{KBr}=1.527, can give a similar scattering curve. This uncertainty can be resolved by considering the agreement between the sharp peaks in the predicted and measured absorbance curves. One should be an almost perfect fit, while the other, while being a good approximation, would not be able to fit the data around the large absorption peaks as well. This due to the fact that, around the strong absorption peaks, the extinction curve has a slightly different shape depending on whether n_0 is higher or lower than n_{KBr}.

However, based on the pure inorganic alkali salts, both values of n_0 gave reasonable predictions. (both fitted very well even at large peaks). The values of n_0 are therefore selected based on both the literature value and the fitted curve for each sample.

For K_2SO_4 and Na_2SO_4, the determined values of n_0 were 1.460 and 1.456 respectively. These values give a slightly better agreement between the measured and predicted absorbance curves (considering the high wave number region) and are also close to the literature values. [20]

Values of 1.606 and 1.626 were obtained for K_2CO_3 and Na_2CO_3 by a similar process.

As is evident, there is a difference between the n_0 value measured by the present technique and the literature reported values. This difference can be attributed to the possible influence of scatter, contaminants in the powdery samples, the technique, and the experimental conditions. Moreover, published values of n_0 of pure inorganic salts and recovery boiler ash samples are unavailable because no values have earlier been reported for the optical constants of samples of interest.

In summary, the value of n_0 for pure inorganic alkali salts is in the range between 1.42-1.63. The values of n_0 for K_2SO_4 and Na_2SO_4 are almost the same (near 1.46) as are the values of n_0 for K_2CO_3 and Na_2CO_3 (near 1.6). This means that, for K_2SO_4 and Na_2SO_4, only sulfate anions affect the absorption and scattering mechanisms while the cations, Na^+ and K^+, have no effects. Similarly, only carbonate anions affect the absorption and scattering of K_2CO_3 and Na_2CO_3.

By considering the values of n_0 obtained for the pure inorganic salts, the values of n_0 for the ash samples were selected based in part on their sulfate and carbonate content. The values obtained are included in Table 7.

Table 7. n_0 values of ash samples.

Material	$n_0(1)$	$n_0(2)$	Diameter (microns)	Selected n_0	n_0 from literature.
A1	1.481	1.573	2.70	1.481	-
A2	1.482	1.572	3.00	1.482	-
B	1.488	1.565	1.98	1.488	-
C	1.492	1.561	1.76	1.492	-
D	1.496	1.558	2.18	1.496	-
E	1.462	1.592	1.35	1.462	-
F	1.473	1.581	1.48	1.473	-

As is evident for pure inorganic salts, sulfate and carbonate anions have a real refractive index of approximately 1.46 and 1.61, respectively at high wave numbers. The refractive indices of ash samples are, then, related to the refractive indices of the pure inorganic salts. From Table 1, each sample is high in sulfate content (the major component), while the content of carbonate and chloride vary from ash to ash. Therefore, the values of the real refractive index, n_0, should be affected by the absorption of light or

electromagnetic radiation by these anions, while the cations (Na and K) do not have significant effects as discussed in the last section.

In ashes E and F, the carbonate anion content is negligible. The values of n_0 for these two ashes are, 1.462 and 1.473, close to the n_0 values of both Na_2SO_4 and K_2SO_4.

We note that, at the specific absorption band of carbonate anions, 1550-1350 cm^{-1} (6.45-7.41 microns), there was very little absorption by these ashes (see Figure 4).

Unlike ashes E and F, absorption by carbonate anions was seen clearly in ashes B, C, and D. These ashes contained intermediate levels of carbonates, more than ashes E and F, but less than ashes A1 and A2. Hence, the values of n_0 for ashes B, C and D should still be closed to those of sulfate than of carbonate, but higher than the values for sulfate due to effect of carbonate. The values of n_0 for these three samples were indeed closer to the n_0 values for Na_2SO_4 and K_2SO_4 (1.46) than to those for Na_2CO_3 and K_2CO_3 (1.61-1.63), but they increased with increasing carbonate content.

Ash samples A1 and A2 not only have a high sulfate content (Table 1), but also have the highest carbonate content of any of the ash samples. Consequently, the values of n_0 for ashes A1 and A2 are between the n_0 values of Na_2SO_4 and K_2SO_4 and of Na_2CO_3 and K_2CO_3. They are closer to the n_0 values of Na_2SO_4 and K_2SO_4 due to their higher sulfate content. The n_0 values of ashes A1 and A2 are a bit lower than those of ashes B-D. This may be due to uncertainty in the absorbance spectra and particle diameters.

Since the composition of both ashes A1and A2 are nearly identical, the values of n_0 are found to be almost the same, i.e. 1.481 and 1.482 respectively.

After choosing the appropriate value of n_0, with other parameters held constant, the predicted value of n and *k* were determined by subtracting the smooth scattering curve for these n_0 values, plus the reflection constant,[4] from the experimental absorbance. The result gives, to a first approximation, the real absorption of these ash samples. The Kramers-Kronig relationships was then used to extract the value of *k*. The final values of n and *k* were obtained by an iterative process as was discussed earlier in this section. The value of n and *k* that make the predicted absorbance and experimental absorbance curves most closely match are considered to be the optimal values of n and *k* as shown in Addendum E of this appendix. The examples of value n and *k* versus wave number are shown in Figure 5.

In summary, the real refractive index of recovery boiler ash samples is in the range of 1.46-1.49 at short wavelengths (high wave number, above 2000 cm^{-1}). It decreases as the wavelength is increases to 10 μm. At wavelengths higher than 10 μm, the values of n increase, and they remain constant at wavelength above 20 μm (<500cm^{-1}). The change in n exhibits a dispersion profile associated with the huge absorption peak at 1240-1040 cm^{-1} (8.06-9.61 μm) and significant peak at 650-550 cm^{-1} (15.38-18.18 μm) due to the vibration-rotation transition of sulfate anions. More minor effects form carbonate anions can cause minor peaks around 1550-1350 cm^{-1} (6.45-7.47 μm) and 940-840 cm^{-1} (10.63-11.90 μm).

The values of absorption index, *k*, ranging from 0.001-0.2, give the corresponding value to the polarization mechanisms-vibration and rotation transition of sulfate by the characteristic of the asymmetric stretch vibration of the tetrahedral SO_4^{2-} ion and carbonate by the characteristic out of plane bending mode of CO_3^{2-} ion, d_3h_1 symmetry. There are no absorption peaks below 6 μm (or above 1500

[4] The reflection constant is subtracted in the simulation program.

cm^{-1}) as seen from the value of the imaginary part of refractive index, *k*, that equal zero in the low wavelength (high wave number) region.

Composition dependence of the optical constants

As discussed in the literature review, the sulfate and carbonate contents appear to be the species that determine the optical constants.

As is event from the analysis, the ash samples used in this study have quite low carbonate contents and almost no heavy metals and other trace elements (less than 0.08 wt-% in all cases). All of the carbon present in these ash samples was in the form of carbonate. Therefore, the effects of unburned carbon and heavy metals, which can influence the optical constants[7,9], have no influence on the optical constants of recovery boiler ash. The only effects observed in the present study were the vibration-rotation stretching band of sulfate and carbonate anions that gave rise to the high absorbance peaks in the wavelengths between 6-20 μm.

The effect of other component such as NaCl and KCl seems to be less significant when compared with the sulfate and carbonate anions because of the small amounts present. Moreover, the effect of KCl and NaCl on the effect to the optical constants cannot be determined by the present method because of the transparency of KCl in the infrared region and because NaCl absorbs only at very high wavelengths (above 50 μm) which is out of the range of the FT-IR spectrometer.[19]

Uncertainty in the optical constants (n and k)

Uncertainty in the optical constants (n and k) came from two parameters: the absorbance spectra of pellet in each sample and the particle diameter. The first parameter depends on the amount of sample used in the pellet. The absorbance spectra affects the n_0 values (the real refractive index at high wave numbers) and correspondingly make the values of n and k vary. Based on the uncertainty in the absorbance, the uncertainty in n and k are estimated to be ±0.004 for n and ±0.001 for k. The calculations are included in Addendum F of this appendix.

The particle diameter also affects on the values of n and k. The effect of uncertainty in the particle diameter (range ±0.5 microns) on the optical constants is estimated to be ±0.007 for n, and there is no variation of k values. Calculations of the uncertainty of n and k due to the uncertainty in the particle diameter (±0.5 microns) are shown in Addendum F of this appendix.

We conclude from these results that the uncertainty in the values of n obtained in this work are less than ±0.01[4] . For k, the uncertainty is ±0.001.

Sources of error

Uncertainty in the experimental results may have been caused by several factors, not only in the experiments but also in the preparation of materials. The sources of error may be identified as follow:

In the preparation of materials, because the ash samples are light, fluffy and always agglomerate together, preparation of the ash samples is very difficult. The density and particle size of the ash samples are the most important parameters in calculating the optical constants. The apparent density of the ash samples must be known in order to monitor the amount of samples placed in the KBr pellet to avoid multiple-scattering problems. The densities of the ash samples were determined by a standard procedure,

[4] This value is rounded up from the square root of the summation of the second power of 0.004 and 0.007.

the volume displacement method. Owing to the characteristics of the ash samples, this method was conducted by using glycerin as a fluid suspension because the alkali salts are not soluble in it. A significant error could have occurred if large amounts of samples were used. The large void volume between high amount of sample, including some air and other impurities, may create problems in finding accurate density values.

In order to apply the Mie theory, the particles must be homogeneous. Particle sizes must also be small (<10 microns) so that they absorb well. Grinding of samples depends on the characteristics of the samples, their composition, morphology, and the time for grinding. There is no way to control accurately the size of particles at this size range. SEM photographs are used to determine the average particle size. The uncertainty of the mean particle size may lead to errors owing to the presence of some large particles. If there are high distributions between large and small particles in the pellet, the absorption by these particles may inaccurate due mainly to non-homogeneity.

On the other hand, in the experimental sections, the KBr pellet used in this study should be transparent because KBr is non-absorbing. Care must be taken to eliminate the formation of microcracks in the KBr during the few minutes following the pressing of the pellet. When these microcracks occur, they make the pellets turn from transparent to whitish. These microcracks contribute to scattering, and are probably related to water escaping the pellet and stress in the KBr. Whitish pellets can give unreasonable absorbance spectra and lead to significant error in determining the optical constants.

The absorbance spectra of samples are obtained by the Fourier Transform spectrometer. The amplitude of the absorbance must be considered carefully to avoid either saturation from too much absorption or noise effects from too little absorption. Either would cause some disturbances to the absorption peaks of the samples. The amount of ash in the KBr pellets must be controlled carefully to prevent these effects. Moreover, multiple-scattering effects, which occur when high amounts of ash sample are present in the pellet, can lead to overlap of absorption bands in absorption regions. This makes the identification of each individual peak difficult because of poor separation.

The choice of n_0, the real part of refractive index at high wave number, has also been a cause of error. Value of n_0 on the either side of $n_{KBr} = 1.527$ can give a similar scattering curve. The chosen value of n_0 must be carefully considered by taking into account the n_0 values of the pure inorganic salts. Unfortunately, no data of the optical constants of pure salts or high alkali salts-containing ashes are available because no previous studies employing this technique have been reported.

Conclusions

The results of an experimental study of the optical constants of ash obtained from the electrostatic precipitators of six different kraft recovery boilers have been presented. From the results of this study, we draw the following conclusions:

1. The technique employed for the first time in this study is simpler than other reported techniques that acquire more complex measurements and computations. However, it provides results that are in agreement with the limited data available on the optical properties of sodium and potassium sulfates and carbonates.

2. The bulk densities of the ash samples were in the range between 0.2-0.5 g/cm^3. The chemical composition of the samples used in this study were found to correspond to the typical composition of ash deposits in the upper part of recovery boilers as reported by Adams et al., [1] 1997.

3. The majority of particles produced by grinding the ash and ash component samples were in the range between 0.5-5 microns. Larger particles were also found. Their effects on the optical properties was small, however, because of the small number of these larger particles compared with the huge number of smaller particles. However, there was virtually no control over what the particle size was in the pellet due largely to the tendency of these light, fluffy, particles to agglomerate. The mean particle size of the ash samples was in the range 1.0-3.0 microns, and 2.0-3.0 microns for pure inorganic alkali salts. This seemed to make the analysis more accurate and easier, as discussed in regards to the grinding step in the experimental procedure.

4. The absorbance spectra of the kraft recovery boilers ash samples show specific absorption bands of sulfate and carbonate anions, the two largest components in the ash samples. Cations (Na versus K) had no significant effect in the position of intensity of the absorption bands. The sulfate anions show specific bands at 1240-1040 cm^{-1} (8.06-9.62 μm), 650-550 cm^{-1} (15.38-18.18 μm) and 1700-1500 cm^{-1} (5.88-6.45 μm). In region 1550-1350 cm^{-1} (6.45-7.41 μm), 940-840 cm^{-1} (10.63-11.9 μm) and 750-650 cm^{-1} (13.3-15.38 μm) are the specific bands for the carbonate anions. The magnitude of the absorbance is related to the strength of each specific absorption band. That, in turn, is related to the amount of the component in the ash sample. The larger the amount of a specific component, the higher the magnitude of the absorbance.

5. The optical constants of ash samples have been affected by the mixing composition between the sulfate and carbonate anions. The values of the real index, n, are constant above the absorption region (>2000 cm^{-1}), called n_0, and are varied from one sample to another. The choice of n_0 is assumed to depend on the composition of the ash. The value of n_0 varied from 1.46-1.49. The changes in n exhibit a dispersion profile that is determined by how the radiation wave propagate into medium associated with absorption peaks of material in the samples.

6. The values of the absorption index, *k*, ranging from 0.001-0.2, are those of a weakly absorbing material. They correspond to the polarization mechanisms of vibration and rotation transition of sulfate by the characteristic of the asymmetric stretch vibration of the tetrahedral SO_4^{2-} ions and carbonate by the characteristic out-of-plane bending mode of CO_3^{2-} ions. The extremely low absorption of these particles over the infrared spectrum shows that these suspended particles (fume) do not significantly absorb or emit radiation. The effect of these particles on radiant heat transfer, other than scattering, in recovery boilers is negligible.

7. The iron, silica and carbon content of the recovery boiler ashes were negligible. These elements had no impact on the optical properties of the recovery boiler ashes.

8. The values of n and *k* obtained can be used in calculating radiant heat transfer in kraft recovery boiler when these particles are suspended in the combustion gases.

Summary

The accurate determination of the optical constants of a material is a difficult task. It requires not only accurate measurement of radiant energy transmission and absorption, but also well-characterized samples.

The KBr extinction technique, along with Mie Theory, was employed to obtain the unique optical properties of ash samples from Kraft recovery boiler, the property measured was the refractive index in the thermal radiation region. Mie theory, which separated scattering effects from absorption effects, was examined to obtain the real absorption curve of the particles. It was assumed that a homogeneous, single spherical particle in a densely packed system acts, to a first approximation,

independently in the absorption and scattering of radiation, unaffected by the presence of other particles. The energy absorbed by a system of particle is thus the algebraic sum of the energy absorbed by each particle.

To ensure that this assumption was valid, the amounts of samples used in the pellets have to be monitored by considering the relationship between the amount and density of each sample and the absorbance of the resulting KBr/sample pellet. The absorption index is then determined by the alternative Kramers-Kronig relationship, in time domain and using the fast Fourier transform method.

Accurate optical constants are obtained by an iterative process of fitting the optical properties model to the measured absorption-transmission data.

The mass of particles (related to the number of particles) in each pellet must be carefully controlled to insure that multiple scattering does not occur. The homogeneous particle assumption of Mie theory, is then still valid. Typically, for materials of high density, the sample mass has to be large to have a sufficient number of particles (high enough scattering in order to make the separation between absorption and scattering more easily). However, for weakly or moderate absorbing kraft recovery boiler ash samples, like ash samples, to mix with 300 mg of KBr, 0.4 mg of sample was found to be enough to have a clearly measurable absorbance without approaching saturation of the absorbance spectrum.

For materials such as pure inorganic alkali salts, which had a higher density, a sample of 1.0 mg is the upper limit to have a measurable absorbance, as well as to ensure that scatter is minimized.

REFERENCES

1). A. Ashkin., *"Acceleration and Trapping of Particles by Radiation Pressure"*, Physics Review Letters, Vol.24, pp.1 5& 159, 1970.

2). G.W. Grams, I.W. Blifford, D.A. Gillette, and P.B Russell., *"Complex Index of Refraction of Airborne Soil Particles"*, Journal of Applied Meteorology, Vol.13, pp.459-471, 1974.

3). C. Willis., *"The complex Refractive Index of Particles in a Flow", Journal of* Physics D: Applied Physics, Vol.3, pp.1944-1956, 1970.

4). D.M. Roessler and F.R. Faxvog., *"Optoaccoustic Measurement of Optical Absorption in Acetylene Smoke"*, Journal of Optical Society America, Vol.69, pp.1699, 1979.

5). F. Volz'., "Infrared Optical Constants of Ammonium Sulfate, Sahara Dust, Volcanic Pumics, Anf Fly ash", Applied Optics, Vol.12, pp.564-56, 1973.

6). P.R. Solomon, R.M. Carangelo, P.E. Best, J.R. Markham and D.G. Hamblen., "The Spectral Emittance of Pulverized Coal and Char", Twenty-first Symposium (International) on combustion[The combustion Institute, pp.437446, 1986.

7). D.G. Goodwin and M. Mitchner., *"Infrared Optical Constants of Coal Slags: Dependence on Chemical Composition"*, Journal of Thermophysics, Vol.3, No.1, pp.53-60, January, 1989.

8). P.J. Foster and C.R. Howarth., *"Optical Constants of Carbons and Coals in the Infrared"*, Carbon, Vol.6, pp.719-729, 1968.

9). M.Q. Brewster and T. Kunitomo., *"The Optical Constants of Coal, Char, and Limestone"*, Journal of Heat Transfer, Vol.106, pp.678-683, 1984.

11). J.R. Markham, P.R. Solomon, and P.E. Best, *"An FT-IR based Instrument for Measuring Spectral Emittance of Material at High Temperature"*, American Institute of Physics, Vol.61, No.12, pp.3700-3708, December, 1990.

12).J.R. Markham, P.R. Solomon, P.E. Best and Z.Z. Yu., *"Measurement of Radiative Properties of Ash and Slag by FT4R Emission and Reflection Spectroscopy"*, Journal of Heat Transfer, Vol.114, No.12, pp.458-464, May, 1992.

13). C.W. Peterson and B.W. Knight., *"Causality calculations in the time domain: An efficient alternative to the Kramers-Kronig method"*, Journal of The Optical Society of America, Vol.63, No.10, pp.1238-1242, October, 1973.

14). *R.P* Gupta and T.F Wall., *"The optical Properties of flyash in Coal fired Furnaces"*, Combustion and Flame, Vol.61, ppl4S-151,1985.

15). A. Lowe, I. McC. Stewart, and T.F Wall., *'The measureinent and Interpretation of Radiation from flyash particles in large pulverized coal flames"*, Seventeenth Symposium (International) on Combustion, The Combustion Institute, Pittsburgh, PA., pp.105-112, 1979.

16). C.F. Bohren and D.R. Huffnian., *"Absorption and Scattering ofLight by Small Particles"*, John Wiley & Sons, 1983.

17). C.L. Tien and B.L. Drolen., *"Thermal Radiation in Particulate Media with Dependent and Independent Scattering"*, Annual Review of Numerical Fluid Mechanics and Heat Transfer, Vol.1, pp.1-32, 1987.

18). T.N. Adams, W.J. Frederick, T.M. Grace, M. Hupa, K. Iisa, A.K. Jones, and H.N. Tran., *"Kraft Recovery Boilers"*, TAPPI Press, Atlanta, 1997.

19). R.A. Nyquist and R.O. Kagel., "Infrared Spectra of In organic Compounds (3800-45 cm^{-1})", Academic Press, 1971.

20). R.H. Perry and D. Green., *"Perry's Chemical Engineerings' Handbook", Mc* Graw Hill, Sixth Edition, 1984.

21). Samretvanich, A., "Determination of the Optical Constants of Ash Samples from Kraft Recovery Boilers," M.S. Thesis, Oregon State University (1997).

List of Addenda

ADDENDUM A

The Calculation Procedure

Development of the scattering model (Mie theory)

In order to simplify the Mie theory, the assumption of the homogeneous slab model was conducted as:

The irradiance or intensity is attenuated according to

$$I_t = I_0 \exp(-\alpha_{ext} h) \qquad \text{----- (1)}$$

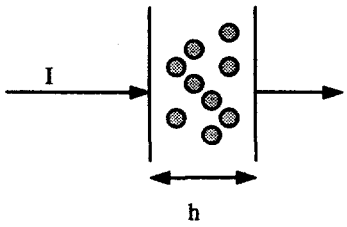

The incident beam traverses the slab of particles where

I_t = intensity of radiation transmitted through the sample at a given wave number

I_0= intensity of transmitted radiation with no samples

h= thickness of slab

α_{ext} = attenuation coefficient $= \eta C_{ext} = \eta C_{abs} + \eta C_{sca}$ or $\alpha_{ext} = \sum_j \eta C_{ext\,j}$

η = number of particles per unit volume

C_{ext} = extinction cross section

C_{sca} = scattering cross section

C_{abs} = absorption cross section

$\alpha = 4\pi k/\lambda$, k = absorption index

The size parameter was defined as $x = ka = 2\pi Na/\lambda = 2\pi Nv$ ----- (2)

where N = medium refractive index

a = particle radius

k = wave vector

From FT-IR spectrometer, the absorbance spectra were obtained.

$$\text{Absorbance} = A_\nu = \log_{10}\frac{I_0}{I_t}$$

$$\text{Transmittance} = \tau_\nu = \frac{I_{t\nu}}{I_{0\nu}}$$

$$\therefore \quad A_\nu = \log_{10}\frac{100}{\%T}$$

$$\frac{I_t}{I_0} = \exp(-\alpha_{ext}\, h)$$

$$\frac{I_0}{I_t} = \exp(\alpha_{ext}\, h)$$

$$\log_{10}\frac{I_0}{I_t} = \alpha_{ext}\frac{h}{\ln 10} = A_\nu = \text{Absorbance}$$

$$\left[\ \log_{10} x = \frac{\ln x}{\ln 10}\ \right]$$

$$\therefore\ A_\nu = \frac{h}{\ln 10}\eta C_{ext} = \eta Q_{ext}\pi a^2\frac{h}{\ln 10}$$

where $Q_{ext} = C_{ext}/\pi a^2$

Q_{ext} = extinction efficiency, can be calculated from the Mie program

a = radius of particle

η = number of particles per unit volume

$$\therefore \quad A_\nu = -\log_{10}\tau_\nu \quad \text{where} \quad \tau_\nu = \exp(-\eta A F_\nu^t h)$$

$$A_\nu = \frac{\eta A F_\nu^t h}{2.3026} \qquad \text{----- (3)}$$

where $F_\nu^t = Q_{ext\,\nu}$ for forward direction (including effect of acceptance angle)

A = cross section $= \pi R^2$

$\eta = N/V_{pellet}$ where N = number of particles in pellet

$$= \frac{\text{weight(ash)}}{\text{weight(1particle)}} = \frac{w}{\frac{4}{3}\pi R^3\rho}$$

$$\eta = \frac{w}{\frac{4}{3}\pi R^3 \rho} \cdot \frac{1}{A_{pellet} \times h} \qquad , A = \pi R^2$$

From (3) $$A_\nu = \frac{w}{\frac{4}{3}\pi R^3 \rho} \cdot \frac{1}{A_{pellet} \times h} \cdot \frac{A_{pellet} \times F^t_\nu h}{\ln 10}$$

$$A_\nu = \frac{3}{4}\frac{w}{\rho} \cdot \frac{1}{A_{pellet}} \cdot \frac{1}{\ln 10} \cdot \frac{F^t_\nu}{R} \qquad \text{----- (4)}$$

where ρ = density of sample

R = radius of particles

To get *k*, from $A_\nu = \alpha t$

$\alpha = A_\nu / t$

t = thickness of ash particle presented in slab

$$= \frac{V_{ash}}{A_{pellet}} = \frac{\text{weight(ash)}}{\rho} \times \frac{1}{A_{pellet}} = \frac{w}{\rho} \cdot \frac{1}{A_{pellet}}$$

From (4), $$\frac{A_\nu}{t} = \frac{3}{4} \cdot \frac{w}{\rho} \cdot \frac{1}{A_{pellet}} \cdot \frac{1}{\ln 10} \frac{F^t_\nu}{R} \cdot \frac{\rho}{w} \cdot A_{pellet}$$

and $$\alpha = \frac{4\pi k}{\lambda}$$

$$\therefore \frac{4\pi k}{\lambda} = \frac{3}{4} \cdot \frac{w}{\rho} \cdot \frac{1}{A_{pellet}} \cdot \frac{1}{\ln 10} \frac{F^t_\nu}{R} \cdot \frac{\rho}{w} \cdot A_{pellet}$$

$$\therefore \quad k = \frac{3}{4} \cdot \frac{F^t_\nu}{R} \cdot \frac{\lambda}{4\pi} \qquad \text{----- (5)}$$

$F^t_\nu = Q_{ext\,\nu}$ from the Mie calculation program

$$Q_{ext} = \frac{C_{ext}}{\pi a^2}$$

$$C_{ext} = \frac{4\pi}{k^2} \mathrm{Re}\{S(0^0)\} \qquad \text{----- (6)}$$

where $S(0^0)$ = amplitude scattering at forward direction or S specifies the magnitude and direction of the rate of transfer of electromagnetic energy at any points of space.

$$C_{sca} = \frac{2\pi}{k^2} \sum_{n=1}^{\infty} (2n+1)\left(|a_n|^2 + |b_n|^2\right) \qquad \text{----- (7)}$$

$$C_{ext} = \frac{2\pi}{k^2} \sum_{n=1}^{\infty} (2n+1)\mathrm{Re}\{a_n + b_n\} \qquad \text{----- (8)}$$

where a_n and b_n are the coefficient and defined as

$$a_n = \frac{m\psi_n(mx)\psi_n'(x) - \psi_n(x)\psi_n'(mx)}{m\psi_n(mx)\xi_n'(x) - \xi_n(x)\psi_n'(mx)} \qquad \text{----- (9)}$$

$$b_n = \frac{\psi_n(mx)\psi_n'(x) - m\psi_n(x)\psi_n'(mx)}{\psi_n(mx)\xi_n'(x) - m\xi_n(x)\psi_n'(mx)} \qquad \text{----- (10)}$$

where ψ_n = Riccati-Bessel functions, $\psi_n(\rho) = \rho j_n(\rho)$ and $\xi_n(\rho) = \rho h_n^{(1)}(\rho)$

$m = k_1/k_2 = N_1/N$ = refractive index of particle / refractive index of medium

k = wave vector

$$Q_b = \frac{\sigma_b}{\pi a^2} = \frac{1}{x^2}\left|\sum_n (2n+1)(-1)^n\left(a_n - b_n\right)\right|^2 \qquad \text{----- (11)}$$

x = vector scattering amplitude for the particle

σ_b= backscattering cross section

Q_b = efficiency for backscattering

By equipping equation (6) through (11), the Q_{sca}, Q_{back}, Q_{ext} and scattering amplitude at acceptance at detector angle are calculated. In order to simplify the complicate equations, the software program was provided by Bohren and Huffman, 1983.

The absorption index was calculated by inserting the Q_{ext} values from Mie's program in equation (5). In Mie program, several input parameters need to be added such as refractive index of media, real and imaginary part of refractive index, n and *k*, sphere radius, wavelength and size parameters.

The simulation program provided by Advance Fuel Research was employed to make the calculation of the optical constants from these equations faster and easier. This simulation program is included in Addendum B.

Addendum B

The Computation Program

```
      1         PROGRAM CALLBH (INPUT=TTY,OUTPUT=TTY,TAPE5=TTY)
C     ************************************************************
C     CALLBH CALCULATES THE SIZE PARAMETER (X) AND RELATIVE
C     REFRACTIVE INDEX (REFREL) FOR A GIVEN SPHERE REFRACTIVE INDEX,
C     MEDIUM REFRACTIVE INDEX , RADIUS , AND FREE SPACE WAVELENGTH.
C     IT THEN CALLS BHMIE, THE SUBROUTINE THAT COMPUTES AMPLITUDE
C     SCATTERING MATRIX ELEMENTS AND EFFICIENCIES
C     ************************************************************
      COMPLEX REFREL,S1(200),S2(200)
      WRITE (5,11)
C     ******************************************************
C     REFMED = (REAL)  REFRACTIVE INDEX OF SURROUNDING MEDIUM
C     ******************************************************
      REFMED=1.0
C     ****************************************
C     REFRACTIVE INDEX OF SPHERE = REFRE +I*REFIM
C     ****************************************
      REFRE=1.55
      REFIM=0.0
      REFREL=CMPLX(REFRE,REFIM)/REFMED
      WRITE (5,12) REFMED,REFRE,REFIM
C     **********************************
C     RADIUS (RAD) AND WAVELENGTH (WAVEL) SAME UNITS
C     **********************************
      RAD=.525
      WAVEL=.6328
      X=2.*3.14159265*RAD*REFMED/WAVEL
      WRITE (5,13) RAD,WAVEL
      WRITE (5,14) X
C     ************************************************
C     NANG = NUMBER OF ANGLES BETWEEN 0 AND 90 DEGREES
C     MATRIX ELEMENTS CALCULATED AT 2*NANG - 1 ANGLES
C     INCLUDING 0, 90, AND 180 DEFRESS
C     ************************************************
      NANG=11
      DANG=1.570796327/FLOAT(NANG-1)
      CALL BHMIE(X,REFREL,NANG,S1,S2,QEXT,QSCA,QBACK)
      WRITE (5,65) QSCA,QEXT,QBACK
      WRITE (5,17)
C     ********************************************************
C     S33 AND S34 MATRIX ELEMENTS NORMALIZED BY S11.
C     S11 IS NORMALIZED TO 1.0 IN THE FORWARD DIRECTION
C     POL=DEGREE OF POLARIZATION (INCIDENT UNPOLARIZED LIGHT)
C     ********************************************************
      S11NOR=0.5*(CABS(S2(1))**2+CABS(S1(1))**2)
      NAN=2*NANG-1
      DO 335 J=1,NAN
      AJ=J
      S11=0.5*CABS(S2(J))*CABS(S2(J))
      S11=S11+0.5*CABS(S1(J))*CABS(S1(J))
      S12=0.5*CABS(S2(J))*CABS(S2(J))
      S12=S12-0.5*CABS(S1(J))*CABS(S1(J))
      POL=-S12/S11
      S33=REAL(S2(J)*CONJG(S1(J)))
      S33=S33/S11
      S34=AIMAG(S2(J)*CONJG(S1(J)))
      S34=S34/S11
```

```
58          S11=S11/S11NOR
59          ANG=DANG*(AJ-1.)*57.2958
60      355 WRITE (5,75) ANG,S11,POL,S33,S34
61      65  FORMAT (//,1ZX,"QSCA= ",E13.6,3X,"QEXT = ",E13.6,3X,
62         2"QBACK = ",E13.6)
63      75  FORMAT (1X,F6.2,2X,E13.6,2X,E13.6,2X,E13.6,2X,E13.6)
64      11  FORMAT (/"SPHERE SCATTERING PROGRAM"//)
65      12  FORMAT (5X,"REFMED = ",F8.4,3X,"REFRE =",E14.6,3X,
66         3"REFIM = ",E14.6)
67      13  FORMAT (5X,"SPHERE RADIUS = ",F7.3,3X,"WAVELENGTH = ",F7.4)
68      14  FORMAT (5X,"SIZE PARAMETER =",F8.3/)
69      17  FORMAT (//,2X,"ANGLE",7X,"S11",13X,"POL",13X,"S33",13X,"S34"//)
70          STOP
71          END
72  C         ************************************************************
73  C         SUBROUTINE BHMIE CALCULATES AMPLITUDE SCATTERING MATRIX
74  C         ELEMENTS AND EFFICIENCIES FOR EXTINCTION, TOTAL SCATTERING
75  C         AND BACKSCATTERING FOR A GIVEN SIZE PARAMETER AND
76  C         RELATIVE REFRACTIVE INDEX
77  C         ************************************************************
78          SUBROUTINE BHMIE (X,REFREL,NANG,S1,S2,QEXT,QSCA,QBACK)
79          DIMENSION AMU(100),THETA(100),PI(100),TAU(100),PI0(100),PI1(100)
80          COMPLEX D(3000),Y,REFREL,,XI,XI0,XI1,AN,BN,S1(200),S2(200)
81          DOUBLE PRECISION PSI0,PSI1,PSI,DN,DX
82          DX=X
83          Y=X*REFREL
84  C         ***********************************
85  C         SERIES TERMINATED AFTER NSTOP TERMS
86  C         ***********************************
87          XSTOP=X+4.*X**.3333+2.0
88          NSTOP=XSTOP
89          YMOD=CABS(Y)
90          NMX=AMAX1(XSTOP,YMOD)+15
91          DANG=1.570796327/FLOAT(NANG-1)
92          DO 555 J=1,NANG
93          THETA(J)=(FLOAT(J)-1.)*DANG
94      555 AMU(J)=COS(THETA(J))
95  C         **************************************************
96  C         LOGARITHMIC DERIVATIVE D(J) CALCULATED BY DOWNWARD
97  C         RECURRENCE BEGINNING WITH INITIAL VALUE 0.0 + I*0.0
98  C         AT J= NMX
99  C         **************************************************
100         D(NMX)=CMPLX(0.0,0.0)
101         NN=NMX-1
102         DO 120 N=1,NN
103         RN=NMX-N+1
104     120 D(NMX-N)=(RN/Y)-(1./(D(NMX-N+1)+RN/Y))
105         DO 666 J=1,NANG
106         PI0(J)=0.0
107     666 PI1(J)=1.0
108         NN=2*NANG-1
109         DO 777 J=1,NN
110         S1(J)=CMPLX(0.0,0.0)
111     777 S2(J)=CMPLX(0.0,0.0)
112 C         *****************************************
113 C         RICCATI-BESSEL FINCTIONS WITH REAL ARGUMENT X
114 C         CALCULATED BY UPWARD RECURRENCE
```

```
C       ********************************************
      PSI0=DCOS(DX)
      PSI1=DSIN(DX)
      CHI0=-SIN(X)
      CHI1=COS(X)
      APSI0=PSI0
      APSI1=PSI1
      XI0=CMPLX(APSI0,-CHI0)
      XI1=CMPLX(APSI1,-CHI1)
      QSCA=0.0
      N=1
  200 DN=N
      RN=N
      FN=(2.*RN+1.)/(RN*(RN+1.))
      PSI=(2.*DN-1.)*PSI1/DX-PSI0
      APSI=PSI
      CHI=(2.*RN-1.)*CHI1/X - CHI0
      XI=CMPLX(APSI,-CHI)
      AN=(D(N)/REFREL+RN/X)*APSI - APSI1
      AN=AN/((D(N)/REFREL+RN/X)*XI-XI1)
      BN=(REFREL*D(N)+RN/X)*APSI -APSI1
      BN=BN/((REFREL*D(N)+RN/X)*XI - XI1)
      QSCA=QSCA+(2.*RN+1.)*(CABS(AN)+CABS(BN)*CABS(BN))
      DO 789 J=1,NANG
      JJ=2*NANG-J
      PI(J)=PI1(J)
      TAU(J)=RN*AMU(J)*PI(J) - (RN+1.)*PI0(J)
      P=(-1.)**(N-1)
      S1(J)=S1(J)+FN*(AN*PI(J)+BN*TAU(J))
      T=(-1.)**N
      S2(J)=S2(J)+FN*(AN*TAU(J)+BN*PI(J))
      IF(J.EQ.JJ)GO TO 789
      S1(JJ)=S1(JJ) + FN*(AN*PI(J)*P+BN*TAU(J)*T)
      S2(JJ)=S2(JJ)+FN*(AN*TAU(J)*T+BN*PI(J)*P)
  789 CONTINUE
      PSI0=PSI1
      PSI1=PSI
      APSI1=PSI1
      CHI0=CHI1
      CHI1=CHI
      XI1=CMPLX(APSI1,-CHI1)
      N=N+1
      RN=N
      DO 999 J=1,NANG
      PI1(J)=((2.*RN-1.)/(RN-1))*AMU(J)*PI(J)
      PI1(J)=PI1(J)-RN*PI0(J)/(RN-1.)
  999 PI0(J)=PI(J)
      IF (N-1-NSTOP) 200,300,300
  300 QSCA=(2./(X*X))*QSCA
      QEXT=(4./(X*X))*REAL(S1(1))
      QBACK=(4./(X*X))*CABS(S1(2*NANG-1))*CABS(S1(2*NANG-1))
      RETURN
      END
```

```
      1          PROGRAM CALLBH (INPUT=TTY,OUTPUT=TTY,TAPE5=TTY)
C     ************************************************************
C     CALLBH CALCULATES THE SIZE PARAMETER (X) AND RELATIVE
C     REFRACTIVE INDEX (REFREL) FOR A GIVEN SPHERE REFRACTIVE INDEX,
C     MEDIUM REFRACTIVE INDEX , RADIUS , AND FREE SPACE WAVELENGTH.
C     IT THEN CALLS BHMIE, THE SUBROUTINE THAT COMPUTES AMPLITUDE
C     SCATTERING MATRIX ELEMENTS AND EFFICIENCIES
C     ************************************************************
      COMPLEX REFREL,S1(200),S2(200)
      WRITE (5,11)
C     *******************************************************
C     REFMED = (REAL)  REFRACTIVE INDEX OF SURROUNDING MEDIUM
C     *******************************************************
      REFMED=1.0
C     ****************************************
C     REFRACTIVE INDEX OF SPHERE = REFRE +I*REFIM
C     ****************************************
      REFRE=1.55
      REFIM=0.0
      REFREL=CMPLX(REFRE,REFIM)/REFMED
      WRITE (5,12) REFMED,REFRE,REFIM
C     *********************************
C     RADIUS (RAD) AND WAVELENGTH (WAVEL) SAME UNITS
C     *********************************
      RAD=.525
      WAVEL=.6328
      X=2.*3.14159265*RAD*REFMED/WAVEL
      WRITE (5,13) RAD,WAVEL
      WRITE (5,14) X
C     ***************************************************
C     NANG = NUMBER OF ANGLES BETWEEN 0 AND 90 DEGREES
C     MATRIX ELEMENTS CALCULATED AT 2*NANG - 1 ANGLES
C     INCLUDING 0, 90, AND 180 DEFRESS
C     ***************************************************
      NANG=11
      DANG=1.570796327/FLOAT(NANG-1)
      CALL BHMIE(X,REFREL,NANG,S1,S2,QEXT,QSCA,QBACK)
      WRITE (5,65) QSCA,QEXT,QBACK
      WRITE (5,17)
C     ***********************************************************
C     S33 AND S34 MATRIX ELEMENTS NORMALIZED BY S11.
C     S11 IS NORMALIZED TO 1.0 IN THE FORWARD DIRECTION
C     POL=DEGREE OF POLARIZATION (INCIDENT UNPOLARIZED LIGHT)
C     ***********************************************************
      S11NOR=0.5*(CABS(S2(1))**2+CABS(S1(1))**2)
      NAN=2*NANG-1
      DO 335 J=1,NAN
      AJ=J
      S11=0.5*CABS(S2(J))*CABS(S2(J))
      S11=S11+0.5*CABS(S1(J))*CABS(S1(J))
      S12=0.5*CABS(S2(J))*CABS(S2(J))
      S12=S12-0.5*CABS(S1(J))*CABS(S1(J))
      POL=-S12/S11
      S33=REAL(S2(J)*CONJG(S1(J)))
      S33=S33/S11
      S34=AIMAG(S2(J)*CONJG(S1(J)))
      S34=S34/S11
```

```
      S11=S11/S11NOR
      ANG=DANG*(AJ-1.)*57.2958
  355 WRITE (5,75) ANG,S11,POL,S33,S34
   65 FORMAT (//,1ZX,"QSCA= ",E13.6,3X,"QEXT = ",E13.6,3X,
     2"QBACK = ",E13.6)
   75 FORMAT (1X,F6.2,2X,E13.6,2X,E13.6,2X,E13.6,2X,E13.6)
   11 FORMAT (/"SPHERE SCATTERING PROGRAM"//)
   12 FORMAT (5X,"REFMED = ",F8.4,3X,"REFRE =",E14.6,3X,
     3"REFIM = ",E14.6)
   13 FORMAT (5X,"SPHERE RADIUS = ",F7.3,3X,"WAVELENGTH = ",F7.4)
   14 FORMAT (5X,"SIZE PARAMETER =",F8.3/)
   17 FORMAT (//,2X,"ANGLE",7X,"S11",13X,"POL",13X,"S33",13X,"S34"//)
      STOP
      END
C       ************************************************************
C       SUBROUTINE BHMIE CALCULATES AMPLITUDE SCATTERING MATRIX
C       ELEMENTS AND EFFICIENCIES FOR EXTINCTION, TOTAL SCATTERING
C       AND BACKSCATTERING FOR A GIVEN SIZE PARAMETER AND
C       RELATIVE REFRACTIVE INDEX
C       ************************************************************
      SUBROUTINE BHMIE (X,REFREL,NANG,S1,S2,QEXT,QSCA,QBACK)
      DIMENSION AMU(100),THETA(100),PI(100),TAU(100),PI0(100),PI1(100)
      COMPLEX D(3000),Y,REFREL,,XI,XI0,XI1,AN,BN,S1(200),S2(200)
      DOUBLE PRECISION PSI0,PSI1,PSI,DN,DX
      DX=X
      Y=X*REFREL
C       ************************************
C       SERIES TERMINATED AFTER NSTOP TERMS
C       ************************************
      XSTOP=X+4.*X**.3333+2.0
      NSTOP=XSTOP
      YMOD=CABS(Y)
      NMX=AMAX1(XSTOP,YMOD)+15
      DANG=1.570796327/FLOAT(NANG-1)
      DO 555 J=1,NANG
      THETA(J)=(FLOAT(J)-1.)*DANG
  555 AMU(J)=COS(THETA(J))
C       ***************************************************
C       LOGARITHMIC DERIVATIVE D(J) CALCULATED BY DOWNWARD
C       RECURRENCE BEGINNING WITH INITIAL VALUE 0.0 + I*0.0
C       AT J= NMX
C       ***************************************************
      D(NMX)=CMPLX(0.0,0.0)
      NN=NMX-1
      DO 120 N=1,NN
      RN=NMX-N+1
  120 D(NMX-N)=(RN/Y)-(1./(D(NMX-N+1)+RN/Y))
      DO 666 J=1,NANG
      PI0(J)=0.0
  666 PI1(J)=1.0
      NN=2*NANG-1
      DO 777 J=1,NN
      S1(J)=CMPLX(0.0,0.0)
  777 S2(J)=CMPLX(0.0,0.0)
C       *****************************************
C       RICCATI-BESSEL FINCTIONS WITH REAL ARGUMENT X
C       CALCULATED BY UPWARD RECURRENCE
```

```
115 C       ***********************************************
166         PSI0=DCOS(DX)
117         PSI1=DSIN(DX)
118         CHI0=-SIN(X)
119         CHI1=COS(X)
120         APSI0=PSI0
121         APSI1=PSI1
122         XI0=CMPLX(APSI0,-CHI0)
123         XI1=CMPLX(APSI1,-CHI1)
124         QSCA=0.0
125         N=1
126    200  DN=N
127         RN=N
128         FN=(2.*RN+1.)/(RN*(RN+1.))
129         PSI=(2.*DN-1.)*PSI1/DX-PSI0
130         APSI=PSI
131         CHI=(2.*RN-1.)*CHI1/X - CHI0
132         XI=CMPLX(APSI,-CHI)
133         AN=(D(N)/REFREL+RN/X)*APSI - APSI1
134         AN=AN/((D(N)/REFREL+RN/X)*XI-XI1)
135         BN=(REFREL*D(N)+RN/X)*APSI -APSI1
136         BN=BN/((REFREL*D(N)+RN/X)*XI - XI1)
137         QSCA=QSCA+(2.*RN+1.)*(CABS(AN)+CABS(BN)*CABS(BN))
138         DO 789 J=1,NANG
139         JJ=2*NANG-J
140         PI(J)=PI1(J)
141         TAU(J)=RN*AMU(J)*PI(J) - (RN+1.)*PI0(J)
142         P=(-1.)**(N-1)
143         S1(J)=S1(J)+FN*(AN*PI(J)+BN*TAU(J))
144         T=(-1.)**N
145         S2(J)=S2(J)+FN*(AN*TAU(J)+BN*PI(J))
146         IF(J.EQ.JJ)GO TO 789
147         S1(JJ)=S1(JJ) + FN*(AN*PI(J)*P+BN*TAU(J)*T)
148         S2(JJ)=S2(JJ)+FN*(AN*TAU(J)*T+BN*PI(J)*P)
149    789  CONTINUE
150         PSI0=PSI1
151         PSI1=PSI
152         APSI1=PSI1
153         CHI0=CHI1
154         CHI1=CHI
155         XI1=CMPLX(APSI1,-CHI1)
156         N=N+1
157         RN=N
158         DO 999 J=1,NANG
159         PI1(J)=((2.*RN-1.)/(RN-1))*AMU(J)*PI(J)
160         PI1(J)=PI1(J)-RN*PI0(J)/(RN-1.)
161    999  PI0(J)=PI(J)
162         IF (N-1-NSTOP) 200,300,300
163    300  QSCA=(2./(X*X))*QSCA
164         QEXT=(4./(X*X))*REAL(S1(1))
165         QBACK=(4./(X*X))*CABS(S1(2*NANG-1))*CABS(S1(2*NANG-1))
166         RETURN
167         END
```

ADDENDUM C

Density Determination

Determination of density of ash sample (by volumee displacement method)

Glycerol (gylcerine)

Formula	Density at 20 C(g/cc)
$CH_2OHCHOHCH_2OH$	1.2613

Composition	
$CH_2OHCHOHCH_2OH$	99.70%
Water	0.10%
Sulfate	0.0003%
Chlorinated Compounds	0.0006%

Ash A1

Test1		Test2	
1.Volume of flask (ml)	5	1.Volume of flassk (ml)	5
2.weight of flask (g)	11.1761	2.weight of flaskk (g)	11.4076
3.weight of sample (g)	0.0219	3.weight of sampple (g)	0.022
4.weight of flask+sample+solvent (g)	17.4458	4.weight of flaskk+sample+solvent (g)	17.6754
Weight of solvent in 5 ml flask (g)	6.2478	Weight of solveent in 5 ml flask (g)	6.2458
Volume of solvent in 5 ml flask (cc)	4.9535	Volume of solveent in 5 ml flask (cc)	4.9519
Volume of Ash in 5 ml flask (cc)	0.0465	Volume of Ash i in 5 ml flask (cc)	0.0481
Density of Sample (g/cc)	**0.4706**	**Density of Saample (g/cc)**	**0.4571**

Test 3		Test 4	
1.Volume of flask (ml)	5	1.Volume of flassk (ml)	5
2.weight of flask (g)	10.705	2.weight of flaskk (g)	11.0173
3.weight of sample (g)	0.0218	3.weight of sampple (g)	0.0219
4.weight of flask+sample+solvent (g)	16.9725	4.weight of flaskk+sample+solvent (g)	17.2876
Weight of solvent in 5 ml flask (g)	6.2457	Weight of solveent in 5 ml flask (g)	6.2484
Volume of solvent in 5 ml flask (cc)	4.9518	Volume of solveent in 5 ml flask (cc)	4.9539
Volume of Ash in 5 ml flask (cc)	0.0482	Volume of Ash i in 5 ml flask (cc)	0.0461
Density of Sample (g/cc)	0.4522	**Density of Saample (g/cc)**	0.4754

Test5		Test6	
1.Volume of flask (ml)	5	1.Volume of flassk (ml)	5
2.weight of flask (g)	11.1761	2.weight of flaskk (g)	11.4076
3.weight of sample (g)	0.0218	3.weight of sampple (g)	0.022
4.weight of flask+sample+solvent (g)	17.4487	4.weight of flaskk+sample+solvent (g)	17.6789
Weight of solvent in 5 ml flask (g)	6.2508	Weight of solveent in 5 ml flask (g)	6.2493
Volume of solvent in 5 ml flask (cc)	4.9558	Volume of solveent in 5 ml flask (cc)	4.9546
Volume of Ash in 5 ml flask (cc)	0.0442	Volume of Ash i in 5 ml flask (cc)	0.0454
Density of Sample (g/cc)	0.4937	**Density of Saample (g/cc)**	0.4851

Average density of ash A1 =	0.472

Table C-1. The average density of ash A1

Ash A2

Test1	
1.Volume of flask (ml)	5
2.weight of flask (g)	10.705
3.weight of sample (g)	0.0223
4.weight of flask+sample+solvent (g)	16.9778
Weight of solvent in 5 ml flask (g)	6.2505
Volume of solvent in 5 ml flask (cc)	4.9556
Volume of Ash in 5 ml flask (cc)	0.0444
Density of Sample (g/cc)	0.5023

Teest2	
1.Wolume of flask (ml)	5
2.wweight of flask (g)	11.0173
3.wweight of sample (g)	0.022
4.wweight of flask+sample+solvent (g)	17.2867
Weeight of solvent in 5 ml flask (g)	6.2474
Voblume of solvent in 5 ml flask (cc)	4.9531
Voolume of Ash in 5 ml flask (cc)	0.0469
Deensity of Sample (g/cc)	0.4695

Test 3	
1.Volume of flask (ml)	5
2.weight of flask (g)	11.1761
3.weight of sample (g)	0.0223
4.weight of flask+sample+solvent (g)	17.4502
Weight of solvent in 5 ml flask (g)	6.2518
Volume of solvent in 5 ml flask (cc)	4.9566
Volume of Ash in 5 ml flask (cc)	0.0434
Density of Sample (g/cc)	0.5142

Teest 4	
1.Wolume of flask (ml)	5
2.wweight of flask (g)	11.4076
3.wweight of sample (g)	0.0218
4.wweight of flask+sample+solvent (g)	17.6787
Weeight of solvent in 5 ml flask (g)	6.2493
Voolume of solvent in 5 ml flask (cc)	4.9546
Voolume of Ash in 5 ml flask (cc)	0.0454
Deensity of Sample (g/cc)	0.4807

Test5	
1.Volume of flask (ml)	5
2.weight of flask (g)	10.705
3.weight of sample (g)	0.0219
4.weight of flask+sample+solvent (g)	16.9724
Weight of solvent in 5 ml flask (g)	6.2455
Volume of solvent in 5 ml flask (cc)	4.9516
Volume of Ash in 5 ml flask (cc)	0.0484
Density of Sample (g/cc)	0.4528

Teest6	
1.Wolume of flask (ml)	5
2.wweight of flask (g)	11.0173
3.wweight of sample (g)	0.0218
4.wweight of flask+sample+solvent (g)	17.2898
Weeight of solvent in 5 ml flask (g)	6.2507
Voolume of solvent in 5 ml flask (cc)	4.9558
Voolume of Ash in 5 ml flask (cc)	0.0442
Deensity of Sample (g/cc)	0.4928

Average density of ash A2 =	**0.485**

Table C-2. The average density of ash A2

Ash . B

Test1	
1.Volume of flask (ml)	5
2.weight of flask (g)	11.1761
3.weight of sample (g)	0.02
4.weight of flask+sample+solvent (g)	17.384
Weight of solvent in 5 ml flask (g)	6.1879
Volume of solvent in 5 ml flask (cc)	4.9060
Volume of Ash in 5 ml flask (cc)	0.0940
Density of Sample (g/cc)	0.2127

Test2	
1.Volume of flask (ml)	5
2.weight of flask (g)	11.1761
3.weight of sample (g)	0.0235
4.weight of flask+sample+solvent (g)	17.4004
Weight of solvent in 5 ml flask (g)	6.2008
Volume of solvent in 5 ml flask (cc)	4.9162
Volume of Ash in 5 ml flask (cc)	0.0838
Density of Sample (g/cc)	0.2804

Test 3	
1.Volume of flask (ml)	5
2.weight of flask (g)	11.4076
3.weight of sample (g)	0.0207
4.weight of flask+sample+solvent (g)	17.5844
Weight of solvent in 5 ml flask (g)	6.1561
Volume of solvent in 5 ml flask (cc)	4.8808
Volume of Ash in 5 ml flask (cc)	0.1192
Density of Sample (g/cc)	0.1736

Test 4	
1.Volume of flask (ml)	5
2.weight of flask (g)	11.1761
3.weight of sample (g)	0.0253
4.weight of flask+sample+solvent (g)	17.4024
Weight of solvent in 5 ml flask (g)	6.201
Volume of solvent in 5 ml flask (cc)	4.9164
Volume of Ash in 5 ml flask (cc)	0.0836
Density of Sample (g/cc)	0.3025

Test5	
1.Volume of flask (ml)	5
2.weight of flask (g)	11.174
3.weight of sample (g)	0.0268
4.weight of flask+sample+solvent (g)	17.3564
Weight of solvent in 5 ml flask (g)	6.1556
Volume of solvent in 5 ml flask (cc)	4.8804
Volume of Ash in 5 ml flask (cc)	0.1196
Density of Sample (g/cc)	0.2240

Test6	
1.Volume of flask (ml)	5
2.weight of flask (g)	11.4076
3.weight of sample (g)	0.0242
4.weight of flask+sample+solvent (g)	17.563
Weight of solvent in 5 ml flask (g)	6.1312
Volume of solvent in 5 ml flask (cc)	4.8610
Volume of Ash in 5 ml flask (cc)	0.1390
Density of Sample (g/cc)	0.1741

Average density of ash B =	0.228

Table C-3. The average density of ash B

Ash C

Test1	
1.Volume of flask (ml)	5
2.weight of flask (g)	11.4076
3.weight of sample (g)	0.0218
4.weight of flask+sample+solvent (g)	17.639
Weight of solvent in 5 ml flask (g)	6.2096
Volume of solvent in 5 ml flask (cc)	4.9232
Volume of Ash in 5 ml flask (cc)	0.0768
Density of Sample (g/cc)	0.2838

Test2	
1.Volume of flask (ml)	5
2.weight of flask (g)	11.1761
3.weight of sample (g)	0.0223
4.weight of flask+sample+solvent (g)	17.369
Weight of solvent in 5 ml flask (g)	6.1706
Volume of solvent in 5 ml flask (cc)	4.8923
Volume of Ash in 5 ml flask (cc)	0.1077
Density of Sample (g/cc)	0.2070

Test 3	
1.Volume of flask (ml)	5
2.weight of flask (g)	11.4076
3.weight of sample (g)	0.0228
4.weight of flask+sample+solvent (g)	17.6065
Weight of solvent in 5 ml flask (g)	6.1761
Volume of solvent in 5 ml flask (cc)	4.8966
Volume of Ash in 5 ml flask (cc)	0.1034
Density of Sample (g/cc)	0.2205

Test 4	
1.Volume of flask (ml)	5
2.weight of flask (g)	11.174
3.weight of sample (g)	0.0226
4.weight of flask+sample+solvent (g)	17.3987
Weight of solvent in 5 ml flask (g)	6.2021
Volume of solvent in 5 ml flask (cc)	4.9172
Volume of Ash in 5 ml flask (cc)	0.0828
Density of Sample (g/cc)	0.2730

Test5	
1.Volume of flask (ml)	5
2.weight of flask (g)	11.1761
3.weight of sample (g)	0.0226
4.weight of flask+sample+solvent (g)	17.3548
Weight of solvent in 5 ml flask (g)	6.1561
Volume of solvent in 5 ml flask (cc)	4.8808
Volume of Ash in 5 ml flask (cc)	0.1192
Density of Sample (g/cc)	0.1895

Test6	
1.Volume of flask (ml)	5
2.weight of flask (g)	11.1761
3.weight of sample (g)	0.0229
4.weight of flask+sample+solvent (g)	17.403
Weight of solvent in 5 ml flask (g)	6.204
Volume of solvent in 5 ml flask (cc)	4.9187
Volume of Ash in 5 ml flask (cc)	0.0813
Density of Sample (g/cc)	0.2818

Average density of ash C	0.243

Table C-4. The average density of ash C

Ash D

Test1	
1.Volume of flask (ml)	5
2.weight of flask (g)	11.1761
3.weight of sample (g)	0.0236
4.weight of flask+sample+solvent (g)	17.413
Weight of solvent in 5 ml flask (g)	6.2133
Volume of solvent in 5 ml flask (cc)	4.9261
Volume of Ash in 5 ml flask (cc)	0.0739
Density of Sample (g/cc)	0.3194

Test2	
1.Volume of flask (ml)	5
2.weight of flask (g)	11.4076
3.weight of sample (g)	0.0242
4.weight of flask+sample+solvent (g)	17.5686
Weight of solvent in 5 ml flask (g)	6.1368
Volume of solvent in 5 ml flask (cc)	4.8655
Volume of Ash in 5 ml flask (cc)	0.1345
Density of Sample (g/cc)	0.1799

Test 3	
1.Volume of flask (ml)	5
2.weight of flask (g)..	10.705
3.weight of sample (g)	0.0236
4.weight of flask+sample+solvent (g)	16.9289
Weight of solvent in 5 ml flask (g)	6.2003
Volume of solvent in 5 ml flask (cc)	4.9158
Volume of Ash in 5 ml flask (cc)	0.0842
Density of Sample (g/cc)	0.2803

Test 4	
1.Volume of flask (ml)	5
2.weight of flask (g)	11.0173
3.weight of sample (g)	0.023
4.weight of flask+sample+solvent (g)	17.2408
Weight of solvent in 5 ml flask (g)	6.2005
Volume of solvent in 5 ml flask (cc)	4.9160
Volume of Ash in 5 ml flask (cc)	0.0840
Density of Sample (g/cc)	0.2737

Test5	
1.Volume of flask (ml)	5
2.weight of flask (g)	11.1761
3.weight of sample (g)	0.0243
4.weight of flask+sample+solvent (g)	17.3451
Weight of solvent in 5 ml flask (g)	6.1447
Volume of solvent in 5 ml flask (cc)	4.8717
Volume of Ash in 5 ml flask (cc)	0.1283
Density of Sample (g/cc)	0.1894

Test6	
1.Volume of flask (ml)	5
2.weight of flask (g)	11.4076
3.weight of sample (g)	0.0238
4.weight of flask+sample+solvent (g)	17.6021
Weight of solvent in 5 ml flask (g)	6.1707
Volume of solvent in 5 ml flask (cc)	4.8923
Volume of Ash in 5 ml flask (cc)	0.1077
Density of Sample (g/cc)	0.2211

Average density of ash D =	0.244

Table C-5. The average density of ash D

Ashh E

Test1	
1.Volume of flask (ml)	55
2.weight of flask (g)	11.17611
3.weight of sample (g)	0.02444
4.weight of flask+sample+solvent (g)	17.43666
Weight of solvent in 5 ml flask (g)	6.23611
Volume of solvent in 5 ml flask (cc)	4.94422
Volume of Ash in 5 ml flask (cc)	0.05588
Density of Sample (g/cc)	0.43722

Test2	
1.Volume of flask (ml)	5
2.weight of flask (g)	11.4076
3.weight of sample (g)	0.0241
4.weight of flask+sample+solvent (g)	17.6661
Weight of solvent in 5 ml flask (g)	6.2344
Volume of solvent in 5 ml flask (cc)	4.9428
Volume of Ash in 5 ml flask (cc)	0.0572
Density of Sample (g/cc)	0.4216

Test 3	
1.Volume of flask (ml)	55
2.weight of flask (g)	10.7055
3.weight of sample (g)	0.02477
4.weight of flask+sample+solvent (g)	16.9622
Weight of solvent in 5 ml flask (g)	6.23233
Volume of solvent in 5 ml flask (cc)	4.94122
Volume of Ash in 5 ml flask (cc)	0.05888
Density of Sample (g/cc)	0.41999

Test 4	
1.Volume of flask (ml)	5
2.weight of flask (g)	11.0173
3.weight of sample (g)	0.0249
4.weight of flask+sample+solvent (g)	17.2758
Weight of solvent in 5 ml flask (g)	6.2336
Volume of solvent in 5 ml flask (cc)	4.9422
Volume of Ash in 5 ml flask (cc)	0.0578
Density of Sample (g/cc)	0.4308

Test5	
1.Volume of flask (ml)	55
2.weight of flask (g)	11.17611
3.weight of sample (g)	0.02344
4.weight of flask+sample+solvent (g)	17.4411
Weight of solvent in 5 ml flask (g)	6.24155
Volume of solvent in 5 ml flask (cc)	4.94835
Volume of Ash in 5 ml flask (cc)	0.05155
Density of Sample (g/cc)	0.45411

Test6	
1.Volume of flask (ml)	5
2.weight of flask (g)	11.4076
3.weight of sample (g)	0.0233
4.weight of flask+sample+solvent (g)	17.6717
Weight of solvent in 5 ml flask (g)	6.2408
Volume of solvent in 5 ml flask (cc)	4.9479
Volume of Ash in 5 ml flask (cc)	0.0521
Density of Sample (g/cc)	0.4473

Average density of ash E =	**0.4355**

Table C-6. the average density of ash E

Ash F

Test1	
1.Volume of flask (ml)	5
2.weight of flask (g)	10.705
3.weight of sample (g)	0.0234
4.weight of flask+sample+solvent (g)	16.9805
Weight of solvent in 5 ml flask (g)	6.2521
Volume of solvent in 5 ml flask (cc)	4.9569
Volume of Ash in 5 ml flask (cc)	0.0431
Density of Sample (g/cc)	0.5425

Test2	
1.Volume of flask (ml)	5
2.weight of flask (g)	11.0173
3.weight of sample (g)	0.0231
4.weight of flask+sample+solvent (g)	17.2887
Weight of solvent in 5 ml flask (g)	6.2483
Volume of solvent in 5 ml flask (cc)	4.9539
Volume of Ash in 5 ml flask (cc)	0.0461
Density of Sample (g/cc)	0.5006

Test 3	
1.Volume of flask (ml)	5
2.weight of flask (g)	11.1761
3.weight of sample (g)	0.0226
4.weight of flask+sample+solvent (g)	17.4512
Weight of solvent in 5 ml flask (g)	6.2525
Volume of solvent in 5 ml flask (cc)	4.9572
Volume of Ash in 5 ml flask (cc)	0.0428
Density of Sample (g/cc)	0.5279

Test 4	
1.Volume of flask (ml)	5
2.weight of flask (g)	11.4076
3.weight of sample (g)	0.023
4.weight of flask+sample+solvent (g)	17.6752
Weight of solvent in 5 ml flask (g)	6.2446
Volume of solvent in 5 ml flask (cc)	4.9509
Volume of Ash in 5 ml flask (cc)	0.0491
Density of Sample (g/cc)	0.4687

Test5	
1.Volume of flask (ml)	5
2.weight of flask (g)	10.705
3.weight of sample (g)	0.0225
4.weight of flask+sample+solvent (g)	16.9823
Weight of solvent in 5 ml flask (g)	6.2548
Volume of solvent in 5 ml flask (cc)	4.9590
Volume of Ash in 5 ml flask (cc)	0.0410
Density of Sample (g/cc)	0.5489

Test6	
1.Volume of flask (ml)	5
2.weight of flask (g)	11.0173
3.weight of sample (g)	0.0226
4.weight of flask+sample+solvent (g)	17.2914
Weight of solvent in 5 ml flask (g)	6.2515
Volume of solvent in 5 ml flask (cc)	4.9564
Volume of Ash in 5 ml flask (cc)	0.0436
Density of Sample (g/cc)	0.5183

Average density of ash F =	**0.518**

Table C-7. The average density of ash F

Material	Density (g/cm)
Na_2SO_4	2.698
Na_2CO_3	2.533
K_2SO_4	2.662
K_2CO_3	2.290
Ash A1	0.472
Ash A2	0.485
Ash B	0.228
Ash C	0.243
Ash D	0.244
Ash E	0.435
Ash F	0.518

Table C-8. The average density of the materials

ADDENDUM D:

Particle Diameter Determination

Size Distributiom of materials

Na_2SiO_4

Size diameter (microns)	Number of particldes	Surface area of total particles (micron^2)
0.50	75	58.91
1.00	66	207.37
1.50	35	247.43
2.00	68	854.62
2.50	58	1138.98
3.00	21	593.84
3.50	-	-
4.00	3	150.82
4.50	2	127.25
5.00	6	471.30
5.50	-	-
6.00	3	339.34
6.50	4	531.00
7.00	-	-
7.50	5	883.69
8.00	-	-
8.50	-	-
9.00	-	-
9.50	-	-
10.00	-	-
10.50	-	-
11.00	6	2281.09
Total	352	7885.63

Average diameter (microns) = 2.56

Table D-1. The average particle diameter of Na_2SO_4

Na_2CO_3

Size diameter (microns)	Number of particles	Surface area of total particles (micron^2)
0.50	15	11.78
1.00	65	204.23
1.50	54	381.75
2.00	63	791.78
2.50	21	412.39
3.00	14	395.89
3.50	19	731.30
4.00	4	201.09
4.50	-	-
5.00	7	549.85
5.50	-	-
6.00	5	565.56
6.50	-	-
7.00	6	923.75
7.50	-	-
8.00	-	-
8.50	-	-
9.00	-	-
9.50	-	-
10.00	7	2199.40
10.50	-	-
11.00	1	-
Total	281	7368.78
Average diameter (microns) =	2.77	

Table D-2. The average particle diameter of Na_2CO_3

K_2SO_4

Size diameter (microns)	Number of particless	Surface area of total particles (micron^2)
0.50	5	3.93
1.00	40	125.68
1.50	70	494.87
2.00	28	351.90
2.50	24	471.30
3.00	5	141.39
3.50	8	307.92
4.00	9	452.45
4.50	7	445.38
5.00	7	549.85
5.50	6	570.27
6.00	9	1018.01
6.50	-	-
7.00	7	1077.71
7.50	-	-
8.00	4	804.35
8.50	-	-
9.00	-	-
9.50	-	-
10.00	-	-
10.50	-	-
11.00	-	-
Total	229	6815.00
Average diameter (microns) =	2.95	

Table D-3. The average particle diameter of K_2SO_4

K_2CO_3

Size diameter (microns)	Number of partticles	Surface area of total particles (micron^2)
0.50	4	3.14
1.00	32	100.54
1.50	38	268.64
2.00	56	703.81
2.50	40	785.50
3.00	45	1272.51
3.50	9	346.41
4.00	7	351.90
4.50	3	190.88
5.00	2	157.10
5.50	4	380.18
6.00	4	452.45
6.50	3	398.25
7.00	2	307.92
7.50	4	706.95
8.00	-	-
8.50	-	-
9.00	-	-
9.50	-	-
10.00	-	-
10.50	-	-
11.00	-	-
Total	253	6426.18

Average diameter (microns) = 2.73

Table D-4. The average particle diameter of K_2CO_3

Ash . A1

Size diameter (microns)	Number of particles	Surface area of total particles (micron^2)
0.50	8	6.28
1.00	32	100.54
1.50	44	311.06
2.00	34	427.31
2.50	35	687.31
3.00	82	2318.80
3.50	15	577.34
4.00	16	804.35
4.50	-	-
5.00	-	-
5.50	-	-
6.00	-	-
6.50	-	-
7.00	-	-
7.50	-	-
8.00	3	603.26
8.50	-	-
9.00	3	763.51
9.50	-	-
10.00	-	-
10.50	-	-
11.00	-	-
Total	266	6599.77
Average diameter (microns) =	2.70	

Table D-5. The average particle diameter of Ash A1

Ash A2

Size diameter (microns)	Number of particicles	Surface area of total particles (micron^2)
0.50	15	11.78
1.00	21	65.98
1.50	23	162.60
2.00	24	301.63
2.50	42	824.78
3.00	89	2516.74
3.50	33	1270.15
4.00	11	552.99
4.50	8	509.00
5.00	-	-
5.50	-	-
6.00	7	791.78
6.50	4	531.00
7.00	-	-
7.50	-	-
8.00	3	603.26
8.50	-	-
9.00	2	509.00
9.50	-	-
10.00	-	-
10.50	-	-
11.00	-	-
Total	282	8650.71
Average diameter (microns) =	3.00	

Table D-6. The average particle diameter of Ash A2

Ash B

Size diameter (microns)	Number of particicles	Surface area of total particles (micron^2)
0.50	56	43.99
1.00	147	461.87
1.50	91	643.32
2.00	85	1068.28
2.50	40	785.50
3.00	32	904.90
3.50	4	153.96
4.00	5	251.36
4.50	3	190.88
5.00	7	549.85
5.50	-	-
6.00	3	339.34
6.50	2	265.50
7.00	1	153.96
7.50	1	176.74
8.00	2	402.18
8.50	-	-
9.00	-	-
9.50	-	-
10.00	-	-
10.50	-	-
11.00	-	-
Total	479	6391.61
Average diameter (microns) =	1.98	

Table D-7. The average particle diameter of Ash B

Ash C

Size diameter (microns)	Number of particles	Surface area of total particles (micron^2)
0.50	76	59.70
1.00	111	348.76
1.50	108	763.51
2.00	87	1093.42
2.50	30	589.13
3.00	13	367.61
3.50	8	307.92
4.00	2	100.54
4.50	4	254.50
5.00	-	-
5.50	-	-
6.00	1	113.11
6.50	-	-
7.00	2	307.92
7.50	-	-
8.00	2	402.18
8.50	-	-
9.00	-	-
9.50	-	-
10.00	-	-
10.50	-	-
11.00	-	-
Total	444	4708.29
Average diameter (microns) =	1.76	

Table D-8. The average particle diameter of Ash C

Ash D

Size diameter (microns)	Number of particlees	Surface area of total particles (micron^2)
0.50	32	25.14
1.00	58	182.24
1.50	76	537.28
2.00	182	2287.38
2.50	121	2376.14
3.00	76	2149.13
3.50	16	615.83
4.00	6	301.63
4.50	-	-
5.00	3	235.65
5.50	-	-
6.00	3	339.34
6.50	-	-
7.00	2	307.92
7.50	-	-
8.00	-	-
8.50	-	-
9.00	-	-
9.50	-	-
10.00	-	-
10.50	-	-
11.00	-	-
Total	575	9357.66
Average diameter (microns) =	2.18	

Table D-9. The average particle diameter of Ash D

Ash E

Size diameter (microns)	Number of particlees	Surface area of total particles (micron^2)
0.50	66	51.84
1.00	148	465.02
1.50	87	615.05
2.00	37	465.02
2.50	4	78.55
3.00	5	141.39
3.50	1	38.49
4.00	-	-
4.50	-	-
5.00	-	-
5.50	-	-
6.00	1	113.11
6.50	-	-
7.00	-	-
7.50	-	-
8.00	1	201.09
8.50	-	-
9.00	-	-
9.50	-	-
10.00	-	-
10.50	-	-
11.00	-	-
Total	350	2169.55

Average diameter (microns) = 1.35

Table D-10. The average particle diameter of Ash E

Ash F

Size diameter (microns)	Number of particlees	Surface area of total particles (micron^2)
0.50	72	56.56
1.00	154	483.87
1.50	121	855.41
2.00	33	414.74
2.50	6	117.83
3.00	4	113.11
3.50	3	115.47
4.00	1	50.27
4.50	2	127.25
5.00	2	157.10
5.50	1	95.05
6.00	-	-
6.50	-	-
7.00	1	153.96
7.50	-	-
8.00	-	-
8.50	-	-
9.00	1	254.50
9.50	-	-
10.00	-	-
10.50	-	-
11.00	-	-
Total	401	2995.11
Average diameter (microns) =	1.48	

Table D-11. The average particle diameter of Ash F

Materials	Mean Particle size (microns)
1.Na_2SO_4	2.56
2.Na_2CO_3	2.77
3.K_2SO_4	2.95
4.K_2CO_3	2.73
5.Ash A1	2.70
6.Ash A2	3.00
7.Ash B	1.98
8.Ash C	1.76
9.Ash D	2.18
10.Ash E	1.35
11.Ash F	1.48

Table D-12. Mean particle diameter

ADDENDUM E:

The Optical Constant Data

Wavenumber(cm^{-1})	n	k
0	1.521	0
50	1.521	0
100	1.522	0
150	1.523	0
200	1.524	0
250	1.526	0
300	1.529	0
350	1.534	0
400	1.54	0
450	1.552	0
500	1.574	0.014
550	1.597	0.046
600	1.616	0.144
650	1.403	0.108
700	1.442	0.015
750	1.487	0.001
800	1.511	0.006
850	1.527	0.011
900	1.543	0.022
950	1.558	0.04
1000	1.569	0.065
1050	1.577	0.096
1100	1.598	0.186
1150	1.393	0.228
1200	1.378	0.085
1250	1.408	0.062
1300	1.419	0.05
1350	1.427	0.043
1400	1.432	0.04
1450	1.435	0.033
1500	1.44	0.03
1550	1.446	0.029
1600	1.452	0.036
1650	1.434	0.037
1700	1.437	0.024
1750	1.44	0.02
1800	1.443	0.018
1850	1.446	0.017
1900	1.448	0.016
1950	1.449	0.016
2000	1.45	0.015
2050	1.46	0.015
2100	1.452	0.015
2150	1.451	0.014
2200	1.451	0.013

Wavenumber(cm^{-1})	n	k
2250	1.452	0.013
2300	1.452	0.012
2350	1.452	0.012
2400	1.453	0.011
2450	1.453	0.011
2500	1.454	0.01
2550	1.454	0.01
2600	1.454	0.01
2650	1.454	0.01
2700	1.455	0.009
2750	1.455	0.009
2800	1.455	0.009
2850	1.455	0.009
2900	1.455	0.008
2950	1.455	0.008
3000	1.455	0.008
3050	1.455	0.008
3100	1.455	0.007
3150	1.455	0.007
3200	1.455	0.007
3250	1.455	0.007
3300	1.455	0.007
3350	1.455	0.006
3400	1.455	0.006
3450	1.455	0.006
3500	1.455	0.006
3550	1.455	0.006
3600	1.455	0.005
3650	1.455	0.005
3700	1.454	0.004
3750	1.454	0.004
3800	1.455	0.004
3850	1.455	0.003
3900	1.455	0.003
3950	1.455	0.002
4000	1.455	0.003
4050	1.455	0.002
4100	1.455	0.002
4150	1.455	0.001
4200	1.455	0.001
4250	1.455	0.001
4300	1.455	0.001
4350	1.455	0.001
4400	1.455	0.001
4450	1.455	0.001

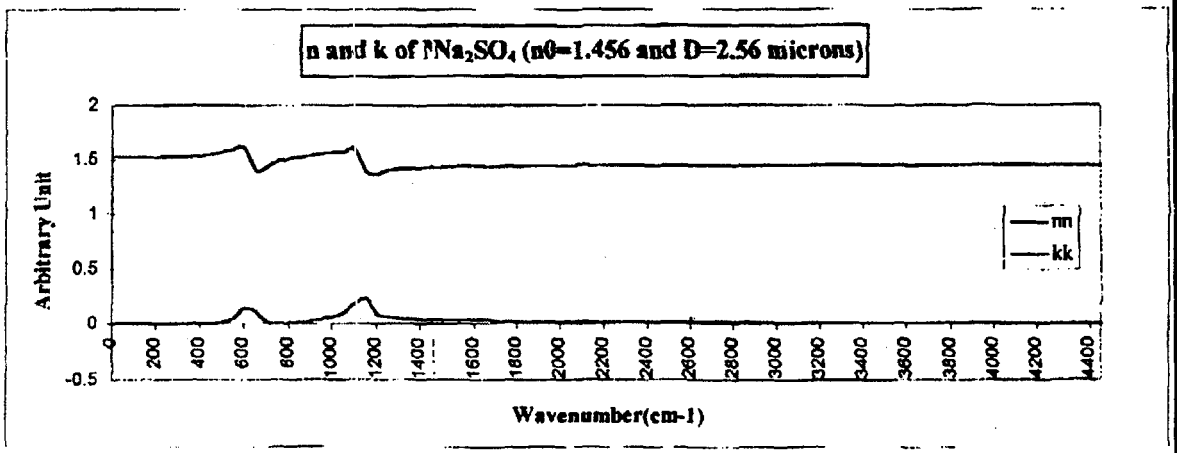

Figure E-1. The Optical constant results of Na_2So_4 at$_0$ =1.456 and Diameter = 2.56 microns

Wavenumber(cm^{-1})	n	k
0	1.71	0
50	1.71	0
100	1.71	0
150	1.711	0
200	1.712	0
250	1.714	0
300	1.717	0
350	1.723	0
400	1.748	0.012
450	1.721	0.028
500	1.715	0.025
550	1.717	0.027
600	1.704	0.033
650	1.698	0.018
700	1.711	0.042
750	1.707	0
800	1.723	0
850	1.757	0.006
900	1.654	0.037
950	1.708	0.012
1000	1.725	0.016
1050	1.731	0.021
1100	1.739	0.023
1150	1.75	0.028
1200	1.763	0.037
1250	1.775	0.05
1300	1.791	0.067
1350	1.815	0.094
1400	1.864	0.16
1450	1.776	0.424
1500	1.54	0.224
1550	1.557	0.144
1600	1.582	0.118
1650	1 58	0.106
1700	1.584	0.086
1750	1.589	0.073
1800	1.593	0.068
1850	1.597	0.06
1900	1.6	0.055
1950	1.603	0.05
2000	1.605	0.047
2050	1.606	0.044
2100	1.608	0.04
2150	1.609	0.038
2200	1.61	0.035

Wavenumber(cm^{-1})	n	k
2250	1.611	0.033
2300	1.612	0.031
2350	1.613	0.027
2400	1.616	0.027
2450	1.617	0.025
2500	1.623	0.028
2550	1.617	0.027
2600	1.618	0.025
2650	1.618	0.023
2700	1.618	0.021
2750	1.619	0.02
2800	1.619	0.019
2850	1.62	0.018
2900	1.62	0.018
2950	1.621	0.017
3000	1.621	0.016
3050	1.621	0.015
3100	1.622	0.015
3150	1.622	0.014
3200	1.622	0.014
3250	1.622	0.013
3300	1.622	0.012
3350	1.623	0.012
3400	1.623	0.011
3450	1.623	0.011
3500	1.623	0.01
3550	1.623	0.01
3600	1.623	0.009
3650	1.623	0.009
3700	1.623	0.008
3750	1.623	0.008
3800	1.623	0.006
3850	1.624	0.006
3900	1.624	0.006
3950	1.623	0.005
4000	1.624	0.005
4050	1 624	0.004
4100	1.624	0.004
4150	1.624	0.003
4200	1.624	0.003
4250	1.624	0.002
4300	1.624	0.002
4350	1.624	0.001
4400	1.624	0.001
4450	1.624	0

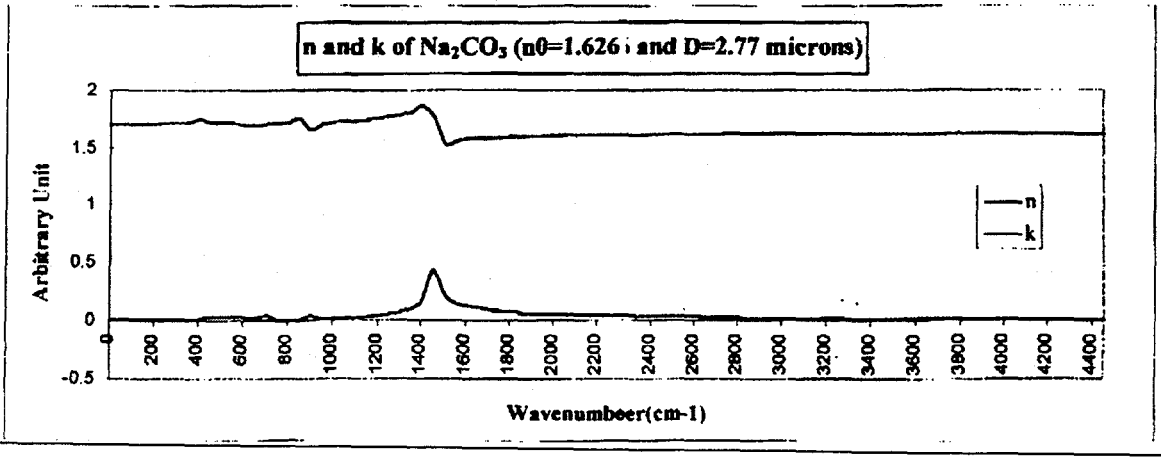

Figure E-2. The Optical constant results of Na_2CO_3 at $n_0 = 1.626$ and Diameter = 2.77 microns

Wavenumber(cm^{-1})	n	k
0	1.533	0
50	1.533	0
100	1.534	0
150	1.536	0
200	1.539	0
250	1.543	0
300	1.549	0
350	1.562	0
400	1.614	0.027
450	1.561	0.064
500	1.551	0.069
550	1.564	0.062
600	1.601	0.14
650	1.372	0.056
700	1.45	0.005
750	1.489	0.002
800	1.512	0.008
850	1.526	0.015
900	1.54	0.023
950	1.558	0.037
1000	1.572	0.06
1050	1.59	0.097
1100	1.638	0.221
1150	1.338	0.23
1200	1.37	0.072
1250	1.402	0.056
1300	1.416	0.043
1350	1.426	0.037
1400	1.432	0.035
1450	1.437	0.031
1500	1.443	0.031
1550	1.44	0.028
1600	1.446	0.029
1650	1.436	0.034
1700	1.436	0.024
1750	1.437	0.017
1800	1.441	0.014
1850	1.444	0.012
1900	1.447	0.011
1950	1.449	0.01
2000	1.45	0.01
2050	1.452	0.01
2100	1.452	0.01
2150	1.453	0.01
2200	1.454	0.009

Wavenumber(cm^{-1})	n	k
2250	1.455	0.008
2300	1.455	0.009
2350	1.455	0.008
2400	1.455	0.007
2450	1.456	0.007
2500	1.457	0.007
2550	1.458	0.007
2600	1.458	0.006
2650	1.458	0.006
2700	1.459	0.006
2750	1.459	0.006
2800	1.459	0.006
2850	1.46	0.006
2900	1.46	0.006
2950	1.46	0.006
3000	1.46	0.006
3050	1.46	0.006
3100	1.46	0.006
3150	1.46	0.005
3200	1.46	0.005
3250	1.46	0.005
3300	1.46	0.005
3350	1.46	0.005
3400	1.46	0.005
3450	1.46	0.005
3500	1.46	0.005
3550	1.46	0.005
3600	1.46	0.005
3650	1.46	0.004
3700	1.461	0.005
3750	1.458	0.005
3800	1.46	0.005
3850	1.46	0.006
3900	1.458	0.003
3950	1.458	0.002
4000	1.459	0.003
4050	1.459	0.002
4100	1.459	0.002
4150	1.459	0.001
4200	1.459	0.001
4250	1.459	0.001
4300	1.459	0.001
4350	1.459	0
4400	1.459	0.001
4450	1.458	0.001

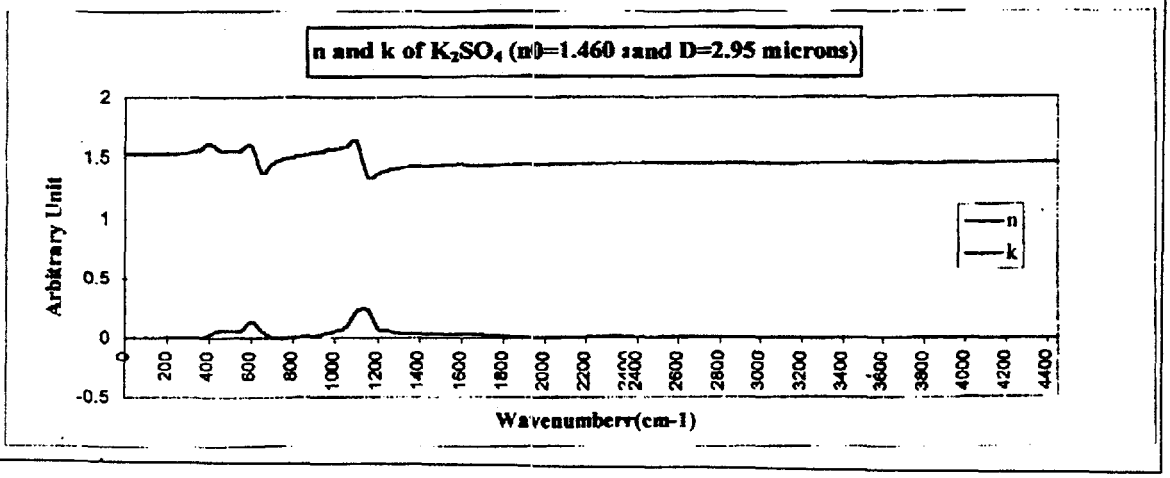

Figure E-3. The Optical constant results of K_2SO_4 at $n_0 = 1.460$ and Diameter = 2.95 microns

Wavenumber(cm^{-1})	n	k
0	1.65	0
50	1.651	0
100	1.651	0
150	1.651	0
200	1.652	0
250	1.654	0
300	1.656	0
350	1.659	0
400	1.675	0.008
450	1.659	0.019
500	1.655	0.019
550	1.657	0.022
600	1.643	0.029
650	1.635	0.013
700	1.636	0.01
750	1.645	0
800	1.653	0.006
850	1.66	0.005
900	1.609	0.008
950	1.647	0
1000	1.658	0.003
1050	1.66	0.008
1100	1.666	0.004
1150	1.676	0.004
1200	1.689	0.01
1250	1.704	0.02
1300	1.724	0.037
1350	1 76	0.082
1400	1.782	0.247
1450	1.549	0.178
1500	1.526	0.093
1550	1.557	0.06
1600	1.572	0.051
1650	1.572	0.045
1700	1.576	0.034
1750	1.584	0.034
1800	1.584	0.024
1850	1.588	0.021
1900	1.591	0.019
1950	1.593	0.018
2000	1.595	0.017
2050	1.596	0.016
2100	1.597	0.015
2150	1.598	0.014
2200	1.6	0.013

Wavenumber(cm^{-1})	n	k
2250	1.601	0.012
2300	1.601	0.012
2350	1.602	0.011
2400	1.603	0.01
2450	1.607	0.013
2500	1.603	0.011
2550	1.603	0.01
2600	1.604	0.009
2650	1.604	0.009
2700	1.605	0.008
2750	1.605	0.008
2800	1.607	0.009
2850	1.606	0.009
2900	1.606	0.009
2950	1.606	0.008
3000	1.606	0.008
3050	1.606	0.008
3100	1.606	0.008
3150	1.606	0.007
3200	1.606	0.007
3250	1.606	0.007
3300	1.606	0.007
3350	1.606	0.006
3400	1.606	0.006
3460	1.606	0.006
3500	1.606	0.006
3550	1.606	0.005
3600	1.605	0.005
3650	1.605	0.005
3700	1.605	0.005
3750	1.605	0.004
3800	1.605	0.004
3850	1.605	0.003
3900	1.605	0.003
3950	1.605	0.003
4000	1.606	0.003
4050	1.605	0.002
4100	1.605	0.002
4150	1.605	0.002
4200	1.605	0 001
4250	1.606	0.001
4300	1.606	0.001
4350	1.605	0.001
4400	1.606	0.001
4450	1.605	0

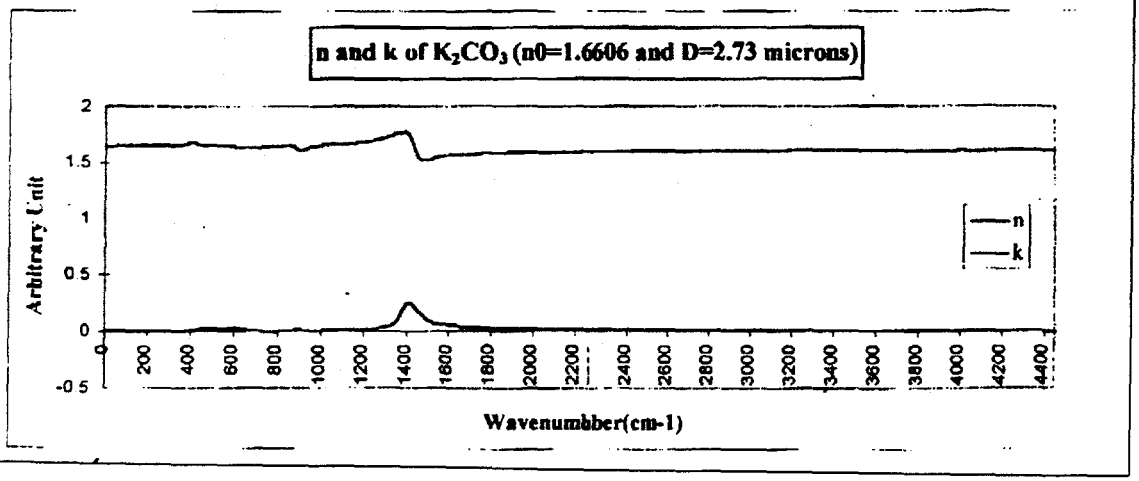

Figure E-4. The Optical constant results of K_2CO_3 at n_0 = 1.606 and diameter = 2.73 microns

Wavenumber(cm^{-1})	n	k
0	1.502	0
50	1.502	0
100	1.502	0
150	1.502	0
200	1.503	0
250	1.503	0
300	1.504	0
350	1.505	0
400	1.508	0
450	1.511	0
500	1.523	0.013
550	1.514	0.015
600	1.528	0.02
650	1.462	0.029
700	1.484	0.006
750	1.492	0.002
800	1.497	0.002
850	1.503	0.001
900	1.501	0.001
950	1.513	0.003
1000	1.521	0.009
1050	1.535	0.017
1100	1.569	0.068
1150	1.478	0.115
1200	1.424	0.037
1250	1.455	0.012
1300	1.469	0.007
1350	1.48	0.004
1400	1.503	0.014
1450	1.484	0.006
1500	1.448	0.019
1550	1.464	0.009
1600	1.47	0.01
1650	1.469	0.009
1700	1.471	0.008
1750	1.473	0.005
1800	1.474	0.004
1850	1.475	0.004
1900	1.476	0.004
1950	1.477	0.004
2000	1.478	0.003
2050	1.478	0.003
2100	1.478	0.003
2150	1.478	0.003
2200	1.479	0.003

Wavenumber(cm^{-1})	n	k
2250	1.479	0.003
2300	1.479	0.003
2350	1.479	0.002
2400	1.48	0.002
2450	1.48	0.003
2500	1.48	0.003
2550	1.48	0.003
2600	1.48	0.002
2650	1.48	0.002
2700	1.481	0.002
2750	1.481	0.002
2800	1.481	0.002
2850	1.481	0.002
2900	1.481	0.002
2950	1.481	0.002
3000	1.481	0.002
3050	1.481	0.002
3100	1.481	0.002
3150	1.481	0.002
3200	1.481	0.002
3250	1.481	0.002
3300	1.481	0.002
3350	1.481	0.002
3400	1.481	0.002
3450	1.481	0.002
3500	1.481	0.002
3550	1.481	0.002
3600	1.481	0.002
3650	1.481	0.002
3700	1.481	0.001
3750	1.481	0.001
3800	1.481	0.001
3850	1.481	0.001
3900	1.48	0.001
3950	1.481	0.001
4000	1.481	0.001
4050	1.481	0.001
4100	1.481	0.001
4150	1.481	0.001
4200	1.481	0
4250	1.481	0
4300	1.481	0.001
4350	1.481	0
4400	1.481	0
4450	1.481	0

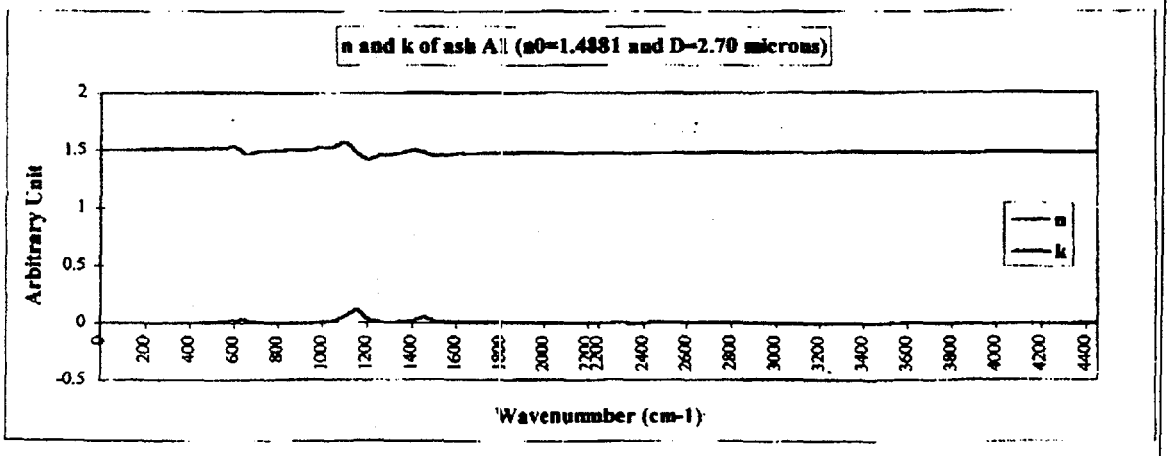

Figure E-5. The Optical constant results of ash A1 at n_0 = 1.481 and Diameter = 2.70 microns

Wavenumber(cm^{-1})	n	k
0	1.507	0
50	1.507	0
100	1.507	0
150	1.508	0
200	1.508	0
250	1.509	0
300	1.51	0
350	1.512	0
400	1.515	0
450	1.52	0
500	1.537	0.022
550	1.519	0.02
600	1.538	0.026
650	1.458	0.037
700	1.484	0.009
750	1.493	0.003
800	1.5	0.001
850	1.509	0.001
900	1.505	0.001
950	1.52	0.004
1000	1.53	0.011
1050	1.546	0.022
1100	1.581	0.084
1150	1.477	0.13
1200	1.418	0.045
1250	1.462	0.016
1300	1.467	0.009
1350	1.48	0.005
1400	1.508	0.017
1450	1.485	0.063
1500	1.445	0.024
1550	1.463	0.012
1600	1.47	0.013
1650	1.466	0.013
1700	1.468	0.008
1750	1.471	0.006
1800	1.473	0.005
1850	1.475	0.005
1900	1.476	0.004
1950	1.477	0.004
2000	1.477	0.004
2050	1.478	0.004
2100	1.478	0.004
2150	1.478	0.004
2200	1.479	0.003

Wavenumber(cm^{-1})	n	k
2250	1.479	0.003
2300	1.479	0.003
2350	1.48	0.002
2400	1.48	0.003
2450	1.481	0.003
2500	1.481	0.003
2550	1.481	0.003
2600	1.481	0.003
2650	1.481	0.003
2700	1.481	0.003
2750	1.481	0.002
2800	1.482	0.002
2850	1.482	0.002
2900	1.482	0.002
2950	1.482	0.002
3000	1.482	0.002
3050	1.482	0.002
3100	1.482	0.002
3150	1.482	0.002
3200	1.482	0.002
3250	1.482	0.002
3300	1.482	0.002
3350	1.482	0.002
3400	1.482	0.002
3450	1.482	0.002
3500	1.482	0.002
3550	1.482	0.002
3600	1.482	0.002
3650	1.482	0.002
3700	1.482	0.002
3750	1.482	0.001
3800	1.482	0.001
3850	1.482	0.001
3900	1.482	0.001
3950	1.481	0.001
4000	1.482	0.001
4050	1.482	0.001
4100	1.482	0.001
4150	1.482	0.001
4200	1.482	0
4250	1.482	0
4300	1.482	0.001
4350	1.482	0
4400	1.482	0
4450	1.482	0

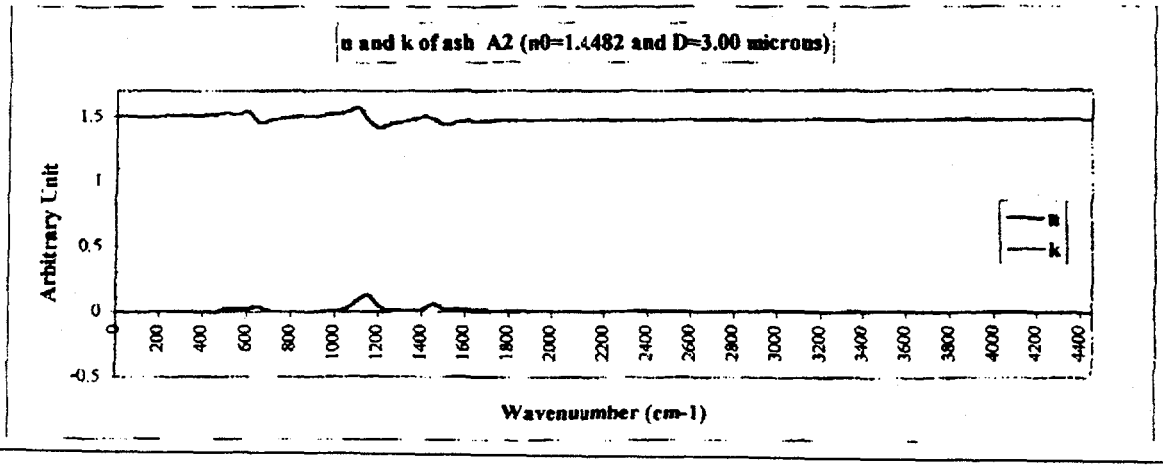

Figure E-6. The Optical constant results of ash A2 at n_0 = 1.482 and diameter = 3.00 microns

Wavenumber(cm^{-1})	n	k
0	1.498	0
50	1.498	0
100	1.498	0
150	1.499	0
200	1.499	0
250	1.499	0
300	1.5	0
350	1.5	0
400	1.501	0
450	1.503	0
500	1.509	0.004
550	1.51	0.009
600	1.512	0.017
650	1.474	0.016
700	1.486	0.002
750	1.483	0.001
800	1.496	0.003
850	1.496	0.003
900	1.496	0
950	1.502	0.001
1000	1.508	0.008
1050	1.512	0.009
1100	1.523	0.036
1150	1.484	0.048
1200	1.467	0.018
1250	1.476	0.007
1300	1.481	0.005
1350	1.484	0.004
1400	1.489	0.004
1450	1.49	0.015
1500	1.481	0.008
1550	1.484	0.004
1600	1.486	0.005
1650	1.484	0.005
1700	1.484	0.004
1750	1.485	0.003
1800	1.486	0.002
1850	1.486	0.002
1900	1.486	0.002
1950	1.487	0.002
2000	1.487	0.002
2050	1.487	0.002
2100	1.487	0.002
2150	1.487	0.002
2200	1.487	0.002

Wavenumber(cm^{-1})	n	k
2250	1.487	0.002
2300	1.487	0.002
2350	1.487	0.001
2400	1.488	0.001
2450	1.488	0.001
2500	1.488	0.001
2550	1.488	0.001
2600	1.488	0.001
2650	1.488	0.001
2700	1.488	0.001
2750	1.488	0.001
2800	1.488	0.001
2850	1.488	0.001
2900	1.488	0.001
2950	1.488	0.001
3000	1.488	0.001
3050	1.488	0.001
3100	1.488	0.001
3150	1.488	0.001
3200	1.488	0.001
3250	1.488	0.001
3300	1.488	0.001
3350	1.488	0.001
3400	1.488	0.001
3450	1.488	0.001
3500	1.488	0.001
3550	1.488	0.001
3600	1.488	0.001
3650	1.488	0.001
3700	1.488	0.001
3750	1.488	0.001
3800	1.488	0
3850	1.488	0
3900	1.488	0.001
3950	1.488	0
4000	1.488	0.001
4050	1.488	0
4100	1.488	0
4150	1.488	0
4200	1.488	0
4250	1.488	0
4300	1.488	0
4350	1.488	0
4400	1.488	0
4450	1.488	0

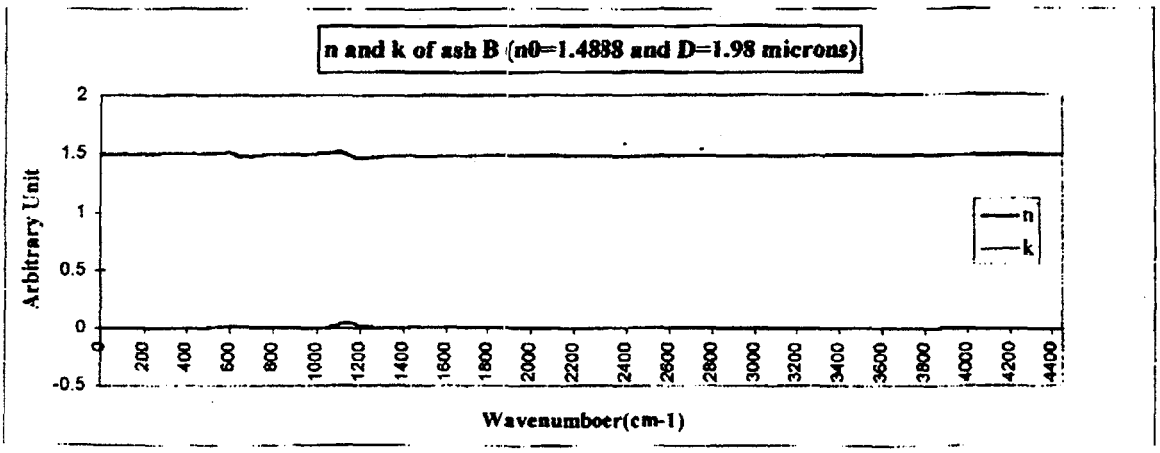

Figure E-7. The Optical constant results of ash B at n_0 = 1.488 and Diameter = 1.98 microns

Wavenumber(cm^{-1})	n	k
0	1.506	0
50	1.506	0
100	1.506	0
150	1.506	0
200	1.506	0
250	1.507	0
300	1.507	0
350	1.508	0
400	1.51	0
450	1.512	0
500	1.52	0.011
550	1.512	0.007
600	1.528	0.012
650	1.479	0.018
700	1.494	0.007
750	1.497	0.002
800	1.502	0
850	1.507	0.001
900	1.507	0.002
950	1.513	0.003
1000	1.519	0.006
1050	1.53	0.011
1100	1.554	0.056
1150	1.483	0.078
1200	1.452	0.027
1250	1.471	0.008
1300	1.48	0.005
1350	1.487	0.004
1400	1.495	0.005
1450	1.498	0.03
1500	1.475	0.007
1550	1.484	0.005
1600	1.487	0.006
1650	1.485	0.006
1700	1.486	0.004
1750	1.487	0.003
1800	1.488	0.002
1850	1.489	0.002
1900	1.489	0.002
1950	1.49	0.002
2000	1.49	0.002
2050	1.49	0.002
2100	1.49	0.002
2150	1.49	0.002
2200	1.491	0.002

Wavenumber(cm^{-1})	n	k
2250	1.491	0.002
2300	1.491	0.002
2350	1.491	0.002
2400	1.491	0.001
2450	1.491	0.001
2500	1.491	0.002
2550	1.491	0.001
2600	1.492	0.001
2650	1.492	0.001
2700	1.492	0.001
2750	1.492	0.001
2800	1.492	0.001
2850	1.492	0.001
2900	1.492	0.001
2950	1.492	0.001
3000	1.492	0.001
3050	1.492	0.001
3100	1.492	0.001
3150	1.492	0.001
3200	1.492	0.001
3250	1.492	0.001
3300	1.492	0.001
3350	1.492	0.001
3400	1.492	0.001
3450	1.492	0.001
3500	1.492	0.001
3550	1.492	0.001
3600	1.492	0.001
3650	1.492	0.001
3700	1.492	0.001
3750	1.492	0.001
3800	1.492	0.001
3850	1.492	0.001
3900	1.492	0.001
3950	1.492	0
4000	1.492	0.001
4050	1.492	0
4100	1.492	0
4150	1.492	0
4200	1.492	0
4250	1.492	0
4300	1.492	0
4350	1.492	0
4400	1.492	0
4450	1.492	0

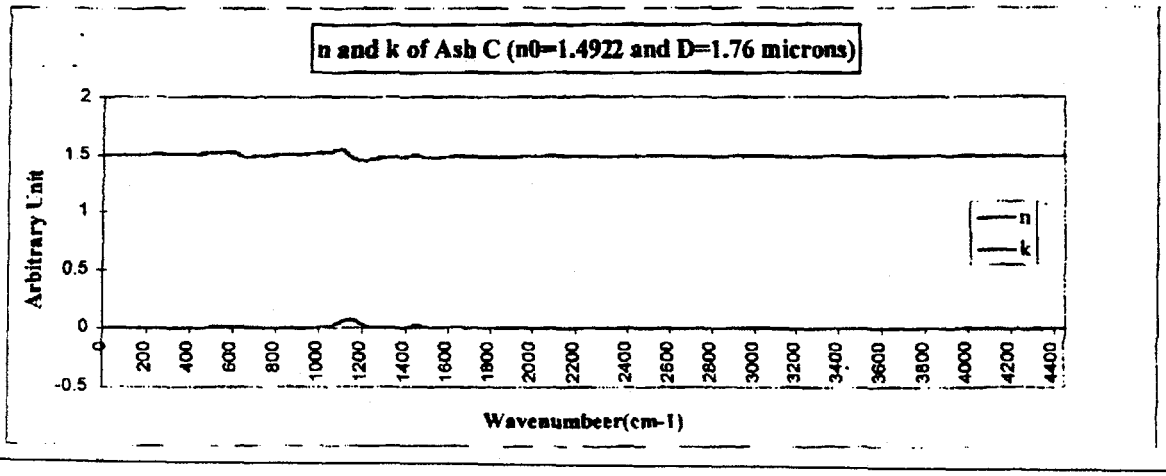

Figure E-8. The Optical constant results of ash C at n_0 = 1.492 and Diameter = 1.76 microns

Wavenumber(cm^{-1})	n	k
0	1.507	0
50	1.507	0
100	1.507	0
150	1.507	0
200	1.507	0
250	1.508	0
300	1.509	0
350	1.509	0
400	1.511	0
450	1.514	0
500	1.524	0.011
550	1.515	0.015
600	1.516	0.018
650	1.481	0.016
700	1.493	0.003
750	1.5	0.002
800	1.502	0.002
850	1.504	0.002
900	1.503	0
950	1.509	0.001
1000	1.514	0.005
1050	1.519	0.008
1100	1.533	0.011
1150	1.494	0.051
1200	1.472	0.017
1250	1.484	0.005
1300	1.49	0.003
1350	1.495	0.002
1400	1.505	0.007
1450	1.497	0.023
1500	1.483	0.006
1550	1.489	0.004
1600	1.492	0.005
1650	1.489	0.006
1700	1.49	0.003
1750	1.492	0.002
1800	1.492	0.002
1850	1.493	0.001
1900	1.494	0.001
1950	1.494	0.001
2000	1.494	0.001
2050	1.495	0.001
2100	1.495	0.001
2150	1.495	0.001
2200	1.495	0.001

Wavenumber(cm^{-1})	n	k
2250	1.495	0.001
2300	1.495	0.001
2350	1.495	0.001
2400	1.496	0.001
2450	1.496	0.001
2500	1.496	0.001
2550	1.496	0.001
2600	1.496	0.001
2650	1.496	0.001
2700	1.496	0.001
2750	1.496	0.001
2800	1.496	0.001
2850	1.496	0.001
2900	1.496	0.001
2950	1.496	0.001
3000	1.496	0.001
3050	1.496	0.001
3100	1.496	0.001
3150	1.496	0.001
3200	1.496	0.001
3250	1.496	0.001
3300	1.496	0.001
3350	1.496	0.001
3400	1.496	0.001
3450	1.496	0.001
3500	1.496	0.001
3550	1.496	0.001
3600	1.496	0.001
3650	1.496	0.001
3700	1.496	0.001
3750	1.496	0.001
3800	1.496	0.001
3850	1.496	0.001
3900	1.496	0.001
3950	1.496	0
4000	1.496	0
4050	1.496	0
4100	1.496	0
4150	1.496	0
4200	1.496	0
4250	1.496	0
4300	1.496	0
4350	1.496	0
4400	1.496	0
4450	1.496	0

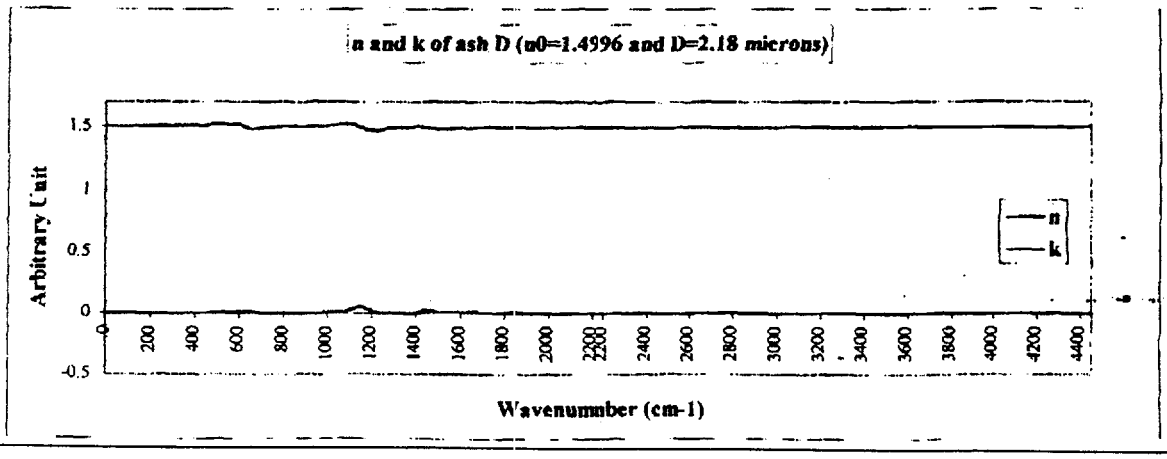

Figure E-9. The Optical constant results of ash D at n_0 = 1.496 and Diameter = 2.18 microns

Wavenumber(cm^{-1})	n	k
0	1.488	0
50	1.488	0
100	1.488	0
150	1.488	0
200	1.489	0
250	1.49	0
300	1.491	0
350	1.493	0
400	1.496	0
450	1.502	0
500	1.517	0.014
550	1.514	0.023
600	1.53	0.049
650	1.419	0.029
700	1.458	0.003
750	1.474	0.001
800	1.481	0.003
850	1.486	0.002
900	1.495	0.002
950	1.507	0.007
1000	1.513	0.024
1050	1.53	0.034
1100	1.552	0.117
1150	1.43	0.108
1200	1.402	0.059
1250	1.421	0.022
1300	1.434	0.016
1350	1.441	0.012
1400	1.445	0.011
1450	1.448	0.009
1500	1.451	0.008
1550	1.454	0.007
1600	1.457	0.01
1650	1.451	0.011
1700	1.452	0.006
1750	1.454	0.005
1800	1.455	0.004
1850	1.457	0.004
1900	1.457	0.004
1950	1.458	0.004
2000	1.459	0.004
2050	1.459	0.004
2100	1.459	0.004
2150	1.459	0.003
2200	1.459	0.003

Wavenumber(cm^{-1})	n	k
2250	1.46	0.003
2300	1.46	0.003
2350	1.46	0.002
2400	1.461	0.003
2450	1.461	0.003
2500	1.461	0.003
2550	1.461	0.002
2600	1.461	0.003
2650	1.461	0.002
2700	1.462	0.002
2750	1.462	0.002
2800	1.462	0.002
2850	1.462	0.002
2900	1.462	0.002
2950	1.462	0.002
3000	1.462	0.002
3050	1.462	0.002
3100	1.462	0.002
3150	1.462	0.002
3200	1.462	0.002
3250	1.462	0.002
3300	1.462	0.002
3350	1.462	0.002
3400	1.462	0.002
3450	1.462	0.002
3500	1.462	0.002
3550	1.462	0.002
3600	1.462	0.002
3650	1.462	0.002
3700	1.462	0.002
3750	1.462	0.001
3800	1.462	0.001
3850	1.462	0.001
3900	1.462	0.001
3950	1.462	0.001
4000	1.462	0.001
4050	1.462	0.001
4100	1.462	0.001
4150	1.462	0
4200	1.462	0
4250	1.462	0
4300	1.462	0
4350	1.462	0
4400	1.462	0
4450	1.462	0

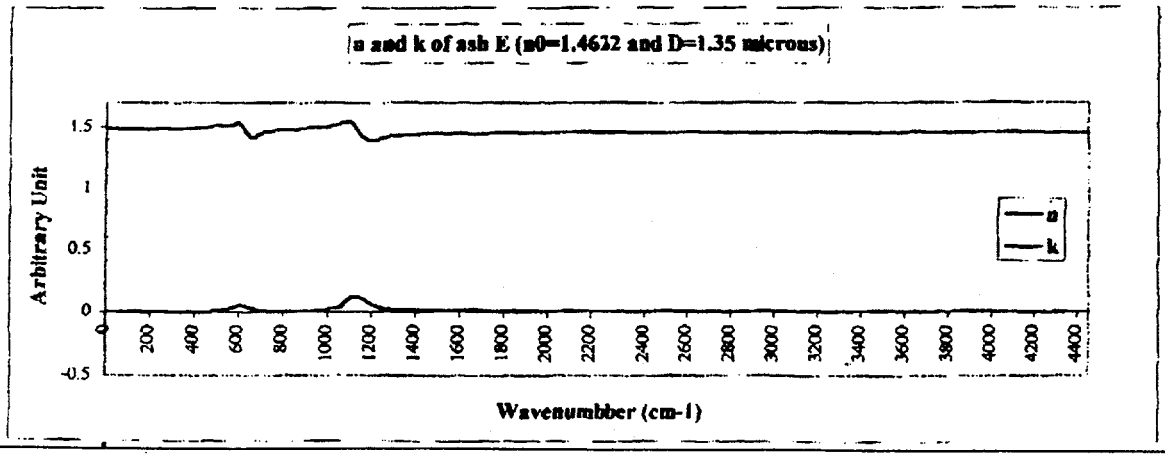

Figure E-10. The Optical constant results of ash E at n_0 = 1.462 and Diameter = 1.35 microns

Wavenumber(cm^{-1})	n	k
0	1.501	0
50	1.501	0
100	1.501	0
150	1.501	0
200	1.502	0
250	1.503	0
300	1.505	0
350	1.507	0
400	1.51	0
450	1.516	0
500	1.533	0.018
550	1.525	0.023
600	1.55	0.039
650	1.421	0.035
700	1.469	0.006
750	1.484	0.003
800	1.492	0.003
850	1.499	0.002
900	1 506	0
950	1.521	0.003
1000	1.534	0.017
1050	1.563	0.021
1100	1.632	0.156
1150	1.427	0.193
1200	1.361	0.086
1250	1.409	0.014
1300	1.433	0.009
1350	1.445	0.006
1400	1.455	0.007
1450	1.458	0.017
1500	1.453	0.006
1550	1.46	0.005
1600	1.464	0.008
1650	1.458	0.01
1700	1.48	0 004
1750	1.462	0.003
1800	1.464	0.002
1850	1.465	0.002
1900	1.466	0.002
1950	1.467	0.002
2000	1.468	0.002
2050	1.469	0.002
2100	1.469	0.003
2150	1.469	0.002
2200	1.469	0.002

Wavenumber(cm^{-1})	n	k
2250	1.47	0.002
2300	1.47	0.002
2350	1.47	0.001
2400	1.471	0.001
2450	1.471	0.001
2500	1.471	0.001
2550	1.471	0.001
2600	1.472	0.001
2650	1.472	0.001
2700	1.472	0.001
2750	1.472	0.001
2800	1.472	0.001
2850	1.473	0.001
2900	1.473	0.001
2950	1.473	0.001
3000	1.473	0.001
3050	1.473	0.001
3100	1.473	0.001
3150	1.473	0.001
3200	1.473	0.001
3250	1.473	0.001
3300	1.473	0.001
3350	1.473	0.001
3400	1.473	0.001
3450	1.473	0.001
3500	1.473	0.001
3550	1.473	0.001
3600	1.473	0.001
3650	1.473	0.001
3700	1.473	0.001
3750	1.473	0.001
3800	1.473	0.001
3850	1.473	0
3900	1.473	0.001
3950	1.473	0
4000	1.473	0.001
4050	1.473	0.001
4100	1.473	0.001
4150	1.473	0
4200	1.473	0
4250	1.473	0
4300	1.473	0
4350	1.473	0
4400	1.473	0
4450	1.472	0

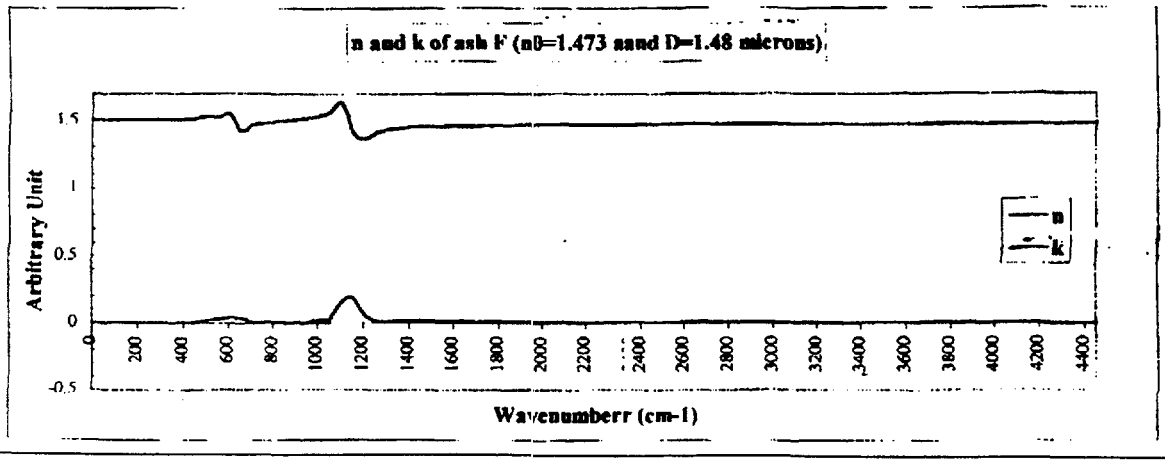

Figure E-11. The Optical constant results of ash F at n_0 = 1.473 and Diameter = 1.48 microns

ADDENDUM F:

Uncertainty Analysis

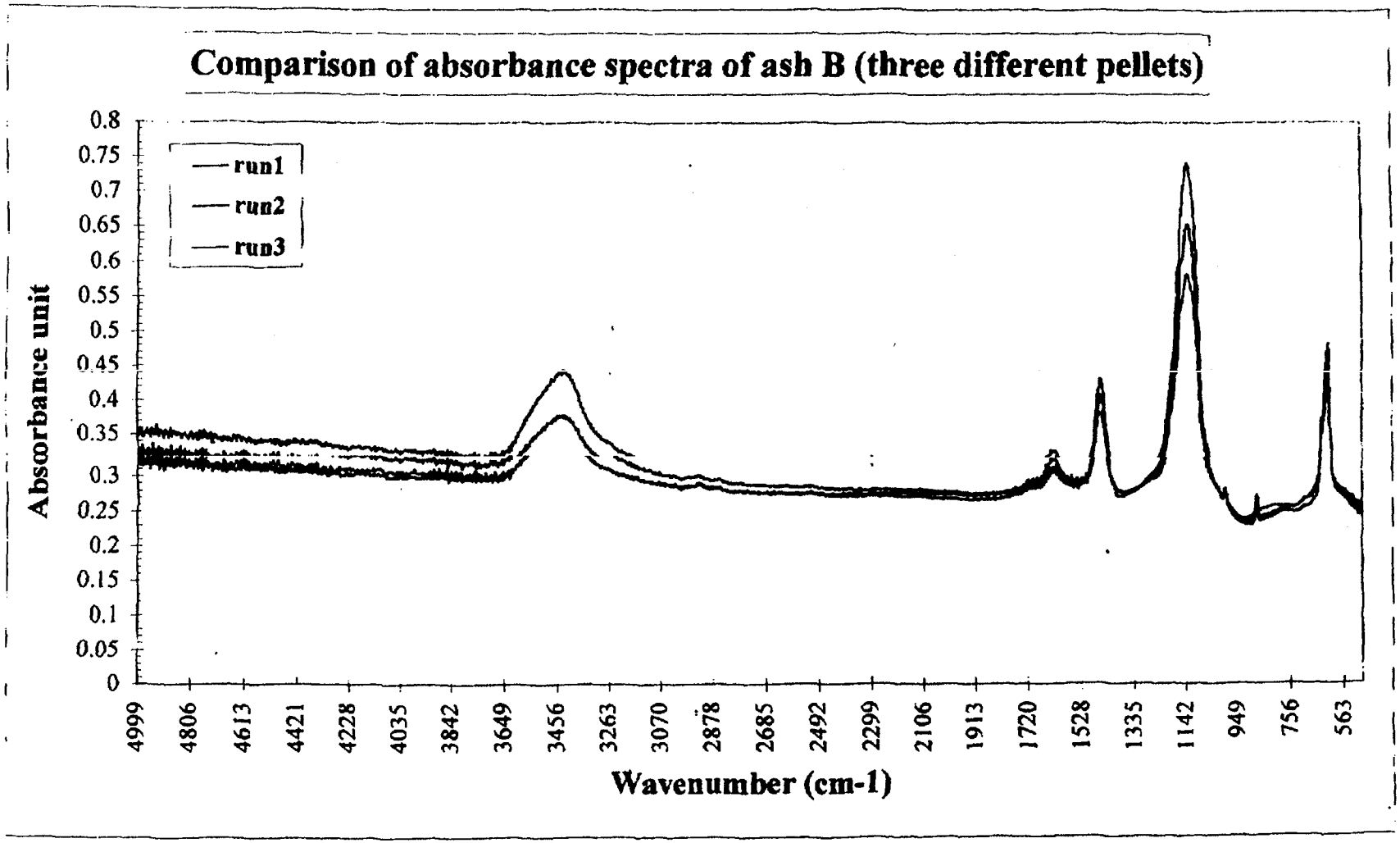

Figure F-1. The uncertainty of the absorbance spectra of ash B (considering three different pellets)

Ash B wavenumber (cm^{-1})	run1 n	run2 n	run3 n	run1 k	run2 k	run3 k
0	1.496	1.501	1.499	0	0	0
50	1.497	1.501	1.5	0	0	0
100	1.497	1.501	1.5	0	0	0
150	1.497	1.502	1.5	0	0	0
200	1.497	1.502	1.5	0	0	0
250	1.497	1.503	1.501	0	0	0
300	1.498	1.503	1.501	0	0	0
350	1.499	1.504	1.502	0	0	0
400	1.5	1.506	1.504	0	0	0
450	1.502	1.512	1.508	0	0.003	0.003
500	1.507	1.513	1.512	0.004	0.01	0.008
550	1.507	1.517	1.512	0.01	0.017	0.017
600	1.509	1.474	1.479	0.017	0.016	0.016
650	1.473	1.489	1.488	0.015	0.002	0.003
700	1.484	1.497	1.495	0.002	0.001	0.001
750	1.491	1.499	1.497	0.001	0.003	0.004
800	1.494	1.499	1.496	0.003	0.002	0.004
850	1.494	1.5	1.496	0.002	0	0.001
900	1.495	1.507	1.502	0	0.001	0.001
950	1.5	1.512	1.505	0.001	0.006	0.005
1000	1.504	1.519	1.51	0.005	0.01	0.008
1050	1.51	1.533	1.518	0.009	0.04	0.028
1100	1.522	1.485	1.487	0.033	0.058	0.039
1150	1.483	1.463	1.473	0.047	0.022	0.015
1200	1.465	1.475	1.481	0.018	0.008	0.007
1250	1.475	1.481	1.485	0.007	0.006	0.005
1300	1.48	1.484	1.487	0.005	0.004	0.004
1350	1.483	1.49	1.491	0.004	0.004	0.004
1400	1.487	1.491	1.491	0.004	0.018	0.013
1450	1.488	1.481	1.485	0.015	0.006	0.005
1500	1.48	1.485	1.487	0.006	0.004	0.004
1550	1.483	1.486	1.488	0.004	0.005	0.005
1600	1.485	1.485	1.487	0.005	0.005	0.005
1650	1.482	1.486	1.487	0.006	0.003	0.004
1700	1.483	1.487	1.487	0.004	0.003	0.003
1750	1.483	1.487	1.488	0.003	0.002	0.002
1800	1.484	1.488	1.488	0.002	0.002	0.002
1850	1.485	1.488	1.489	0.002	0.002	0.002
1900	1.485	1.488	1.489	0.002	0.002	0.002
1950	1.485	1.488	1.489	0.002	0.002	0.002
2000	1.485	1.489	1.489	0.002	0.002	0.002
2050	1.485	1.489	1.489	0.002	0.002	0.002
2100	1.486	1.489	1.489	0.002	0.002	0.002
2150	1.486	1.489	1.489	0.002	0.002	0.002
2200	1.486	1.489	1.489	0.002	0.002	0.002

Ash B wavenumber (cm^{-1})	run1 n	run2 n	run3 n	run1 k	run2 k	run3 k
2250	1.486	1.489	1.489	0.002	0.002	0.002
2300	1.486	1.489	1.489	0.002	0.002	0.001
2350	1.486	1.489	1.489	0.002	0.001	0.001
2400	1.486	1.489	1.49	0.002	0.001	0.001
2450	1.486	1.49	1.49	0.001	0.001	0.001
2500	1.486	1.489	1.49	0.002	0.001	0.001
2550	1.486	1.49	1.49	0.001	0.001	0.001
2600	1.486	1.49	1.49	0.001	0.001	0.001
2650	1.486	1.49	1.49	0.001	0.001	0.001
2700	1.486	1.49	1.49	0.001	0.001	0.001
2750	1.486	1.49	1.49	0.001	0.001	0.001
2800	1.486	1.49	1.49	0.001	0.001	0.001
2850	1.486	1.49	1.49	0.001	0.001	0.001
2900	1.486	1.49	1.49	0.001	0.001	0.001
2950	1.486	1.49	1.49	0.001	0.001	0.001
3000	1.486	1.49	1.49	0.001	0.001	0.001
3050	1.486	1.49	1.49	0.001	0.001	0.001
3100	1.486	1.49	1.49	0.001	0.001	0.001
3150	1.486	1.49	1.49	0.001	0.001	0.001
3200	1.486	1.49	1.49	0.001	0.001	0.001
3250	1.486	1.49	1.49	0.001	0.001	0.001
3300	1.486	1.49	1.49	0.001	0.001	0.001
3350	1.486	1.49	1.49	0.001	0.001	0.001
3400	1.486	1.49	1.49	0.001	0.001	0.001
3450	1.486	1.49	1.49	0.001	0.001	0.001
3500	1.486	1.49	1.49	0.001	0.001	0.001
3550	1.486	1.49	1.49	0.001	0.001	0.001
3600	1.486	1.49	1.49	0.001	0.001	0.001
3650	1.486	1.49	1.49	0.001	0.001	0.001
3700	1.486	1.49	1.49	0.001	0.001	0.001
3750	1.486	1.49	1.49	0.001	0	0
3800	1.486	1.49	1.49	0.001	0.001	0
3850	1.486	1.49	1.49	0.001	0.001	0.001
3900	1.486	1.49	1.49	0.001	0	0
3950	1.486	1.49	1.49	0	0	0
4000	1.486	1.49	1.49	0.001	0	0
4050	1.486	1.49	1.49	0.001	0	0
4100	1.486	1.49	1.49	0.001	0	0
4150	1.486	1.49	1.49	0.001	0	0
4200	1.486	1.49	1.49	0	0	0
4250	1.486	1.49	1.49	0	0	0
4300	1.486	1.49	1.49	0.001	0	0
4350	1.486	1.49	1.49	0	0	0
4400	1.486	1.49	1.49	0	0	0
4450	1.486	1.49	1.49	0	0	0

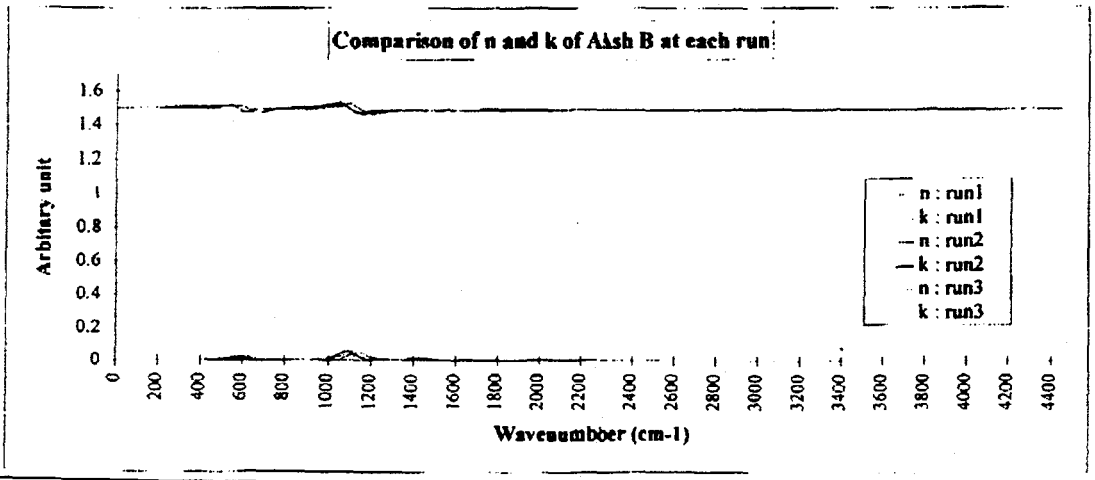

Table F-1. The comparison of the optical constants of ash B showing the uncertainty of n and k due to the absorbance spectra

Ash B	Particle diameter (microns)					
	1.5	2	2.5	1.5	2	2.5
wavenumber (cm-1)	n	n	n	k	k	k
0	1.49	1.498	1.501	0	0	0
50	1.49	1.498	1.501	0	0	0
100	1.49	1.498	1.502	0	0	0
150	1.49	1.498	1.502	0	0	0
200	1.49	1.498	1.502	0	0	0
250	1.491	1.499	1.502	0	0	0
300	1.491	1.499	1.503	0	0	0
350	1.492	1.5	1.503	0	0	0
400	1.493	1.501	1.504	0	0	0
450	1.495	1.503	1.506	0	0	0
500	1.499	1.507	1.511	0.003	0.003	0.003
550	1.501	1.509	1.513	0.009	0.009	0.009
600	1.503	1.511	1.515	0.017	0.017	0.017
650	1.466	1.474	1.477	0.015	0.015	0.015
700	1.478	1.486	1.49	0.002	0.002	0.002
750	1.485	1.493	1.497	0.001	0.001	0.001
800	1.488	1.496	1.499	0.003	0.003	0.003
850	1.487	1.495	1.499	0.003	0.003	0.003
900	1.488	1.496	1.5	0	0	0
950	1.494	1.502	1.506	0.001	0.001	0.001
1000	1.498	1.506	1.51	0.005	0.005	0.005
1050	1.504	1.512	1.515	0.009	0.009	0.009
1100	1.515	1.523	1.527	0.033	0.033	0.033
1150	1.476	1.484	1.487	0.047	0.048	0.048
1200	1.459	1.466	1.47	0.018	0.018	0.017
1250	1.468	1.476	1.48	0.007	0.007	0.007
1300	1.473	1.481	1.484	0.005	0.005	0.005
1350	1.476	1.484	1.488	0.004	0.004	0.004
1400	1.48	1.488	1.492	0.004	0.003	0.003
1450	1.482	1.489	1.493	0.015	0.015	0.015
1500	1.473	1.481	1.484	0.006	0.006	0.005
1550	1.476	1.484	1.488	0.004	0.004	0.004
1600	1.477	1.485	1.489	0.005	0.005	0.005
1650	1.476	1.484	1.487	0.005	0.005	0.005
1700	1.476	1.484	1.488	0.004	0.003	0.003
1750	1.477	1.485	1.488	0.003	0.003	0.002
1800	1.477	1.485	1.489	0.002	0.002	0.002
1850	1.478	1.486	1.49	0.002	0.002	0.002
1900	1.478	1.486	1.49	0.002	0.002	0.002
1950	1.478	1.486	1.49	0.002	0.002	0.002
2000	1.479	1.487	1.49	0.002	0.002	0.002
2050	1.479	1.487	1.49	0.002	0.002	0.002
2100	1.479	1.487	1.491	0.002	0.002	0.002
2150	1.479	1.487	1.491	0.002	0.002	0.002
2200	1.479	1.487	1.491	0.002	0.002	0.002

Ash B	Particle diameter (microns)					
	1.5	2	2.5	1.5	2	2.5
wavenumber (cm-1)	n	n	n	k	k	k
2250	1.479	1.487	1.491	0.002	0.002	0.001
2300	1.479	1.487	1.491	0.001	0.001	0.001
2350	1.479	1.487	1.491	0.001	0.001	0.001
2400	1.48	1.488	1.491	0.001	0.001	0.001
2450	1.48	1.488	1.491	0.001	0.001	0.001
2500	1.48	1.488	1.491	0.001	0.001	0.001
2550	1.48	1.488	1.491	0.001	0.001	0.001
2600	1.48	1.488	1.491	0.001	0.001	0.001
2650	1.48	1.488	1.491	0.001	0.001	0.001
2700	1.48	1.488	1.491	0.001	0.001	0.001
2750	1.48	1.488	1.492	0.001	0.001	0.001
2800	1.48	1.488	1.492	0.001	0.001	0.001
2850	1.48	1.488	1.492	0.001	0.001	0.001
2900	1.48	1.488	1.492	0.001	0.001	0.001
2950	1.48	1.488	1.492	0.001	0.001	0.001
3000	1.48	1.488	1.492	0.001	0.001	0.001
3050	1.48	1.488	1.492	0.001	0.001	0.001
3100	1.48	1.488	1.492	0.001	0.001	0.001
3150	1.48	1.488	1.492	0.001	0.001	0.001
3200	1.48	1.488	1.492	0.001	0.001	0.001
3250	1.48	1.488	1.492	0.001	0.001	0.001
3300	1.48	1.488	1.492	0.001	0.001	0.001
3350	1.48	1.488	1.492	0.001	0.001	0.001
3400	1.48	1.488	1.492	0.001	0.001	0.001
3450	1.48	1.488	1.492	0.001	0.001	0.001
3500	1.48	1.488	1.492	0.001	0.001	0.001
3550	1.48	1.488	1.492	0.001	0.001	0.001
3600	1.48	1.488	1.492	0.001	0.001	0
3650	1.48	1.488	1.492	0.001	0.001	0
3700	1.48	1.488	1.492	0.001	0.001	0
3750	1.48	1.488	1.492	0.001	0.001	0.001
3800	1.48	1.488	1.492	0	0	0
3850	1.48	1.488	1.492	0	0	0
3900	1.48	1.488	1.492	0.001	0.001	0
3950	1.48	1.488	1.492	0	0	0
4000	1.48	1.488	1.492	0	0	0
4050	1.48	1.488	1.492	0	0	0
4100	1.48	1.488	1.492	0	0	0
4150	1.48	1.488	1.492	0	0	0
4200	1.48	1.488	1.492	0	0	0
4250	1.48	1.488	1.492	0	0	0
4300	1.48	1.488	1.492	0	0	0
4350	1.48	1.488	1.492	0	0	0
4400	1.48	1.488	1.492	0	0	0
4450	1.48	1.488	1.492	0	0	0

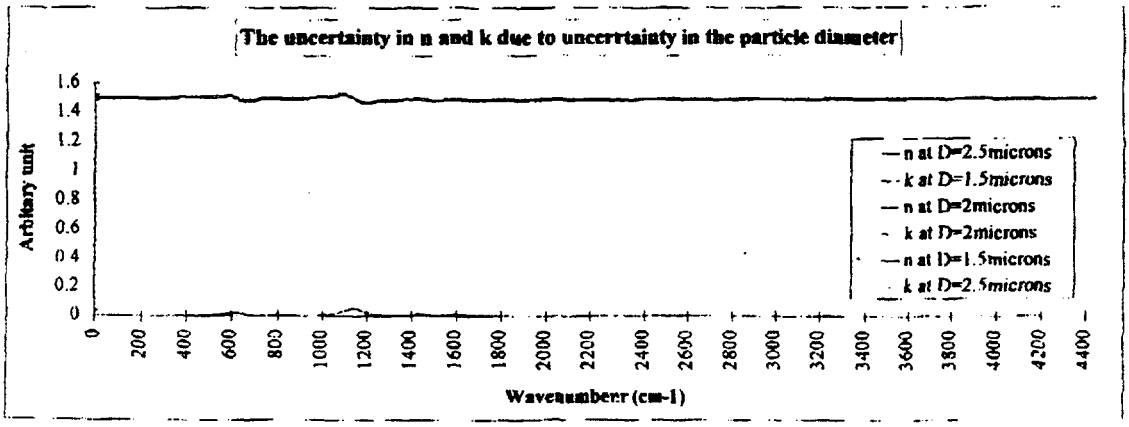

Table F-2. The uncertainty in n and k due to uncertainty in the particle diameter of ash B